A Sub-GHz UWB Pulse Generator for Wireless Biomedical Communication

Mark Stoopman

A Thesis Submitted to
The Faculty of Electrical Engineering, Mathematics and Computer Science in Partial Fulfillment of the Requirements for the Degree of
MASTER OF SCIENCE
in Electrical Engineering

Supervisor: Dr. ir. Wouter A. Serdijn

Thesis committee

Prof. dr. John R. Long
Dr. ir. Wouter A. Serdijn
Prof. dr. Alexander G. Yarovoy

Delft University of Technology

November 2010

A Sub-GHz UWB Pulse Generator for Wireless Biomedical Communication

Biomedical Electronics Group
Faculty of Electrical Engineering, Mathematics and Computer Science
Delft University of Technology

Abstract

The microelectronic revolution combined with the advances in neuroscience, surgical procedures and medicine will have a huge impact on the medical world in the near future. Implantable Medical Devices (IMD) equipped with wireless communication allow doctors to monitor, adjust and improve the treatment of medical disorders such as epilepsy, parkinson and Alzheimer's decease.

Today's wireless biomedical communication systems do not meet all requirements such as reliability, power consumption, bitrate and wireless range. This was the reason to investigate sub-GHz Ultra-Wideband (UWB) biomedical communication. This new concept can offer all the above mentioned requirements and also has negligible tissue heating due to the low average emission level.

As neither information is available on the human tissue penetration of sub-GHz UWB pulses, nor on the requirements and properties of the implantable antenna, the first part of this thesis focuses on the electrical characterization of human tissue and implantable antennas. A layered tissue model consisting of muscle, fat, skin and free space is used to study the power absorption over a broad frequency range. Furthermore, an antenna equivalent circuit model is developed based on various antenna simulations and measurements. Subsequently, the antenna-electronics interface was investigation and it was found that for this application a *current* driven antenna results in the most reliable signal transfer. This is a fundamentally different approach of terminating an antenna and is not bounded to the traditional 50 Ω interface.

A system level design is carried out in the second part of the thesis to obtain the design specifications for a sub-GHz UWB pulse generator. Variables such as bitrate, (indoor) UWB path loss, environment loss, battery capacity and receiver architecture are taken into account to obtain a realistic link budget.

In the last part of the thesis, a MOS-only ultra-low power pulse generator is designed using the AMIS 0.35μm I3T25 technology. The proposed pulse generator is capable of generating Binary Phase Shift Keying (BPSK) modulated pulses with a 550 MHz bandwidth and is tunable in pulse center frequency and output power. Circuit simulations showed a correct functioning pulse generator even under worst case condition and considerable antenna reactance variations. For a 2.5 V supply voltage and 1 Mb/s raw bitrate, the average power consumption ranges from 30 μW to 150 μW, depending on the pulse power controlled by the digital gain. This is considerably lower compared to commercially available implantable RF transmitters.

Preface

The report in front of you is the result of many hours spend on reading, writing and simulating during my master thesis project. My interest in UWB systems and biomedical engineering lead me to the Biomedical Electronics Group of Delft University of Technology. Together with Dr. ir. Wouter Serdijn I decided to investigate the feasibility of a new wireless biomedical communication concept, namely, sub-GHz UWB biomedical communication. A second challenge was to design a pulse generator for this application.

This project was not only limited to the design of electronic circuits, but also involved research in other fields such as biomedical and antenna engineering. Also, there were no specifications at the begin of this project, which I believe raises the creativity of the student. I find it very challenging and interesting to start a project from scratch and to gradually build up enough knowledge to arrive at a design that meets all specifications that are found along the way. I hope that my work will have a (small) contribution to the biomedical engineering field.

This work would not have been possible without the support and interest of others. First, I would like to thank my supervisor Wouter Serdijn. I greatly appreciate his way of coaching me during my thesis project. His sincere interest in my work encouraged and helped me to bring this work to its final form. He also gave me the opportunity to present my work at the BIOCAS conference in Cyprus, which I enjoyed very much. I feel honored by the trust that he puts in me.

Furthermore, I really appreciate the unique working environment in the ELCA group of Prof. John Long. Every since I was involved with the Delfi-C^3 nanosatellite project three years ago, I appreciated the relaxed atmosphere and professional working environment. I always enjoyed the daily technical and non-technical discussions during work, lunch and in the queue of the coffee machine. A big thanks goes to all the members of the Biomedical Electronics Group. Thank you for all the laughs, discussions, movie nights and the ELCA music festival. Marion, thank you for all the nice daily chats and candy.

Finally I want to thank my family, friends and girlfriend for supporting me throughout my thesis project.

Mark Stoopman
Delft, November 2010

Contents

List of Figures

List of Tables

List of Abbreviations

BER	Bit Error Rate
BPSK	Binary Phase Shift Keying
EIRP	Equivalent Isotropic Radiated Power
EM	ElectroMagnetic
ESA	Electrically Small Antenna
FCC	Federal Communications Commission
FS	Free Space
IC	Integrated Circuit
IR	Impulse Radio
MEMS	Micro ElectroMechanical Systems
MOS	Metal Oxide Semiconductor
IMD	Implantable Medical Devices
MOS	Metal Oxide Semiconductor
PCB	Printed Circuit Board
PRF	Pulse Repetition Frequency
PSD	Power Spectral Density
RF	Radio Frequency
SA	Specific Absorption
SAR	Specific Absorption Ratio
SNR	Signal to Noise Ratio
UWB	Ultra-WideBand

1. Introduction

Microelectronics has revolutionized the way people live. The small integrated circuits are hardly noticed by anyone, working silently at the background doing its task. It can offer intelligent, reliable and cheap solutions to various applications. Combining this with advances in neuroscience, surgical procedures and medicine will have a hugh impact on the medical world in the near future. Deep brain stimulation, personalized drug delivery, advanced medical procedures and patient monitoring are just a few applications in this multibillion-dollar market. A lot of research and development still has to be done and this thesis focuses on the research of wireless biomedical communication.

1.1. Wireless Biomedical Communication

The salamander is part of the amphibian family and can be found almost all around the globe. It is a remarkable creature because of its capability to regrow body parts, including legs, tail and even parts of their heart. Unfortunately, human beings *cannot* regrow a missing arm or leg. So, until we *can*, we have to take care of each other and as a consequence, the medical science field was born.

The field of biomedical engineering involves the applications of engineering principles and technology to the medical field to improve quality of life. It has emerged into a rapidly growing science since the implantation of the first cardiac pacemaker in 1958. Today's advanced electronics make it feasible to design small integrated systems which can be implanted inside the body.

The applications of biomedical engineering can be divided into diagnosis, monitoring and therapy. For all these applications there is a need for communication so that doctors can monitor, adjust and improve the treatment. Preferably, we would like to do this without any surgical procedure with risk of infection (percutaneous connection), but with a non-invasive solution (transcutaneous) such as wireless communication. This offers a very flexible and comfortable way of communication because the patient is unaware that his health is being monitored. Also, it can send an emergency alert to local hospitals if the implant malfunctions or detects a medical disorder such as a stroke. Furthermore, in the future, implants will be able to communicate with a WLAN in the patient's home environment so that the received data can automatically be forwarded to the doctor via the Internet. In addition, personalized settings can be uploaded to the implant to improve performance *after* the device is implanted. Thus, wireless biomedical communication is a promising application that really improves the patient's quality of life.

1.2. System Requirements

Safe

Since biomedical implants is applied in vivo, safety is of course a priority. The implant should be compatible with the human body and not contain any toxic material such as silver. Tissue heating caused by electromagnetic (EM) radiation is another concern that should be taken into account during design.

Small

Since area is extremely limited in implantable devices, the communication system should be small. This means that bulky components such as inductors should be avoided during the Integrated Circuit (IC) design. Another challenge is to use physical small antenna that still have good performance when inserted inside the body.

Ultra-low power

Currently, batteries provide all of the energy needs for implantable devices, but due to their fixed energy density, self-discharge, weight and volume constraints they have a limited operating lifetime. This is a major issue since batteries for implanted systems cannot be removed without surgery. So ultra-low power systems have to be designed to extend operating lifetime. In today's wireless systems, a large part of the complete transceiver power budget is used for the wireless communication. Improving this power hungry subsystem results in a significant improvement of the overall power consumption.

Today's pacemakers use lithium iodine batteries which have a battery capacity of approximately 2.5 Ah at 2.2 V [28]. If an implanted medical device were powered by a low-power general purpose processor such as the ATtiny 24, which draws aproximately 1.6 mA, current battery technology would accommodate 65 days of operation. Alternatively, dedicated solutions, employing sub-threshold circuit design, the current consumption can be reduced to approximately 3 μA as shown in [1], achieving almost 100 years of operating with the same battery. This however, is not feasable due to the self-discharge of the battery. This together with the actual pulse injection, the expected lifetime of a pacemaker battery is approximately 5-10 years.

An alternative solution is energy harvesting from an internal or external source. Examples of internal energy harvesting are converting thermal and mechanical energy into electrical energy which can be stored electrically or chemically. Micro ElectroMechanical Systems (MEMS) can provide us with those kind of techniques and removes the burden of having to replace the battery. A power dissipation level below 100 μW would enable selfpowered nodes using energy extracted from the environment [2]. However, today's harvesting systems do not generate enough energy to power an entire implant. Near field inductive coupling is an example of external energy harvesting. It involves transmitting electromagnetic energy into the body and collecting it via a coil or antenna. This concept will be dealt with in more detail in Section 1.3.

In conclusion, we note that electronics have to be designed for ultra-low power consumption to extend operation lifetime, irrelevant of the energy source.

Bitrate

The required bitrate of the wireless link depends on the application. Modern neural signal recording systems with 100 or more electrodes can easily produce raw data rates of 15 Mb/s [3]. Conventional micropower wireless telemetry circuits cannot transmit data at such high rates, so data reduction is usually performed on-chip. A high bitrate is desired to send the same amount of data in less time which saves energy. So a high bitrate increases the functionality of implantable integrated circuits to accommodate for future implants. On the other hand, other applications such as heart monitoring requires lower bitrates and therefore can significantly reduce power consumption. Thus, a communication system has to be used that can handle a wide range of bitrates.

Reliable communication link

Finally, the communication link should be very reliable. This is a real challenge since the environment of the patient can have a big influence on the communication link. Especially when the patient is in a crowded hospital with all kind of other electronic radiating equipment, not to mention the influence of the patient's own body.

1.3. Present Day Communication Systems

1.3.1. Inductive Coupling

Wireless biomedical communication is not a new concept since communication has already been achieved by an inductive link [4]. It consists of a coil on the implant and an second external coil connected to a power source placed close to the surface of the skin. The low frequency near field inductive coupling makes it possible to transfer data *and* to deliver energy to the implant. Thus, by using this technique, the implants can last for a lifetime. However, it has some major drawbacks. The range of wireless communication is limited to a few cm's and is sensitive to the position of the external coil. Also, because of the compromise between the compactness of the coil, coupling coefficient and operating frequency, the bitrate is usually very poor. However, new developments showed some improvement in this. A 100% data-rate-to-carrier frequency ratio is presented in [5].

But because the wireless range is very limited, making health monitoring an inconvenient and time consuming process. So it seems that inductive coupling is not the perfect candidate for wireless biomedical communication.

1.3.2. Narrowband Communication

Researchers have tried to use narrowband communication techniques as an alternative solution. This offers some advantages with respect to inductive coupling. Firstly, the use of far field wave propagation can extend the wireless link range to several meter.

Secondly, a higher carrier frequency results in an increase of bandwidth. This makes it possible to achieve bitrates in the order of 200 kbit/s to 4 Mbit/s, depending on the distance and carrier frequency [6].

Nevertheless, this solution also comes with some drawbacks. The transmitter requires an energy storage device such as a battery, meaning that at some point the battery has to be replaced. Power consumption can be minimized by designing ultra-low power circuits to increase operation time. However, the *concept* of narrowband communication is not power efficient since traditional narrowband communication make use of a continuous wave, resulting in continuous power consumption.

Another important drawback is the fact that narrowband communication can suffer from frequency selective fading. In a multipath channel, EM waves travel by various paths to the receiver, resulting in signal overlapping. It is possible that the signals partly cancel each other so that that no information can be retrieved. Furthermore, narrowband communication can suffer from an antenna null. An antenna null is an area of the antenna's radiation pattern where the antenna is unable to radiate or receive. This depends on antenna geometry, frequency, surrounding environment and direction. For example, when the patient is in a small and crowded room, a combination of changing environment, wrong direction, body and antenna influence can result in a null in the communication link. Because all information is centered at one frequency, no information can be received. Worst case scenario is that no communication is possible due to a null or frequency selective fading in a life threatening situation.

What is more, antenna impedance matching with conventional narrowband matching techniques can be difficult because of unpredictable variations in electrical properties of the body. Each patient is unique, which means that an implanted antenna with tuned matching network can shift in resonance frequency, resulting in a significant mismatch and thus poor efficiency.

Biomedical narrowband communication is still a research field and a lot of papers have been written on in-body antenna and matching designs [7, 8, 9]. The designs are simulated and tested using phantoms, tissue simulating liquid and raw pork meat. Although narrowband communication solves the distance and bitrate problems of inductive coupling, it still has some reliability and power consumption issues as mentioned above. So we therefore have to investigate another communication system.

1.4. Ultra-Wideband Communication

The interest in commercial applications for Ultra-Wideband (UWB) wireless communication has increased greatly in the last decade. UWB impulse radio uses carrierless, short duration pulses send in time domain where the transmitted pulse occupies a certain spectral bandwidth. This is a fundamentally different technique compared to narrowband communication. Although it is an old technique[1], it has some very interesting properties.

[1]UWB was already developed in the 60's for radar and military communication.

Inspecting Shannon's channel capacity formula quickly shows the advantage when using UWB:

$$C = BW \log_2 \left(\frac{S+N}{N} \right) \tag{1.1}$$

Channel capacity and hence data rate increases linearly with bandwidth, whereas signal-to-noise ratio only increases logarithmically. So UWB can offer high speed communication which is superior to narrowband communication. This translates into longer battery life and more functionallity of the implanted integrated circuit. Another advantage is that UWB has a high level of multipath immunity. The probability that two reflected signals overlap in time is extremely small because of the short duration of the pulses and fine time gating resolution. Antenna nulls also don't have a significant effect since the information is widely spread in frequency. Even *if* a null occurs at a particular frequency, the receiver is still able to receive information from the rest of the frequency band. Therefore UWB communication can provide a higher level of reliability than narrowband communication. The concept of UWB communication is also ultra-low power since the transmitter is not active for 100% of the time during communication. The transmitter should only consume power when a pule is generated, it can be completely switched off during the time laps between two pulses. This is depicted in Figure 1.1. This concept is much more energy efficient compared to narrowband communication,

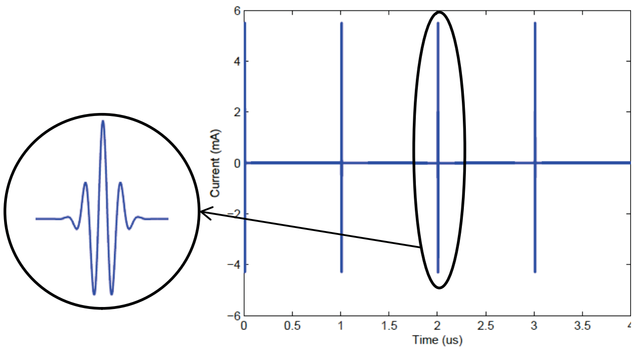

Figure 1.1.: An UWB transmitter should only consume power when a pulse is generated.

especially for low duty cycles. The communication range is limited to around 15 meters for typical UWB applications as the signal power is very low. But this is more than sufficient for biomedical communication.

Although this sounds very promising, it also comes with some design challenges. Covering an UWB spectrum puts high demands on the antenna and electronics design. The UWB antenna has to provide a suitable impedance across the entire band so that the electronics can drive it with a signal which results in the desired frequency band. Also, minimum ringing and constant group delay are desired aspects to design for.

UWB Regulations

Since UWB spans several commercially used frequency bands, there are strict regulations to be followed which prevent interference with other wireless systems such as Global Positioning System (GPS) and IEEE 802.11 WLAN. Unfortunately, world wide regulations for UWB communication is still not available today, so emission limits may vary with continent and country.

In 2002, the US Federal Communications Commission (FCC) issued the First Report and Order which permitted unlicensed UWB operation and commercial deployment of UWB devices. Here, UWB is defined as “an intentional radiator that, at any point in time, has a fractional bandwidth equal to or greater than 0.2 or a -10 dB UWB bandwidth equal or greater than 500 MHz, regardless of the fractional bandwidth.” The fractional bandwidth is calculated using

$$f_{frac,BW} = 2\frac{f_H - f_L}{f_H + f_L} \tag{1.2}$$

The UWB regulations are divided in many different categories for indoor and outdoor communication. The general FCC emission limits for indoor and outdoor UWB communication are depicted in Figure 1.2a.

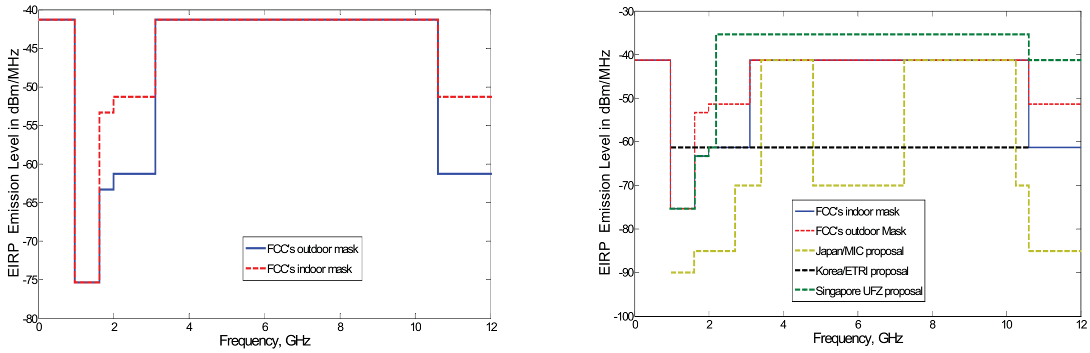

(a) FCC indoor and outdoor UWB emission masks.

(b) Proposed UWB emission masks in Asia.

Figure 1.2.: UWB emission masks.

The FCC made the 402-405 MHz band available for narrowband biomedical communication since this band satisfies the requirements with respect to EM wave penetration, antenna size, performance and receiver design. There is no special category for UWB biomedical communication yet, but it is likely that this category will fall under the general UWB communication emission limit described in part 15 of the FCC regulations which can be found in [10, 11].

A few years later, the European Telecommunications Standards institute (ETSI) and the Japan’s Ministry of Internal Affairs and Communications (MIC) also came up with its own regulations and they have some dissimilarities compared to the FCC regulations as can been seen in Figure 1.2b. Designing an UWB system which follows all international regulations is not doable. We decided to follow the FCC regulations since most recent designs use the FCC mask as emission limit. Also, the European and Asian regulatory authorities are still discussing these regulation issues. This in the contrast to the US, where the FCC has been active in the UWB area for a number of years.

1.5. Sub-GHz Frequency Band

The sub-GHz frequency band can offer several advantages compared to systems working in the GHz range. The propagation path loss is significantly smaller for low frequencies because of the squared relationship between the received power and frequency as shown in Equation 1.3.

$$P_{Rx} = P_{Tx} \left(\frac{c}{4\pi r f} \right)^2 G_{Tx} G_{Rx} \tag{1.3}$$

Furthermore, it provides good penetration which lead to useful applications such as ground penetrating radar, medical imaging system and through-wall imaging. It is also very interesting for biomedical UWB communication since we expect that in this frequency region the EM wave penetration is maximized while power consumption of the electronics can be kept low. Disadvantage is that the physical area of the antenna increases with decreasing frequency. Thus, a trade-off has to be mae between antenna size and operating frequency band.

1.6. Research Objectives

This work focuses on the uplink biomedical communication only, that is, the transmission of information from the implant to the external receiver. Main goal is to investigate the feasibility of a biomedical UWB communication system below 1 GHz. The advantages of sub-UWB discussed in Section 1.4 and 1.5 make this new research topic worthwhile exploring. To the authors knowledge, no such systems are found in the literature yet.

Since no specifications are given at the begin of this work, the challenges and requirements for sub-GHz UWB biomedical communication has to be identified and solved. The following research tasks have to be completed for a succesfull design:

- Characterize the communication channel.
- Determine the frequency band which is most suited for biomedical wireless communication.
- Investigate safety issues such as tissue heating.
- Investigate the influence and properties of implantable antennas.
- Find optimum antenna-electronics interface for reliable communication.

- System level design and link budget analysis.
- Design of a robust ultra-low power sub-GHz UWB pulse generator.

1.7. Thesis Outline

The thesis is organized as follows. The electrical characteristics of human tissue are investigated in Chapter two, where a simplied human body model will be developed to find the best operating frequency band for sub-GHz UWB communication. Also the Specific Absorption Ratio (SAR) is introduced which concerns the safety issues of electromagnetic power absorption by human tissue.

The implantable UWB antenna is treated in Chapter three. First, some important antenna parameters and requirements are introduced. Then, an antenna equivalent circuit model is developed based on antenna impedance measurements. Consequently, the antenna-electronics interface is investigated in great detail to obtain the most reliable signal transfer. Finally, antenna simulations are performed to obtain important antenna parameters and to verify an antenna-electronics interface experiment.

In the fourth chapter the system level design is discussed. To obtain the pulse generator circuit design specifications, the transmitter and receiver architecture are investigated. Variables such as bitrate, (indoor) UWB path loss and battery capacity are taken into account to obtain a realistic link budget. The required pulse properties are derived in the last part of this chapter.

A sub-GHz UWB pulse generator is designed in Chapter five. Various pulse generator topologies are discussed and process variations are taken into account during the topology choice and circuit design to obtain a robust pulse generator.

The designed pulse generator performance is verified with simulations in Chapter six. The robustness of the circuit is put to the test by varying process corners, device mismatch, load impedance, supply voltage and temperature.

Finally, the thesis ends with the scientic contribution, conclusions and recommendations.

2. Human tissue

A good channel definition is of great importance in any communication system. For biomedical communication, the channel exists of the implanted device, the human body, surrounding area of the patient and finally the receiver located somewhere in the room. Tissue properties may vary with patient dependent on weight, health, age, position and sex, making it difficult to predict the channel. Still, we need to have an estimation of how much power is lost in the channel. In this chapter the electrical characteristics of various tissues will be investigated and a simplified human body model will be developed. With this knowledge, an operating frequency band has to be chosen which complies with the FCC regulations. Finally, the Specific Absorption Ratio (SAR) is introduced which concerns the safety issues of electromagnetic power absorption by human tissue.

2.1. Electrical Characteristics of Human Tissue

To investigate the power loss versus frequency in a conductive environment, we need to define the dielectric properties of the tissue. As the human body is almost completely non-magnetic, we can set $\mu_r = 1$ so that $\mu = \mu_0 = 4\pi \cdot 10^{-7}$ [H/m] [17]. We will use this assumption throughout the whole thesis. We can express the dielectric properties by using the complex permittivity which describes the interaction of a material with an electric field. The complex *relative* permittivity is given by

$$\epsilon_r(j\omega) = \epsilon_r(\omega) + \frac{\sigma(\omega)}{j\omega\epsilon_0} \tag{2.1}$$

so that

$$\epsilon(j\omega) = \epsilon_0 \epsilon_r(j\omega) \tag{2.2}$$

where $\epsilon_0 = 8.854 \cdot 10^{-12}$ is the permittivity of free-space [F/m], $\sigma(\omega)$ is conductivity [S/m] and ω is the angular frequency [rad/s]. The *real* part is a measure of how much energy from an external electric field is stored in a material. The *imaginary* part describes how lossy a material is to an external electric field.

In 1996 Gabriel *et* al. measured and modeled various types of human tissue in the frequency range of 10 Hz to 20 GHz and can be found in [12, 13, 14]. Equation 2.3 gives a first order approximation of the complex relative permittivity.

$$\epsilon_r(j\omega) = \epsilon_\infty + \frac{\epsilon_s - \epsilon_\infty}{1 + j\omega\tau} \tag{2.3}$$

This is called the Debye expression in which ϵ_∞ is the permittivity at field frequencies where $\omega\tau \gg 1$ and ϵ_s the permittivity at $\omega\tau \ll 1$. As this expression only contains one pole, it is not accurate enough to analyze most human tissue over a broad frequency range. So Hurt [15] extended the model by a summation of Debye dispersions and added an extra term

$$\epsilon_r(j\omega) = \epsilon_\infty + \sum_{n=1}^{5} \frac{\epsilon_s - \epsilon_\infty}{1 + j\omega\tau_n} + \frac{\sigma_i}{j\omega\epsilon_0} \tag{2.4}$$

where σ_i is the static ionic conductivity. This multi-pole model is a much better approximation over an UWB frequency range. However, this model does not include the effect that each dispersion region may be broadened by multiple contributions. The broadening of the dispersion is accounted for by introducing distribution parameter α_n to each dispersion region:

$$\epsilon_r(j\omega) = \epsilon_\infty + \sum_{n=1}^{5} \frac{\epsilon_s - \epsilon_\infty}{1 + (j\omega\tau_n)^{(1-\alpha_n)}} + \frac{\sigma_i}{j\omega\epsilon_0} \tag{2.5}$$

When using the appropriate parameters given in [14] we can use equation 2.5 to analyze the power loss in various tissues.

For very accurate low frequency dry and wet skin models we can refer to a model developed by Raicu in 1999, which combines the Debye dispersion with the universal dielectric response behavior

$$\epsilon_r(j\omega) = \epsilon_\infty + \frac{\epsilon_s - \epsilon_\infty}{\left[\left(\frac{j\omega}{\omega_c}\right)^{\alpha} + \left(\frac{j\omega}{\omega_c}\right)^{(1-\beta)}\right]^{\gamma}} + \frac{\sigma_i}{j\omega\epsilon_0} \tag{2.6}$$

where α, β and γ are real constants and range from 0 to 1. The appropriate values for dry and wet skin can be found in [16].

2.2. Dielectric behavior of Human Tissue

The Cole-Cole model for dielectric properties of muscle, fat, dry and wet skin are plotted on a double logarithmic scale using matlab. What we can easily see in Figure 2.1a is that the relative permittivity can become as high as $\epsilon_r = 10^7\,\text{F/m}$ for low frequencies (<1 MHz), especially for muscle and fat. Also note the big difference in dry and wet skin at low frequencies, and that they eventually converge to the same value at higher frequencies.

The models for conductivity in Figure 2.1b are in line with our expectations. Tissues like muscle contain a lot of water so that their conductivity is much higher than tissues which contain less water such as fat. An important observation is that all tissues show a decreasing relative permittivity and an increasing conductivity with increasing frequency. This suggests that the power loss in all tissues will increase with frequency. Also, note that all tissues except fat converge to approximately the same ϵ_r and σ at high frequencies. At 1 GHz we find that for muscle and skin $40 \leq \epsilon_r \leq 55\,\text{F/m}$ and $\sigma \approx 0.93\,\text{S/m}$. The dielectric properties for fat at 1 GHz are $\epsilon_r = 13.08\,\text{F/m}$ and $\sigma = 0.095\,\text{S/m}$.

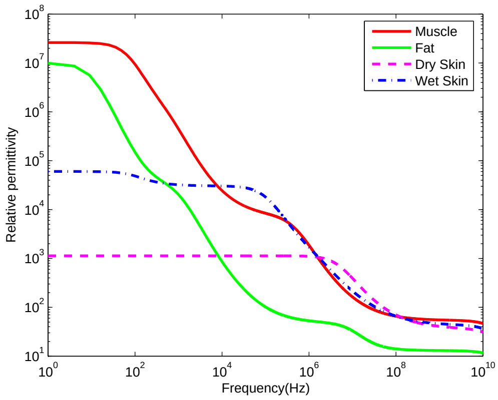

(a) Relative permittivity ϵ_r versus frequency.

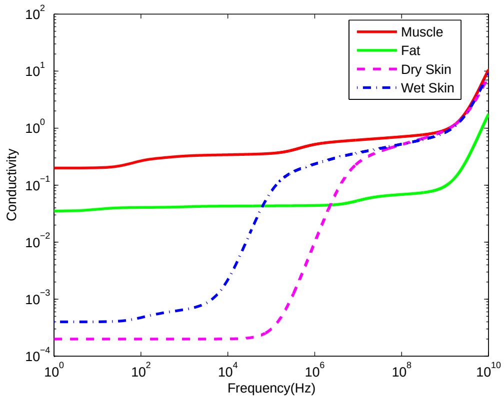

(b) Conductivity σ versus frequency.

Figure 2.1.: Dielectric properties as a function of frequency for various tissues using the Cole-Cole model.

2.2.1. Cole-Cole versus Raicu model

For dry and wet skin tissues we have two different models so we have to compare them and find the one which is most suited to this design. Figure 2.2 shows the two models in one graph for ϵ_r and σ.

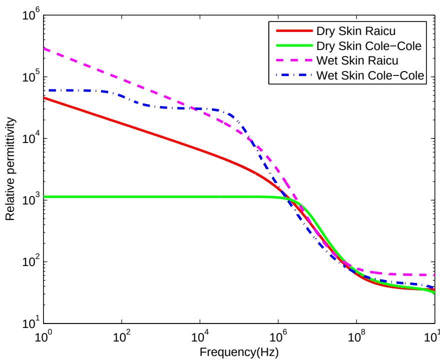

(a) Relative permittivity ϵ_r versus frequency

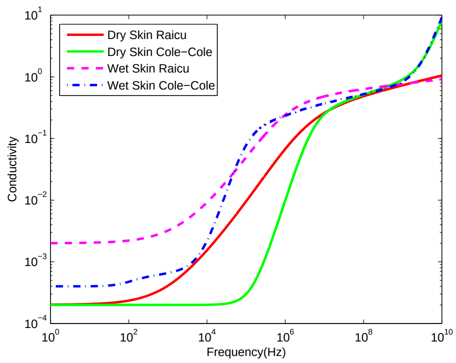

(b) Conductivity σ versus frequency

Figure 2.2.: Dry and wet skin Raicu vs. Cole-Cole

Note that the two models differ significantly at low and high frequencies. When comparing these models to the experimental data in [14], we conclude that the Raicu model is more accurate at low frequencies ($<$ 1MHz) and the Cole-Cole model is more reliable for frequencies above 1 MHz. Especially when looking at the difference in conductivity for frequencies higher than 600 MHz. So to analyze the power loss in human tissue we use the Cole-Cole model since we are not interested in frequencies below 1 MHz. Antennas at this frequency will be too large (physically) to be implanted. Antennas used in biomedical applications will be extensively discussed in chapter 3.

2.2.2. Further Characteristics of Tissue

Layer thickness can vary considerable when we compare patients on health, weight, age and sex. In this section some further tissue characteristics will be discussed. The following tissue thicknesses are reported in [18].

Muscle Muscle thickness can vary greatly depending on the location and patient. An adult can have a muscle thickness ranging from 0-30 mm, but also layer thicknesses of 60 mm and above are reported.

Fat The reported fat thickness for an adult lies between 0.4-23.2 mm, also dependent on location. For children this is considerable less, in the order of 0-16 mm. This limit does not take extremely obese people into account.

Skin The difference of skin for an adult and a child can also vary greatly. Adults have a skin thickness ranging from 0.8-2.6 mm whereas children skin thickness are around 0.4-1mm.

Homogeneity The properties of a homogeneous medium are characterized by the *spatially* independent constants σ,ϵ and μ. This does not hold for the human body. Nevertheless, homogeneity is usually assumed in tissue models to keep the analysis simple.

Isotropy of the Tissue Some tissues like muscle have anisotropic properties which changes the characteristics depending on direction. However, for most tissues it is a valid assumption to think of human tissue as isotropic [17].

Mass density The mass density for each tissue is important when calculating the power absorbed in a given volume, which will be explained in more detail in Section 2.5 where the Specific Absorption Rate (SAR) is defined. The mass density of muscle, fat and skin is 1040, 920 and 1010 $\left[\mathrm{kg/m^3}\right]$, respectively.

2.3. Human Tissue Modeling

Now that the dielectric properties of the tissues are known, a simplified multi-layered tissue model will be presented in this section to analyze the power loss.

2.3.1. Multi-Layered Tissue Model

The location of the implant will have a direct effect on the link budget. For this analysis, we assume that the implant is located closely underneath the skin. A one-dimensional layered tissue model is used to study the power loss. In this model the wave enters perpendicular to an isotropic, homogeneous, linear and time-invariant medium and propagates from inside the muscle tissue, making a transition to fat, skin and finally free space. The other two dimensions extend to infinity. To analyze implants which are located deeper inside the body, the model can be expanded by introducing one or more layers such as bone and brain tissue, depending on the location of the implant.

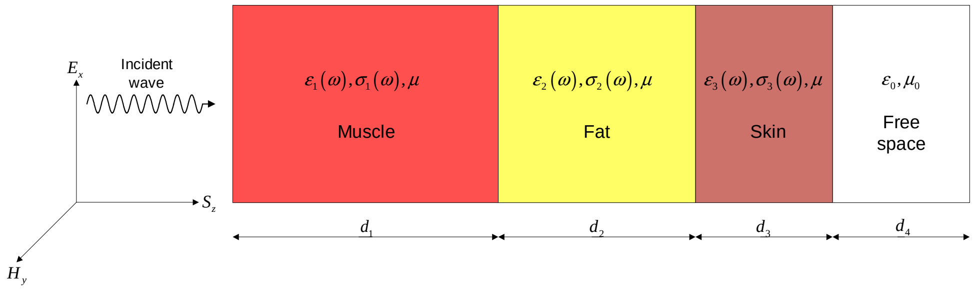

Figure 2.3.: One-dimensional layered tissue model

In the general case, EM wave propagation involves electric and magnetic fields having more than one component, each dependent on all three coordinates, in addition to time. Instead, a lot of EM fields are studied using a waveform which consists of electric and magnetic fields that are perpendicular to each other and to the direction of propagation. These waves are known as *plane waves*. Although plane waves do not exist in practice, they can be approximated by waves which propagate from a source located at a large distance (far field) [19].

Note that this is an extremely simplified model with a lot of assumptions made. Of course, in reality, the waves are generated by finite-sized antennas and therefore are non-planar. Moreover, the antenna is located *inside* the body, suggesting that the antenna radiation properties will be affected by the lossy near field. One might doubt the accuracy of this model, but some assumptions have to be made to simplify the analysis. The goal of this model is to have a rough estimation of the power loss over a broad frequency range to determine the best operating frequency band. Moreover, it makes little sense to use extremely accurate calculations for a model where the medium is as unpredictable as the human body.

Moreover, numerical models, no matter how complex, will serve only as best estimates.

2.3.2. Power transfer factor

In this analysis we define an uniform plane wave which only has an x-component (electric field) and y-component (magnetic field) which are both function of the propagation direction z only.

$$\mathbf{E} = \hat{E}_x e^{-\gamma z} \mathbf{a}_x \tag{2.7}$$

$$\mathbf{H} = \hat{H}_y e^{-\gamma z} \mathbf{a}_y \tag{2.8}$$

The propagation constant γ $\left[\mathrm{m}^{-1}\right]$ is dependent on the medium and is given by $\gamma = \sqrt{j\omega\mu_0\mu_r\left(\sigma + j\omega\epsilon_0\epsilon_r\right)}$. The derivation of γ can be found in Appendix A. The solution of this complex square root can be written as $\gamma = \alpha + j\beta$, where

$$\alpha = \frac{\omega}{c}\sqrt{\frac{\epsilon_r\mu_r}{2}\left[\sqrt{1+\left(\frac{\sigma}{\omega\epsilon_r\epsilon_0}\right)^2} - 1\right]} \tag{2.9}$$

$$\beta = \frac{\omega}{c}\sqrt{\frac{\epsilon_r\mu_r}{2}\left[\sqrt{1+\left(\frac{\sigma}{\omega\epsilon_r\epsilon_0}\right)^2} + 1\right]} \tag{2.10}$$

Here is α [Np/m] the attenuation constant and β [rad/m] the phase constant. In free space these equations reduce to $\alpha = 0$ and $\beta = \frac{\omega}{c}$, where $c = \frac{1}{\sqrt{\mu_0\epsilon_0}}$ is the speed of light in vacuum.

A convenient way to analyze the propagation of an EM wave in two different mediums is to use transmission line theory. The impedance of the medium can be represented by the wave impedance η, defined by the ratio between the electric and magnetic field. The *intrinsic* complex wave impedance can be written as

$$\eta = \frac{\eta_0}{\sqrt{\epsilon_r + \frac{\sigma}{j\omega\epsilon_0}}} \tag{2.11}$$

where $\eta_0 = \sqrt{\frac{\mu_0}{\epsilon_0}} \approx 120\pi$ $[\Omega]$ is the wave impedance in free space. Here it is assumed that $\mu_r = 1$.

The transmission coefficient of the wave propagating from medium 1 to medium 2 is defined as the ratio of the transmitted field to the incidental field. In terms of electric field, this becomes

$$T_E = \frac{\hat{E_x}^t}{\hat{E_x}^i} = \frac{2\eta_2}{\eta_1 + \eta_2} \tag{2.12}$$

Since the electric and the magnetic field components are related by η, we can write:

$$T_H = \frac{\eta_1}{\eta_2} T_E = \frac{2\eta_1}{\eta_1 + \eta_2} \tag{2.13}$$

By calculating the time-averaged power density S $\left[\mathrm{W/m^2}\right]$ of the wave in medium 1 and 2, we can determine the power loss in the medium. The real time-averaged power density in medium 2 is

$$S_2 = \frac{1}{2}\mathrm{Re}\left[\hat{\mathbf{E}}_2 \times \hat{\mathbf{H}}_2^*\right] =$$

$$\frac{1}{2}\mathrm{Re}\left[\left(T_E \hat{E_x}^i e^{-\gamma_2 z}\right) \times \left(T_M \hat{H_y}^i e^{-\gamma_2 z}\right)^*\right] \tag{2.14}$$

which reduces to

$$S_2 = S_1 \mathrm{Re}\left[\hat{T}_E \hat{T}_M^*\right] e^{-2\alpha_2 z} \tag{2.15}$$

The power transfer factor A_T is found when substituting equation 2.12 and 2.13 in 2.15:

$$A_T = \frac{S_2}{S_1} = 4\frac{\mathrm{Re}\left[\eta_1 \eta_2^*\right]}{|\eta_1 + \eta_2|^2} e^{-2\alpha_2 z} \tag{2.16}$$

Equation 2.16 can be separated into two parts, the first one being the impedance mismatch factor (the η ratio) due to the mismatch of the two mediums. The second part is the tissue propagation factor $e^{-2\alpha_2 z}$ which represents the power loss due to the propagation of the EM wave in a lossy medium. Both parts can be seen in Figure 2.4. We

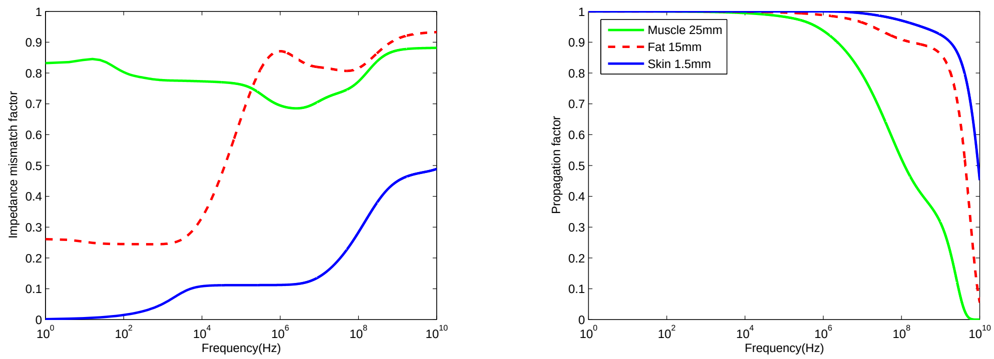

(a) Impedance mismatch transfer factor, Muscle-Fat (green), Fat-Skin (dashed red), Skin-FS (blue)

(b) Tissue propagation factor for muscle (25mm), fat (15mm), skin (1.5mm)

Figure 2.4.: Power transfer factor separated in impedance mismatch and propagation loss

can see that the transistion from skin-FS dominates across the entire frequency range. This can easily be explained by the fact that the difference in permittivity is the greatest between skin and free space than any other medium transition in this model, causing a large impedance mismatch. Furthermore we note that muscle propagation dominates the tissue propagation loss, especially at higher frequencies. This is because muscle is the thickest tissue layer and because of the increasing conductivity at high frequencies.

For a more general n-layered tissue model A_T can be written as :

$$A_T = \prod_{i=1}^{n} 4 \frac{\mathrm{Re}\left[\eta_{i-1}\eta_i^*\right]}{\left|\eta_i + \eta_{i-1}\right|^2} e^{-2\alpha_i d_i} \tag{2.17}$$

This can also be written in terms of attenuation and phase constants [20]:

$$A_T = \prod_{i=1}^{n} 4 \frac{\alpha_i \alpha_{i-1} + \beta_i \beta_{i-1}}{\left(\alpha_i + \alpha_{i-1}\right)^2 + \left(\beta_i + \beta_{i-1}\right)^2} e^{-2\alpha_i d_i} \tag{2.18}$$

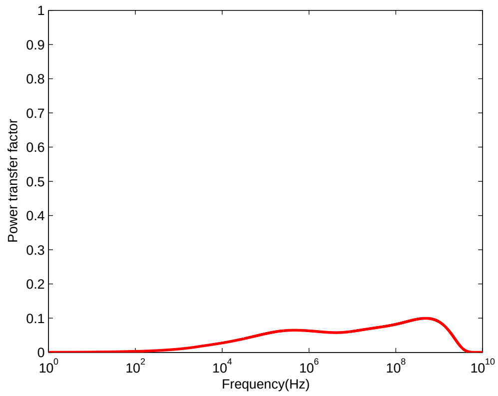

Figure 2.5.: Power transfer factor for a layered tissue model consisting of muscle (25mm), fat (15mm) and skin (1.5mm)

Looking at the total power transfer in Figure 2.5 we conclude that there is a constant optimum power transfer factor of approximately 0.1 at 350-600 MHz. This is in good agreement with the 402-405 MHz band made available by the FCC for biomedical communication. As expected, the power loss increases at high frequencies. This graph can be thought of as an upper limit for the power transfer because of all the assumptions made in this analysis. Be aware that this graph is dependent on the tissue thickness. To demonstrate this, we zoomed in on the power transfer while varying the muscle thickness as can be seen in Figure 2.6.

It is shown on a semi-logarithmic and linear scale for a clearer high and low frequency view. The results are intuitively satisfying and we can see that all power transfer functions converge to the same value at frequencies below 1 MHz. Furthermore it is evident that an increase of tissue layer thickness, or adding another layer, will decrease and *shift* the optimum power transfer to lower frequencies. In practice this graph will decrease and shift to even lower values due to all the assumptions made before. So we can conclude that the tissue penetration will be best for frequencies below approximately 1.5 GHz.

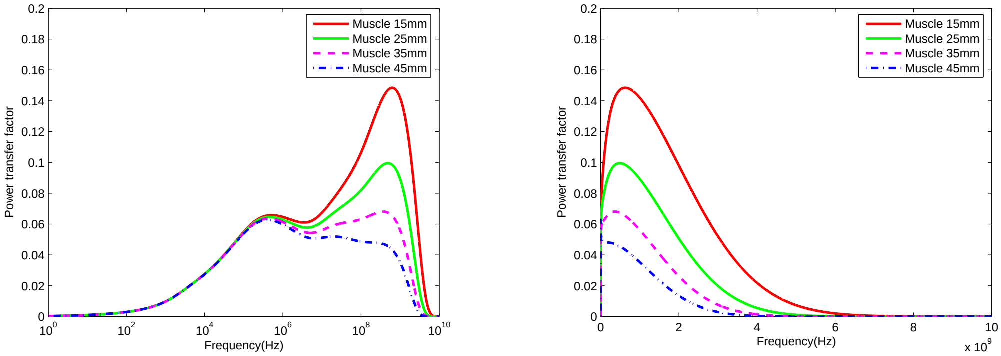

(a) Semi-logarithmic scale (b) Linear scale

Figure 2.6.: Power transfer factor for a muscle-fat-skin-FS layered tissue model with varying muscle thickness of 15mm, 25mm, 35mm and 45mm

2.4. Frequency band selection

At this point the power loss inside the tissue is known and a decision has to be made which frequency band is going to be used for this design. The power loss in a practical system increases rapidly at frequencies above 1.5 GHz, effectively decreasing the SNR ratio. Moreover, designing electronic circuits at these high frequencies (for example in the widely used 3.1-10.6 GHz range) requires a significantly higher bias current for the transistors just to operate compared to sub-GHz electronics. This in combination with the high dielectric losses makes a wireless biomedical communication system inefficient at high frequencies. Reviewing the FCC mask and the corresponding emission limits in Table 2.1 we note that the 960-1610 MHz band is heavily shielded. The Global Positioning System (GPS) operates in this band and because of its relative low power levels, the FCC is concerned with interference from other communication systems. So the FCC has set the average emission limit to -75.3 dBm/MHz.

Table 2.1.: FCC average emission limit applicable for indoor UWB operation [10]

Frequency (MHz)	Indoor emission limit (dBm/MHz)
0.009-960	-41.3
960-1610	-75.3
1610-1990	-53.3
1990-3100	-51.3
3100-10600	-41.3
Above 10600	-51.3

This is unfortunately also in the frequency range of interest in this design. The goal of this work is that this design eventually leads to an actual product, so it *has* to comply with the FCC mask. This means that we will set the upper frequency boundary to 960

MHz with an emission limit of -41.3 dBm/Mhz. Note that this is 34 dB higher than the allowed emission in the GPS band, which means that the higher band edge has to be steep enough to keep the emission within the limits of the FCC. The lowest frequency is of no importance yet since the antenna will limit the lower bound of the bandwidth. This will be discussed in chapter 3.

2.5. Specific Absorption Rate

In the last decade there are numerous of discussions on health issues. A recognizable example is the public concern that the use of mobile phones could increase the risk of brain tumors. The purpose of this section is to introduce the concept of Specific Absorption Ratio (SAR), which is the most common way to describe electromagnetic power absorption by human tissue and is defined as

$$SAR = \frac{d}{dt}\left(\frac{dW}{dm}\right) = \frac{d}{dt}\left(\frac{dW}{\rho dv}\right) = \frac{\sigma E^2}{\rho}\,[\mathrm{W/kg}] \tag{2.19}$$

where σ is the electrical conductivity [S/m], E is the rms electric field strength [V/m] and ρ is the mass density in $\left[\mathrm{kg/m^3}\right]$. The measured data must be averaged over a defined mass of tissue and a period of time. This is typically done for 6 minutes over a 1 or 10g cubic mass.

The real concern is the actual tissue heating due to the absorbed RF energy, since this can cause some adverse biological effects. Temperature increases in living tissue due to RF energy absorption which follow a well defined pattern with a (thermal) time constant of approximately 6 minutes.[1] These thermal effects are associated with whole-body heating at levels that usually increase temperature by approximately $1°C$ or more [21]. Short localized exposure of a few seconds can cause electric shocks and pain sensations. Extreme long and high power exposures in the order of hours can result in skin burn, heat stroke and damage to the central nervous system.

In some cases, for example in the medical field, it can be more convenient to express SAR in terms of tissue temperature changes

$$SAR = c\frac{\Delta T}{\Delta t} \tag{2.20}$$

where ΔT is the change of temperature [°C], Δt is the duration of exposure $[s]$ and c is the tissue specific heat capacity [J/kg°C]. Muscle has a specific heat capacity of $c = 3600\,\mathrm{J/kg°C}$. So an EM wave exposure of 6 minutes which increases the tissue temperature with 1 °C relates to a SAR of 10 W/kg. The SAR limits in Europe and the USA are given in Table 2.2. Whole body heating only happens in rare conditions and since the implant is located at a certain position in the body, it is more relevant to study the localized power absorption.

[1] 67% of the steady state temperature increase occurs within 6 minutes [22, 21].

Table 2.2.: Continuous wave exposure SAR limits for the general public.

	SAR Europe (W/kg)	SAR USA (W/kg)
Whole-body average	0.08	0.08
Localized 10g (peak spatial-average)	2	1.6
Extremities (arms and legs)	4	4

Pulsed EM wave exposure

Note that the limits in Table 2.2 are only applicable for continuous wave exposure. Since UWB transmitters emit very short but high peak RF pulses, this raises questions about the biological effects. For short duration pulses (< 30 µs), biological effects are dependent on the energy per pulse and correspond to a specific absorption per pulse (SA). Spatial peak SA is determined by evaluating the total energy delivered to any 10 g of contiguous tissue in the shape of a cube tissue within any 50 microsecond period. For the general public the spatial peak SA in the head in the frequency range of 0.3-6 GHz is limited to 2 mJ/kg [22].

Instantaneous spatial peak SAR in the head and torso for frequencies exceeding 10 MHz is determined by evaluating the total energy delivered to any 10 g of contiguous tissue in the shape of a cube tissue within any 1 µs period and is limited to 2000 W/kg. In conclusion, UWB impulse radio is less likely to cause adverse biological effects compared to narrow band biomedical communication.

2.6. Summary

In this chapter the power loss in a layered tissue model consisting of muscle, fat, skin and free space was studied over a frequency range from 10 Hz to 20 GHz. The tissues are characterized using the Cole-Cole approximation for the complex relative permittivity. A power transfer factor was derived for a uniform plane wave entering the layered tissue model. It was found that the power loss was minimized at frequencies below approximately 1.5 GHz. Increasing layer thickness or adding another layer will decrease and shift the frequency response to lower frequencies. Furthermore, it was decided that, when taking the FCC regulations into account, the upper band frequency has to be 960 MHz with an emission limit of -41.3 dBm/Mhz. The lower band frequency will be limited by the antenna design. Care must be taken not to exceed the -75.3 dBm/MHz limits of the GPS band which is located at 960-1610 MHz. Finally the Specific Absorption Rate was introduced. UWB impulse radio is less likely to cause adverse biological effects compared to narrow band biomedical communication because of the short pulse duration and low average emission level. A localized peak SAR for pulse modulated exposure of 2000 W/kg, or peak SA of 2 mJ/kg will be used as a limit to prevent tissue damage.

3. Implantable antennas

Antenna design is a scientific discipline which closes the gap between electronics and electromagnetic radiated fields. When opening an antenna theory textbook such as Antenna Theory by C.A. Balanis [23], one sees that the analysis of even the most simple antenna like the infinite small dipole can become very complex. Almost all textbooks describe antennas which are placed in vacuum where ϵ_r and μ_r are 1 and σ equals zero. When placing the same antenna *inside* the body, which has a high permittivity and conductivity, it will have a major impact on the antenna characteristics. The antenna, which is of high importance in the communication channel, determines the signal quantity of the electronic output stage, operating frequency band, power level and it will also dominate the occupied area of the implanted communication system.

In this chapter we will introduce some important antenna parameters and requirements for implantable antennas. Furthermore, the interface between the electronics and the antenna will be explicitly discussed. Some measurements and simulations conclude the implantable antenna analysis.

The main objective of this chapter is not to find or design the best antenna for biomedical implants, but to get a firm understanding of how antenna properties are influenced by the human body and what kind of impedance levels and radiation characteristics we can expect. There are PhD reports found in the literature [24, 25] that focus only on the design of an antenna placed in *vacuum*. The design of an *implantable* UWB antenna during the work of this thesis is not feasible. However, since the antenna has so much influence, some important implantable antenna properties have to be known before the electronic circuit can be designed.

3.1. Fundamental Antenna Parameters

Definition of Antenna An antenna is a *transducer* designed to transmit or receive electromagnetic waves. In other words, antennas convert electrical signals into electromagnetic signals and vice versa. The radiation mechanism of any antenna is based on the acceleration of electric *charge*. This creates a time-varying electric field which again gives rise to a magnetic field and both fields propagate away from the antenna with the speed of light in case of free space. Thus, time-varying *currents* will produce radiation. Antenna design is all about influencing the current distribution of a certain structure so that radiation properties such as efficiency, directivity, bandwidth and radiation pattern are met.

Radiation Pattern The relative distribution of the radiated power as a function of the direction in space is defined as the radiation pattern. An *isotropic* radiator radiates

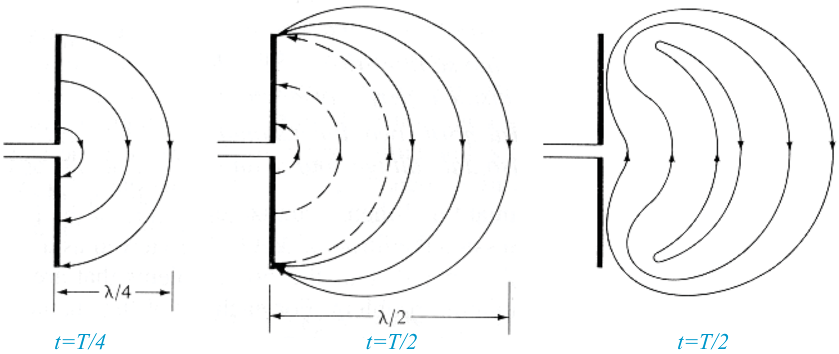

Figure 3.1.: Dipole radiation mechanism.

equally in all directions. The power density of an isotropic radiator is given by $S_{rad} = \frac{P_{rad}}{4\pi r^2}$, where r denotes the distance. The radiation intensity U in a given direction is defined as:

$$U = r^2 S_{rad} \tag{3.1}$$

Directivity Isotropic antennas do not exist in practice but are used to define the directivity of an antenna. If we assume a non-isotropic lossless antenna, then by the law of energy conservation this antenna should radiate or receive more effectively in some directions than in others. The directivity D is the ratio between the radiation intensity in a given direction to the radiation intensity of an isotropic antenna.

$$D = \frac{U_{Antenna}}{U_{Isotropic}} = \frac{4\pi U_{Antenna}}{P_{rad}} \tag{3.2}$$

Efficiency In this thesis, the body and the antenna are seen as one radiating structure. The radiated power is found when integrating the power density over an closed surface with radius r enclosing the radiating structure. A radiated wave inside the body first propagates through the lossy body. Once the wave leaves the body and propagates through air (which we assume to be lossless), the total power inside the closed surface remains constant. The radiated power is defined in the lossless far field so that the efficiency is no longer depending on r. The radiation efficiency is then defined as:

$$Radiation\ efficiency = \frac{Far\ field\ radiated\ power}{Applied\ electrical\ power} \tag{3.3}$$

This includes all power losses and can be separated into ohmic, dielectric and interface losses:

$$e_{total} = e_{cond} e_{dielectric} e_{interface} \tag{3.4}$$

The conductivity efficiency e_{cond} can be computed for simple antenna geometries and is defined as

$$e_{cond} = \frac{R_{rad}}{R_{loss} + R_{rad}} \tag{3.5}$$

The dielectric efficiency $e_{dielectric}$ is more difficult to compute and is usually measured. But after the measurements it is often difficult to separate the conductivity from the dielectric efficiency. Therefore they are usually combined to the e_{cd} efficiency. The interface efficiency $e_{interface}$ is defined as $e_{interface} = 1 - |\Gamma|^2$. Here is Γ the reflection coefficient that describes the impedance mismatch in the antenna-electronics interface.

Gain The gain of an antenna G is closely related to the directivity, but it also takes the antenna efficiency into account. Note that the interface loss is not included.

$$G = e_{cond} e_{dielectric} D \tag{3.6}$$

Bandwidth The bandwidth of an antenna can be considered to be the range of frequencies, on either side of a center frequency, where the antenna characteristics such as input impedance, radiation pattern, directivity and efficiency are within an acceptable value of those at the center frequency. In this thesis the bandwidth is related to the input impedance of the antenna.

Polarization Polarization of a radiated *wave* is defined as "that property of an electromagnetic wave describing the time varying direction and relative magnitude of the electric field vector." The polarization of an *antenna* in a given direction is defined as the polarization of the wave radiated by the antenna. An antenna or wave can be linear, circular or elliptically polarized. If the antenna and the wave do not have the same polarization, the amount of power extracted by the antenna will not be maximized due to the polarization loss factor $PLF = |\rho_w \cdot \rho_a|^2$, where ρ_w and ρ_a are the wave unit and antenna polarization vector, respectively.

Input Impedance The input impedance of an antenna is defined as the ratio of voltage to current seen at the feedpoint terminal, also known as the feedpoint impedance. This impedance can be modeled as $Z_A = R_A + jX_A$ and is dependent on frequency, antenna shape and surrounding environment. The sign of the input reactance depends on the near field predominance of field type: electric (capacitive) or magnetic (inductive). At resonance (zero reactance) the stored energies due to the near fields are equal.

Radiation fields Near and far field can mean different things in different contexts. Defining the boundary between them is depending on the designers perspective and tolerances. For example, the boundary between the near-and far field of a dipole's field can be defined as the distance from the antenna where the reactive and real electric fields are equal. Setting the boundary through wave impedance involves determining where an EM wave impedance becomes "constant". An excellent paper is available which goes through the various definitions and boundaries of near field [27]. In general, the near field of an antenna is the field region where the reactive power dominates the total complex power. This reactive power is not radiated but stored inside the electromagnetic field near the antenna in case of free space.

3.2. Implantable Antenna Requirements

The requirements of an implantable antenna can be described in terms of the fundamental antenna parameters and physical size. In order not to distort the radiated pulse, the input impedance should be constant over frequency. The radiation resistance does not necessarily have to be 50 Ω since we can control the output impedance and signal quantity of the final stage which drives the antenna. Furthermore, high efficiency is of great importance. The antenna engineer can improve the efficiency by altering the antenna shape, material, isolation and choosing a proper electronics-antenna interface.
The required radiation pattern is dependent on the location of the implant. An implant located close underneath the skin can benefit more from a high directive antenna pointing its maximum towards the skin. In this way, less power is absorbed by the tissue behind the implant. Disadvantage is that the received signal strength is more dependent on the location of the patient in the room. In general, high directive antennas are physically larger than antennas with a dipole radiation pattern, making compact directive antennas inefficient.

Designing a physically small implantable antenna with the properties described above is a challenging task, especially in the frequency range of interest in this design. To have an estimation of the maximum allowed antenna dimensions we had a private conversation with neurosurgeon Prof. Dirk de Ridder from the Medical University of Antwerp. From his experience, a maximum dimension of 20x10x2 mm or two stacked 2 euro coins can be inserted into the skull for neurostimulation in the brain. This may seem a lot, but it is roughly the same size of today's pacemakers. The volume occupied by the battery in a pacemaker is about half the total volume. Typical dimensions of an implantable cardiac pacemaker are in the range of 49x46x6 mm [28]. This alows the antenna to be mounted on the backside of the device. We will use these dimensions as a reference throughout this thesis.

3.3. Dependence on Surrounding Environment

All antenna parameters described in Section 3.1 are dependent on wavelength λ and thus are also dependent on the medium since

$$\lambda = \frac{\lambda_0}{\sqrt{\epsilon_r + \frac{\sigma}{j\omega\epsilon_0}}} \tag{3.7}$$

By placing an antenna in a theoretical non-conducting and high permittivity environment extending to infinity, the antenna effectively becomes a factor $\sqrt{\epsilon_r}$ electrically larger compared to the same antenna in free space. That is, the required physically dimensions for a $\lambda/4$ length dipole antenna becomes smaller for the same frequency. This property is widely used to scale down the antennas physical size. Note that this scaling factor is dependent on frequency since ϵ_r varies with frequency as shown in Figure 2.1a on Page 11.

An antenna placed in vacuum has reactive power stored in its near field. If the same antenna is placed in a conductive medium, the reactive power will become partly real since the wavelength becomes a complex number. This can be explained when looking at the complex power moving in the radial direction of an infinite small dipole:

$$P = \eta \frac{\pi}{3} \left| \frac{I_0 l}{\lambda} \right|^2 \left[1 - j \frac{1}{(kr)^3} \right] \tag{3.8}$$

where $k = \frac{2\pi}{\lambda}$ is the wavenumber.

This power does not contribute to the radiation from the antenna and is therefore lost in the near-field. Note that the reactive power *does* flow through the antenna and therefore introduces some losses due to the finite conductivity of the metal, decreasing the efficiency. The power distribution of an antenna in a lossy medium is depicted in Figure 3.2.

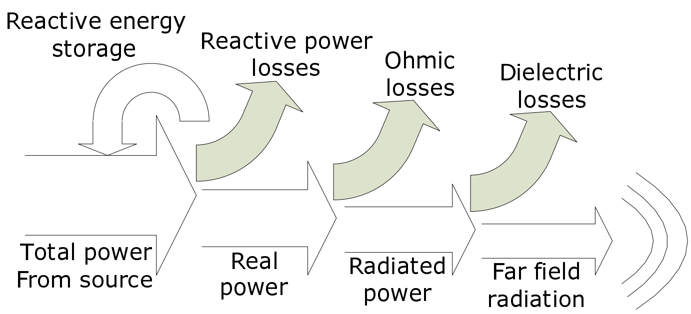

Figure 3.2.: Antenna power distribution.

3.4. Antenna-Electronics Interface

Before we dive into all the implantable antenna details, we will discuss some general but important antenna-electronic interface issues. In this section, the antenna equivalent circuit model with its short comings will be introduced followed by a discussion about information processing in antennas.

3.4.1. Antenna Equivalent Model

If we go back to the definition of an antenna, we know that an antenna is a *transducer*. It relates the terminal voltage and current, related by the impedance of the antenna, to the electromagnetic fields which are related by the wave impedance of the medium.

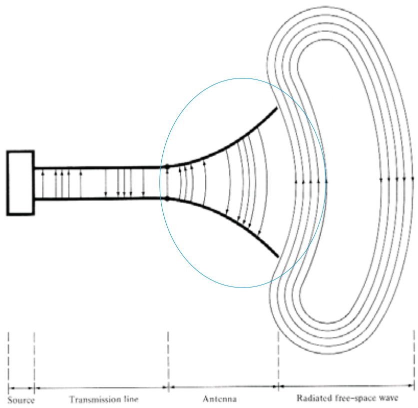

Figure 3.3.: Antenna as a transducer between electronic signals and EM radiation.

The wave impedance of a medium does in general not equal the radiation resistance, so we can think of this transducer as an impedance transformer between the two mediums while the power during the transition ideally remains the same. We could model this with a two port transformer as the electronic equivalent component. However, from an electronic design perspective we are interested in a simple equivalent model consisting of resistances, capacitances and inductances. It has to model the input impedance and corresponding radiated power and not necessarily the physical transition to the medium. Other antenna parameters such as directivity and polarization also do not have to be included in this equivalent circuit model.

Figure 3.4 shows the model of an electric dipole in receiving mode. An incident wave enters the antenna with a certain angle and induces a voltage across the antenna terminal (we assume a omni-directional radiation pattern). This voltage is a function of the E-field and the effective length of the antenna, which depends on the angle θ and the antenna geometry. The antenna has an impedance which relates the voltage and current to the received power and is modeled in series with the induced voltage.

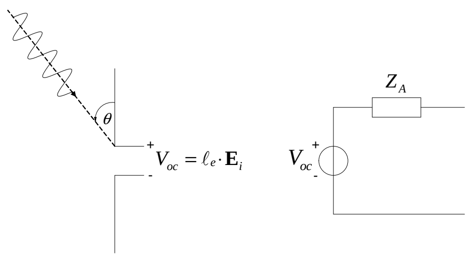

Figure 3.4.: Equivalent circuit of an electric dipole in receiving mode.

By the reciprocity theorem we know that the radiation pattern and impedance of an antenna in receiving and transmitting mode are equal [23]. So the transmitting antenna model is simply equal to the input impedance.

Now we will introduce the shortcomings of these models. First of all, the dielectric losses cannot be represented by simply adding another series resistance to this model. These losses have to be simulated with the antenna inside the lossy medium. This will be dealt with in Section 3.7. The problem with this antenna model arises when one wants to calculate the power. From basic circuit theory, we can also represent the antenna model as its Norton equivalent circuit as shown in Figure 3.5.

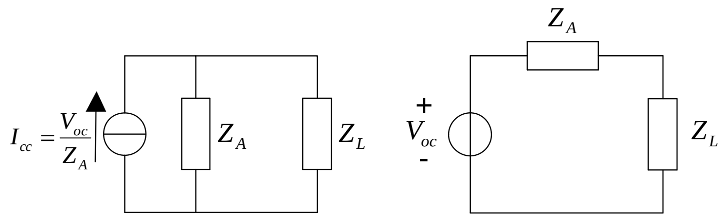

(a) Norton equivalent circuit (b) Thévenin equivalent circuit

Figure 3.5.: Equivalent antenna models in receiving mode.

The power in the load, calculated using the Norton and Thévenin equivalent circuit is given by

$$P_L = \frac{1}{2}\left|\frac{V_{oc}}{Z_L + Z_A}\right|^2 Re\{Z_L\} \tag{3.9}$$

As expected, both equivalent circuits give the same result. If we now calculate the power dissipated inside the antenna using the Norton equivalent circuit we find

$$P_{A,Norton} = \frac{1}{2}\left|\frac{V_{oc}}{Z_L + Z_A}\right|^2 \left|\frac{Z_L}{Z_A}\right|^2 Re\{Z_A\} \tag{3.10}$$

while using the Thévenin equivalent circuit results in

$$P_{A,Thévenin} = \frac{1}{2}\left|\frac{V_{oc}}{Z_L + Z_A}\right|^2 Re\{Z_A\} \tag{3.11}$$

Note that the internal power dissipation calculated using the two models are equal *only* when $Z_L = Z_A$. Many antenna textbooks consider the internal power dissipation as re-radiated power. But this analysis shows that Norton and Thévenin circuits only describe the correct voltages and currents at the terminals and cannot rely for calculating the internal power dissipation.

Another interesting case is the open and shorted receiving antenna. If the receiving antenna is open circuited, then there is no internal power dissipation in the Thévenin equivalent circuit, which suggests that the antenna does not re-radiated any power. On the contrary, the Norton equivalent circuit does have internal dissipated power, even when the receiving antenna is open circuited. There is no power conservation theorem associated with these equivalent circuits, while power transfer seems to be the main concern for most antenna and RF engineers. Allan W. Love developed an interesting constant-power generating circuit for a receiving antenna which combines a Norton and Thévenin circuit [37]. The sources and impedances are a function of antenna geometry and the incident EM wave. This paper assumes that maximum power in the load is the desired signal quantity. However, we will see that for some applications this might not be the best choice.

3.4.2. Integration of chip into antenna

In this design the antenna and electronics will be integrated into one system. Figure 3.6 shows an example of a pulse generator on chip integrated into an UWB antenna. The pulse generator is connected to the antenna flairs using copper vias. This antenna-electronics interface has several advantages. First of all, the total area of the communication system is reduced. Secondly, there is no need of any transmission line or a balun between the antenna and generator. This is possible since the physical length from chip to antenna is only a few mm. In other words, working below 1 GHz allows us to assume that the voltage and current along the wire are constant and we do not have to be concerned about propagation effects.

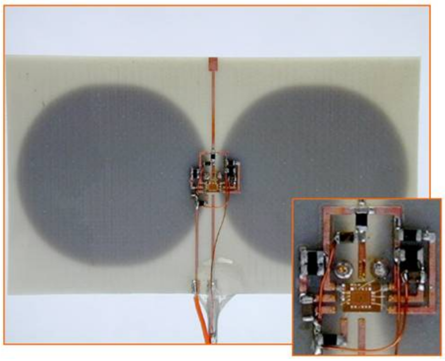

Figure 3.6.: Integration of a pulse generator on chip into an UWB antenna [25, 26].

Eliminating the need for a transmission line also reduces common mode radiation. This type of radiation is caused by common mode currents on the cable, making the cable act as part of the antenna. When common mode current becomes comparable in magnitude to the differential mode current it can change the antenna radiation characteristics. Finally, the antenna-electronics interface is not limited by the conventional $50\,\Omega$ characteristic impedance. We can freely *choose* a convenient interface and output stage which drives the antenna with the appropriate signal quantity. In this way we can design the most reliable and efficient interface for this application. This approach is completely different from conventional antenna designs where antennas are impedance matched to a generator with a fixed impedance.

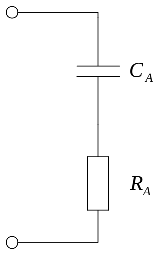

Figure 3.7.: Small electric dipole equivalent circuit model

3.4.3. Information processing

One must realize that analog circuit design deals with the transfer of *information*. Current, voltage and power are fundamental circuit signal quantities and the designer has to choose which quantity represents the information in the most accurate way. A proper characterization of the antenna is required since knowledge about the source and load impedance is of high importance. The required impedance of a LNA, antenna or generator is frequently assumed to be $50\,\Omega$ without any further discussion. We will look for an alternative solution which might be superior to the standard way of terminating an antenna.

As a thought experiment we will use the equivalent circuit of a small electric dipole depicted in Figure 3.7. The physical information is represented by the power in the radiation resistance R_A, which can be delivered by an impedance matched power, current or voltage source, all three shown in Figure 3.8. First we will consider this antenna to be power driven (impedance matched).

Power driven

Conjugate impedance matching between the antenna and source or load is frequently used to obtain maximum power transfer. Another reason is to avoid reflections in transmission lines, which can simultaneously be achieved by using the same impedance match condition for maximum power. Transmission lines are used when the wavelength of the signal becomes comparable or less than the physical length of the wire. At this length, the amplitude of the signal varies along the wire. These propagation effects can cause interference which is not taken into account when using basic circuit theory.

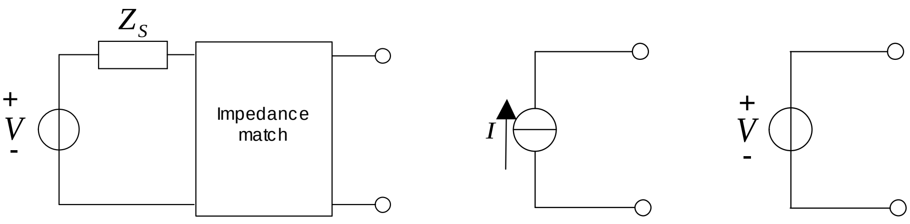

(a) Power (b) Current (c) Voltage

Figure 3.8.: Antenna driving signal quantities

However, there are no propagation effect in this design since the physical length from chip to antenna is only a few mm. The demand to maximize power transfer also does not apply in this design. Though it may be convenient from a measurement point of view to standardize on characteristic impedances, there seems to be no fundamental reason why an antenna should be terminated for optimum power transfer. Actually, power transfer is a very inefficient way of signal processing since at each interface, half of the available signal power is lost. Also, the transfer becomes sensitive to a lot of parameters since the voltage and current become functions of the source impedance, matching network and antenna impedance. Since the electrical properties of the human body can vary considerably, it is expected that this can cause problems for implantable medical devices. The performance of the wireless link should not rely on how well the antenna is impedance matched. Hence, we must investigate other, more reliable and efficient antenna-electronics interfaces.

Voltage and current driven

Since power transfer is not a reliable and efficient way of signal processing, we will investigate the possibility of driving the antenna with an ideal voltage and current source. When looking at the model in Figure 3.7, it suggests to drive it with a *current.* This guarantees that the desired power is always delivered to the radiation resistance, independent of the reactance. On the contrary, when the antenna is voltage driven, the power delivered to the resistance becomes dependent on the capacitance and on frequency. This creates the undesirable property of a frequency selective antenna-electronics interface.

A current driven antenna thus sounds very promising. Also, it is very compatible since most active devices which we know today are natural current sources. But still, the majority of antenna designs are terminated with a conjugate impedance matched source, even at low frequencies. This may be a result of the 'standard 50 Ω tradition' way to terminate an antenna since most generators and transmission lines are 50 Ω. The validity of this simple thought experiment will be verified with antenna simulations in Section 3.7.

Note that in a different situation, a current driven antenna might *not* be the best solution at all. For example, if the equivalent circuit of the antenna takes the form of a parallel network within the desired frequency range, it should be considered to drive this antenna with a voltage source.

Antenna in receiving mode

To complete the full picture of a communication system, the information processing in a electrically small receiving antenna will also be discussed briefly. Again, the common way to do this is to conjugate match the antenna to the LNA. But since the reactance is usually much larger than the radiation resistance for small antennas, it is difficult to extract any power from the antenna. With the same reasoning as before we investigate the possibility to extract the information from another signal quantity. Referring to Figure 3.4 on page 26, we know that the information is represented by the terminal voltage in case of an electric dipole. This means that the voltage has to be sensed with a high impedance voltage sensor, for example by means of a negative feedback amplifier. In this way the terminal voltage can be amplified with a fixed gain which is virtually independent of the antenna impedance.

Since modern LNAs are implemented with CMOS transistors (which are natural voltage sensors), we can assume that eventually the voltage will be measured. In the case of a conjugate impedance matched antenna, the voltage across the LNA will be half compared to the directly negative feedback voltage sensing. Thus by choosing the appropriate signal quantity, the signal strength has increased by a factor of two. In addition, when using a voltage sensor to extract information from the EM wave, no signal is lost in the interface between the antenna and the receiver, which is the case in impedance matched systems.

The same holds for other antennas, although it may be more convenient to sense the current rather than the voltage. An example is the magnetic dipole (loop antenna) where the current induced in the loop is related to the magnetic field. It can be more advantageous to measure this current by creating a short circuit with a current sensor. A magnetic dipole terminated with different loads has been simulated in [38]. Sensing the current instead of the voltage or power indeed improved the performance in terms of amplitude and bandwidth. So by using the appropriate model and sensing the right signal quantity one can improve the performance. Of course, this only applies if there are no propagation effects along the wire. If reflections in the transmission line are the cause of unacceptable interference, the antenna will have to be terminated with an impedance matched load at the expense of reduced performance.

3.5. Antenna type

A decision has to be made concerning the antenna type to be used during this research. A lossless electric dipole is less power efficient as an implantable antenna compared to the lossless magnetic dipole [6]. This is due to the fact that the E-field near the antenna of an electric dipole is stronger with respect to the magnetic dipole, resulting in more reactive power loss in the body. However, in practice this is compensated by the much lower ohmic losses since the electric dipole has a higher radiation resistance compared to the the magnetic dipole. Some recently reported narrowband implantable antennas are summarized in Table 3.1. All antennas fall within the maximum dimensions of two stacked 2 euro coins, but cannot easily be compared on gain and bandwidth because of the different tissue models being used.

Table 3.1.: Recently reported implantable antennas.

Frequency (MHz)	Size (mm)	Gain (dB)	Antenna type	Paper
377-427	πx7.5^{2}x1.9	-26	Stacked spiral	[8]
392-409	78.5	N/A	Circumference	[32]
400-510	10.5x10.5x3	N/A	Spiral	[31]
402-405	26.6x16.8x3	-35	Spiral	[9]
402-405	N/A	-14	Patch	[45]
402-405	8.2x8.1x1	-25	Square loop	[7]
411-600	πx10^{2}x7	-10	Dual Spiral	[33]
916-920	8.25x8.25x0.6	N/A	Microstrip spiral	[30]
3500-4500	28.7x15x0.5	-22.77	Patch	[47]
31000-32000	3.39x2.66x0.254	-46.5	Patch	[46]

All these antennas use miniaturization techniques to achieve the smallest antenna size possible while maintaining acceptable performance. However, there is a fundamental limit which keeps the antenna designer from further improving the performance. To obtain an even smaller antenna operating at low frequencies, it is necessary to look for alternative ways. In [34], a very interesting MEMS antenna was designed which measures the magnetic field with a cantilever structure using the Lorentz force on a current carrying lead. In this way, an extremely compact antenna with electrically controlled gain can be realized. Disadvantage is that this structure can only be used as a receiving antenna and the power consumption is much too high for biomedical applications.

Since no other alternatives solutions were found, we still have to use conventional antennas. Unfortunately we could not find any reported sub-GHz implantable antenna with a bandwidth greater than 200 MHz, so free space UWB antennas where investigated to be used as an implantable antenna. In [35], an effective miniature technique is reported where inductive loading was used by coiling the spiral arm such that the arm resembles a solenoid. In this way approximately 10 dB improvement in gain was achieving on the lower band frequency. However, the design, simulation and manufacturing of this antenna would take too much time and is outside the scope of this thesis.

Because of the large variety of published papers on planar UWB dipole antennas [29, 36, 24, 25], we decided to investigate this type of antenna. These antennas have good performance in terms of input impedance, gain and efficiency. Moreover, these type of antennas are very compact, making them ideal to be mounted on the side of the implant or battery. Since all antennas in these papers where designed to operate in free space, we have to investigate if they are also suitable as implantable antennas.

To answer this question, we fabricated various planar UWB dipole antennas on a FR4 Printed Circuit Board (PCB) using [36] as a reference to determine the dimensions of each antenna type. The dimension of the PCB are 26x26x1.6 mm, roughly the size of a 2 euro coin. The PEMA 2 antenna dimensions in Figure 3.9a are: F=2mm, G=1mm, L=7mm, H=2mm, R=8mm. The typical electrical properties of the used PCB are $\epsilon_r = 4.3$ and loss parameter $\tan\delta = 0.01$ at 1 GHz. These antennas are used to measure

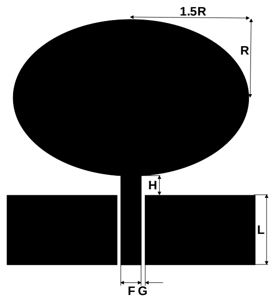

(a) PEMA 2 antenna dimensions.

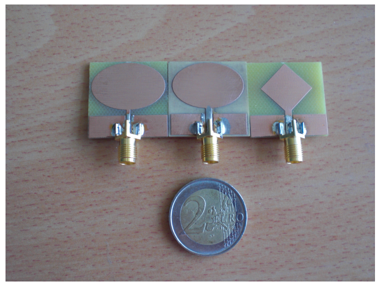

(b) Variety of fabricated antennas.

Figure 3.9.: Planar UWB dipole antennas.

the input impedance when they are located inside a lossy and high permittivity medium.

3.6. Measurements

Small dipole antennas can be analyzed well because of their simple geometry. UWB antennas usually have more complex geometries so that only a limited number of practical antennas have been investigated analytically. For many others, the input impedance has to be determined experimentally. This has also been done in this work. We used muscle simulating liquid and raw pork meat to represent the human body. The simulating liquid consists of de-ionized water, sugar, salt and hydroxyethylcellulose (HEC), where the percentage of each ingredient is given in Table 3.2. This liquid can be used for

Table 3.2.: Muscle simulating liquid ingredients for 0.1-1GHz [40].

De-ionized water	Sugar	Salt	HEC
52.4%	45%	1.5%	1%

simulating muscle tissue for 100MHz - 1GHz. The solution has to be altered for higher frequencies. The measurements taken in [39] show that raw pork meat has a good agreement with the electrical properties of the muscle simulating liquid.

S-parameter measurements where done using an Anritsu 37397D vector analyzer which covers a frequency range of 40 MHz - 65 GHz. The worst case reflection magnitude and phase uncertainty are depending on the antennas $|S_{11}|$. These specifications can be found in the Anritsu 37000D technical datasheet [41]. Calibration was done to remove the influence of the 50 Ω transmission line.

To isolate the antenna from the lossy medium, the antennas where inserted in a thin balloon. Measurements showed that the input impedance of the antenna in free space with and without balloon where almost identical. When the antenna is placed inside the

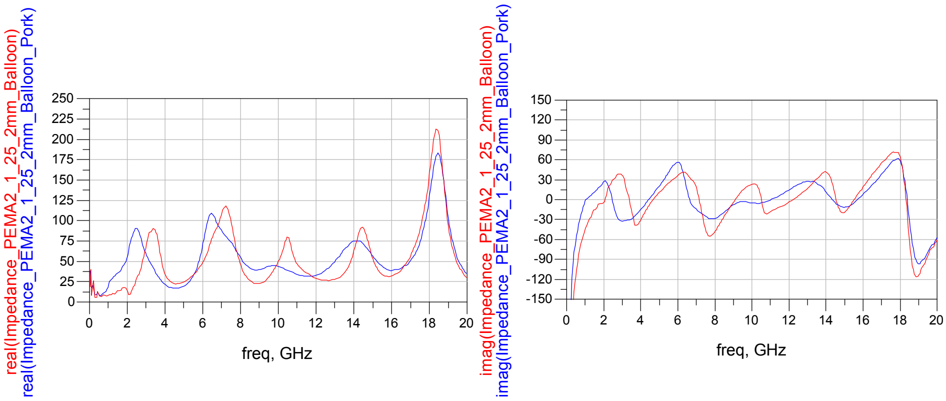

(a) Real (b) Imaginary

Figure 3.10.: Measured antenna impedance in pork (blue) and free space (red).

raw pork meat, the impedance should shift down in frequency by a theoretical factor of $\sqrt{\varepsilon_r}$. However, the measured impedance in Figure 3.10 show that the frequency shift is significantly less. The permittivity of muscle is frequency dependent, but always higher than $\varepsilon_r = 40$ for frequencies below 10 GHz, which should shift the impedance by a factor of 6.3 or more. This deviation can be explained by the fact that the pork meat is a finite medium. This in combination with the balloon as isolation can be the cause of this reduced frequency shift.

Equivalent Circuit Model

Since we are interested in frequencies below 1 GHz, the measurements of various antennas inserted in pork meat and simulating liquid are shown in Figure 3.11. Note that the

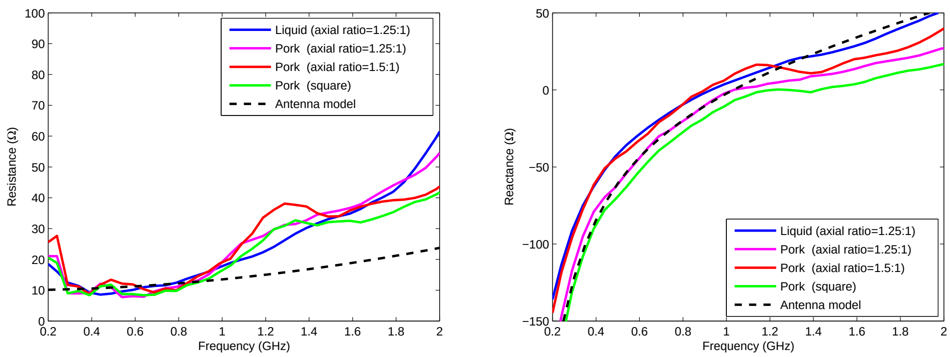

(a) Measured real impedance (b) Measured imaginary impedance

Figure 3.11.: Various measured antenna impedances in pork and muscle simulating liquid.

measured resistance of the various antennas do not vary as much at these frequencies and that the resistance is significantly smaller compared to the reactance, which is to be expected of an electrically small antenna (ESA). Also, the resistance is almost constant over a frequency range of 300-900 MHz for all antennas. The reactance varies more over all antenna measurements. This suggests not to impedance match this antenna because of the unpredictable variations of the implantable antenna, making it hard to have a good impedance match. These variations in reactance will have little or no effect on the radiated power nor pulse shape when the antenna is current driven.

An equivalent RLC circuit has been developed to model the antenna's impedance in the frequency range of 300-900 MHz. The dotted black line in Figure 3.11 is the impedance of the equivalent circuit depicted in Figure 3.12, which is sufficient to model the antennas impedance in the desired frequency range.

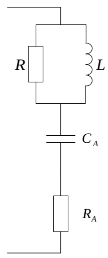

Figure 3.12.: Antenna equivalent circuit model for 300-900 MHz, $R_A = 10\,\Omega$, $C_A = 4\,pF$, $R = 400\,\Omega$, $L = 6\,nH$.

Measurement Inaccuracy

The inaccuracy of these measurements can be determined with the Anritsu 37397D vector analyzer specifications. The maximum measured $|S_{11}|$ of the antenna is approximately -2.8 dB. This is the result of the large mismatch between the antenna impedance and the characteristic impedance of the measurement setup.

The measurement inaccuracy and absolute error calculations of ΔZ_{in} can be found in Appendix B. The S parameter inaccuracy in these measurements was $\Delta\,|S_{11}| = 0.5\,dB$ and $\Delta\varphi = 2°$. The calculated absolute and relative error in the measured resistance and reactance is shown in Figure 3.13. The absolute resistance error from 500 MHz to 1 GHz is approximately $3\,\Omega$. Since the measured resistance is in the order of $10\,\Omega$, the relative inaccuracy is high, starting from 30% at 500 MHz and drops down to 15% at 1 GHz. The sudden increased relative reactance error around 900 MHz is due to the fact that the reactance is changing from capacitive to inductive, causing an infinite error at that frequency.

Note that these errors are worst case contributions of the analyzers residual directivity, load and source match, frequency response, isolation, dynamic accuracy and connector repeatability. Nevertheless, it shows that the measured impedance level inaccuracy can be considerably high. Furthermore, these measurements do not give any insight on other important antenna properties such as efficiency and radiation pattern. We will continue

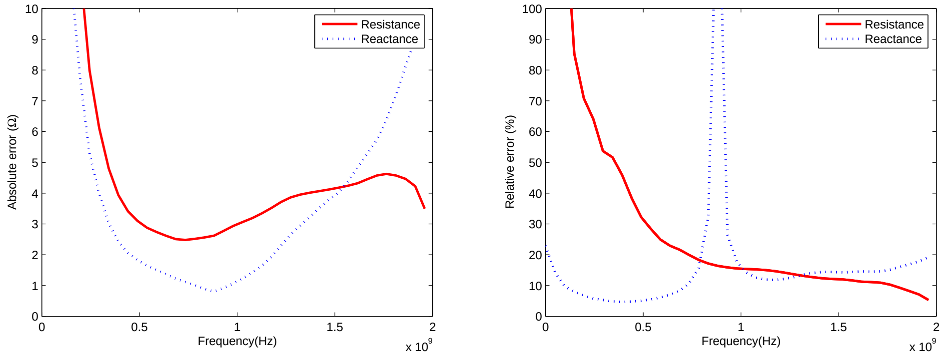

(a) Absolute error ΔZ_{in}. (b) Relative error $\frac{\Delta Z_{in}}{Z_{in}}$.

Figure 3.13.: Calculated worst case impedance inaccuracy.

this research by simulating the antenna in a multi-layered tissue model. In this way, the measured and simulated impedances can be compared so that we can have an estimation of the antenna performance inside the human body.

3.7. Simulations

The antenna measurements in the previous section showed that the input resistance from 300-900 MHz is approximately $10\,\Omega$, which is much lower than conventional $50\,\Omega$ antenna designs. In the literature, these electrical small antennas are often referred to be inefficient radiators because of their low radiation resistance and large reactance which makes them difficult to match. In this section we will investigate if this also holds for this design. Also, the radiation pattern and antenna-electronics interface will be simulated to completely characterize the implantable antenna.

The simulations have been performed using Computer Simulation Technology (CST) Microwave Studio 5.0.2. on an Intel 1.66 GHz dual core processor with 2.5 GB RAM memory. CST Microwave Studio uses the Finite Elements Method (FEM) which is a numerical technique used for finding approximate solutions of partial differential equations and integral equations. This software can be used to determine the input impedance and the corresponding radiation pattern at various frequencies. Another useful feature build into CST is the ability to simulate the SAR of a given structure, making this software very useful for this application.

The antenna used in the simulations is shown in Figure 3.14. This type of antenna has similar performance as the antenna with ground plane used in the measurements, but is easier to simulate in CST by using a discrete port between the two flares. The antennas used in the measurements are easier to fabricate and to measure. The dimensions of the simulated antenna are 20x32x1.6mm, where the copper layer has a conductivity of 60e6 S/m and the FR4 substrate a loss tangent of 0.01 @ 1 GHz. The density of the substrate is 1910 kg/m^3.

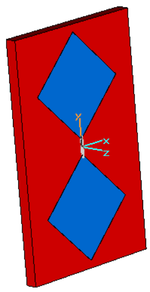

Figure 3.14.: Simulated UWB antenna.

3.7.1. Antenna in free space

The antenna will be simulated first in free space to determine its efficiency and radiation pattern. At 2.2 GHz, the input resistance equals 10 Ω, roughly equal to the resistance of the antenna when inserted inside the body at 500 MHz. Figure 3.15 shows that the antenna has an omni-directional radiation pattern with a maximum directivity of 1.55 pointed at broadside, which is to be expected of a dipole antenna. Moreover, it shows

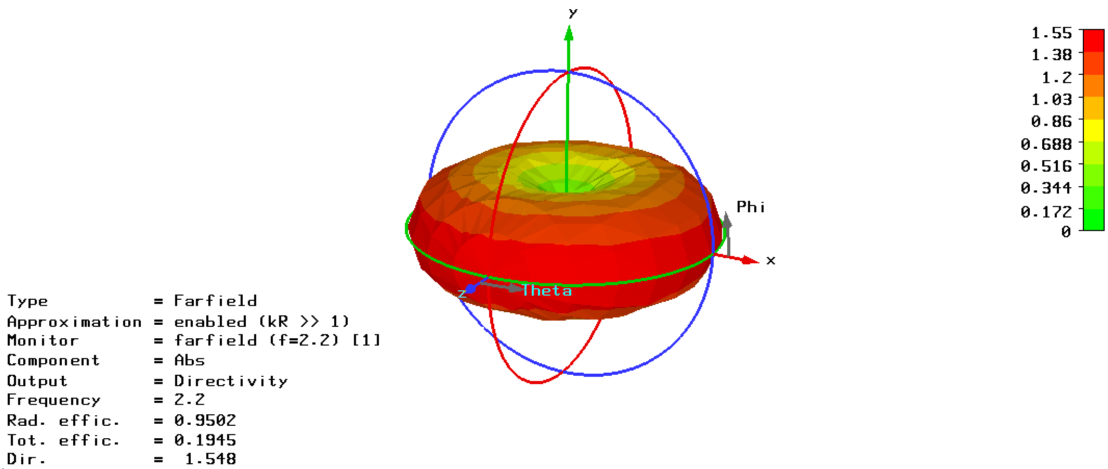

Figure 3.15.: Radiation pattern of an ESA at 2.2 GHz.

that the antenna *itself* is a very efficient radiator despite its low input resistance. The *radiation* efficiency equals 95% while the *total* efficiency, which includes the external impedance mismatch, is only 19.45%. From this simulation we can conclude that the ohmic losses are small ($R_{Loss} \approx 0.5\ \Omega$). The losses in the interface between the source and antenna dominates the total efficiency.

The thought experiment in Section 3.4 showed that a current driven antenna was the optimum interface in terms of efficiency and reliability. To validate this, the antenna was simulated with a current, voltage and power source (50 Ω). The available source power in CST is fixed to 1 Watt peak, Microwave studio does not allow to change this value when using a power source. To compare the three possible interfaces, the voltage and current sources were given the right values to also deliver 1 Watt to the antenna at the *resonance frequency*. The simulations showed that the antenna performance of the three different driving quantities were *identical*. This is to be expected since the input impedance is purely real. At frequencies where the input impedance became complex, the current driven antenna indeed was superior to the voltage and power driven antenna since the delivered power was not depending on the reactance. The radiated power of the voltage and power driven (impedance matched) antenna will always be less than or equal to the current driven antenna. Hence, the antenna is this design will be current driven because this results in the most efficient en reliable interface.

3.7.2. Implantable antenna

Now that the antenna efficiency, radiation pattern in free space and optimum interface is known, the antenna can be simulated inside the layered tissue structure. The same

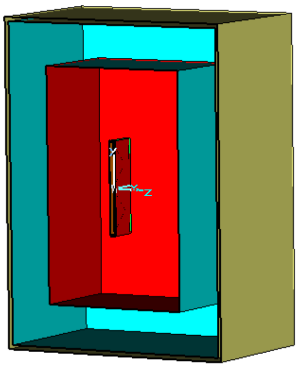

Figure 3.16.: Intersection view of antenna surrounded by multiple tissue layers consisting muscle (25mm), fat (15mm) and skin (1.5mm) simulated in CST.

tissue model used in Section 2.3 was used so that the influence of the antenna can be investigated and compared to the analytical results. A 2nd order Debye model was used to model the tissues characteristics for the different tissues which can be found in [42]. The tissue volume is 104x116x84.5 mm with a weight of 0.983 kg. To make the simulation as realistic as possible, the antenna was isolated inside a cavity which represents the balloon in the measurements. The thickness of a non-conducting insulation will influence the antenna efficiency as investigated in [6]. However, we did not investigate this any further and will leave this optimization to the antenna expert. The isolation layer was given a thickness of 1 mm and permittivity of $\epsilon_r = 2$ as this showed a high degree of similarity with the measured input impedance.

First, the antenna is simulated with a 50 Ω port impedance to investigate the difference in interface losses with respect to a voltage and current driven antenna. Figure 3.17a shows the simulated radiation and total efficiency versus frequency. It is evident that the optimum operating frequency lies higher than the calculated 600 MHz in Section 2.3.2. This difference can be explained by the fact that analytical results in Section 2.3.2 where obtained without taking the antenna gain into account. In CST microwave studio the total efficiency is defined as the ratio of radiated to stimulated power of the antenna. This explains the large difference in total and radiation efficiency, the radiation efficiency does not include the impedance mismatch with the 50 Ω port impedance, the total efficiency does. The total efficiency can be improved by using an impedance matching network. However, an UWB impedance match can be difficult to realize without introducing a penalty in another design aspect.

When the antenna is current driven, the total efficiency will equal the radiation efficiency, which has a maximum of approximately 3.5% at 800 MHz. The work done in [45]

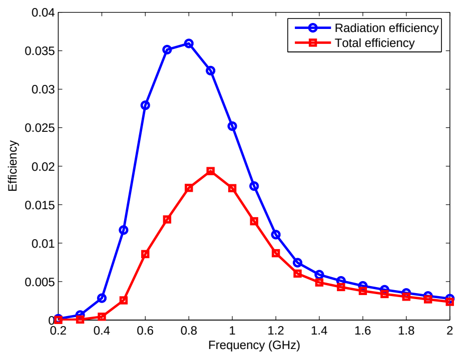

(a) Radiation and total efficiency.

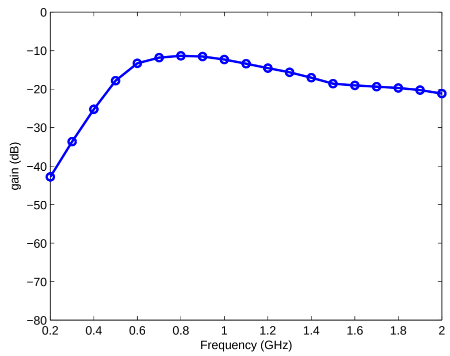

(b) Maximum gain (dBi).

Figure 3.17.: Simulated implantable antenna efficiency.

shows similar simulation and measurement results at 403.5 MHz, where an implanted patch antenna exhibits an efficiency of 3.41%.

The maximum antenna gain in Figure 3.17b is approximately -12 dB and is independent of the driving source because the antenna gain is defined as the ratio between the radiated power and the delivered power in a certain direction and does not include the interface losses.

This graph therefore does not include the *true* signal transfer from source to radiated power. To include the influence of the source's signal quantity, we define the interface signal reduction factor δ which includes any reduction of the signal along the path between the source and the antenna resistance. It is defined as the ratio between delivered power of the ideal signal transfer where there is no signal loss (no source impedance, no reactance) and the real transfer.

$$\delta = \frac{P_{Del,ideal}}{P_{Del,real}} \tag{3.12}$$

For a voltage driven antenna, the voltage is divided between the reactance and the resistance so the interface signal reduction becomes:

$$\delta_{voltage} = 1 + \left(\frac{X_A}{R_A}\right)^2 \tag{3.13}$$

A current driven antenna does not suffer from any signal reduction in the interface:

$$\delta_{current} = 1 \tag{3.14}$$

The power driven antenna suffers the most from reduction along the signal path due to the extra source impedance. For this analysis we used a voltage source in series with a source impedance R_S.

$$\delta_{power} = 1 + \left(\frac{R_S}{R_A}\right)^2 + \left(\frac{X_A}{R_A}\right)^2 + 2\frac{R_S}{R_A} \tag{3.15}$$

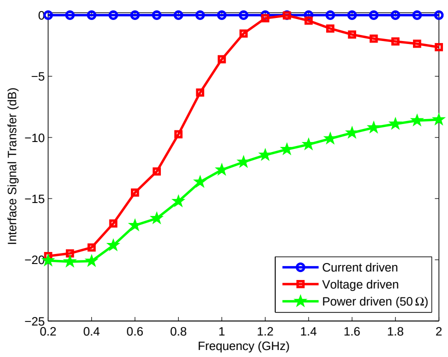

(a) Source-antenna signal transfer.

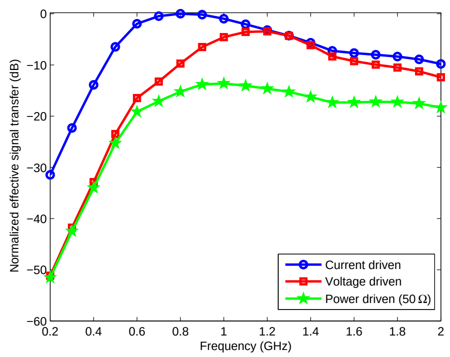

(b) Normalized effective signal transfer.

Figure 3.18.: Interface and total effective signal transfer.

Figure 3.18a shows the signal transfer δ^{-1} for each interface. The voltage driven antenna equals the current driven antenna only at the resonance frequency. The power driven antenna has an additional loss factor due to the source resistance.

The total effective signal transfer is the combination of the interface signal transfer and the antenna gain. The normalized effective signal transfer of each configuration is shown in Figure 3.18b. Clearly, the current driven antenna is preferred since it offers the highest effective signal transfer, especially at low frequencies. These results have been verified with simulated current, voltage and power driven antennas.

It must be noted that no impedance matching network has been used for the power driven antenna. However, the maximum signal transfer will never be higher than a current driven antenna, even with an ideally impedance matched antenna.

The maximum gain used to calculate the effective signal transfer is obtained from the radiation pattern. The change in radiation pattern over frequency is shown in Appendix C. The radiation pattern deviates from a typical dipole pattern for frequencies higher than 1 GHz, while the variation for frequencies below 1 GHz is considerably less. This is another good argument to use UWB communication at low frequencies.

Of course, all these antenna characteristics will vary with the patient. These variations must be taken into account with the link budget calculations.

Now that the antenna is characterized, the operating bandwidth can be determined.

3.7.3. Bandwidth

When looking at Figure 3.18b it can be seen that signals below 500 MHz are heavily attenuated. Signals below this frequency will have almost no contribution to the radiated power. Hence, an operating frequency bandwidth of 500-960 MHz will be used during this design.

3.7.4. Specific Absorption Rate

At this point in the design, it is still unknown what power level should be used. This will depend on the pulse shape, link budget and battery capacity. Once this is known, the SAR levels can be determined.

3.7.5. Group Delay

Group delay is the measure of a signal transition time through a device. It is defined as the negative derivative of phase versus frequency given by

$$Group\,Delay = -\frac{\partial\varphi\left(\omega\right)}{\partial\omega} \tag{3.16}$$

A linear phase results in a flat group delay so that all frequency components experience the same delay. A non-flat group delay in practical UWB systems can cause timing errors at the receiver. The maximum variation of the group delay within the operating frequency band should be less than the pulse duration [25]. Simulations showed that the maximum variation in group delay in the frequency range of 500-960 MHz for this implantable antenna is 78 ps. Since the pulse duration in this design is in the order of nanoseconds, it is expected that a transmitted pulse will not be seriously distorted due to the group delay.

3.8. Summary

In this chapter the antenna characteristics and optimum electronics-antenna interface where investigated for implantable devices. First, the definition and requirements for implantable antennas where discussed. Then, it was shown that the often used antenna equivalent circuit models are not always valid, especially the equivalent model for a receiving antenna. This led to the discussion of impedance matched antennas, which turned out not always to be the best solution. It was found that a *current* driven antenna offers the highest degree of reliability and efficiency for this particular application since the desired radiated power is *always* delivered to the antenna, independent of the antenna reactance. The performance of conventional 50 Ω antennas are more sensitive to variations in the environment since they rely on how well the antenna is impedance matched.

Various UWB electric dipole antennas were build and immersed into muscle simulating liquid and raw pork meat to measure the input impedance of an implantable antenna. The result of these measurements was that all antennas showed a highly similar input resistance between 300-900 MHz. The variation in antenna reactance was more compared to the variations in antenna resistance. With these findings, an equivalent circuit model was developed which is valid in this frequency range. To investigate other antenna characteristics such as gain, efficiency and radiation pattern, a similar antenna was simulated in CST Microwave Studio using a tissue model consisting of muscle, fat and skin. Although the radiation resistance is low, in the order of 10 Ω, simulations showed that the ohmic losses are acceptable and that the antenna itself is an efficient radiator. Simulations confirmed that a current driven antenna offers the most reliable and the highest effective signal transfer. The implantable antenna has an omnidirectional radiation pattern below 1 GHz, but quickly deviates from this typical dipole pattern with increasing frequency. The gain, directivity, and efficiency will vary with the patient so these variations must be taken into account with the link budget calculations.

It was decided to set the lower operating frequency to 500 MHz, as signals below this frequency will almost not contribute to the radiated power. Finally, it was shown that group delay is of no importance for this design since the maximum variation in group delay is only 78 ps.

4. System Design

Sub-GHz UWB communication applied to implantable medical devices is a new concept, meaning that there are no specifications given yet. These specifications have to be obtained before the circuit level design phase. In previous chapters, specifications such as bandwidth, antenna size and maximum allowed SAR where found. The remaining specifications will be derived in this chapter. With these design specifications, a realistic link budget will be created. Finally, the RF electromagnetic energy arbsorption in the tissue will be discussed.

4.1. Design Philosophy

It is essential to keep the power consumption of the implant as low as possible, whereas the base station is allowed to consume much more power. This suggests to shift the complexity in the wireless link from the implant to the base station as much as possible. Complex signal processing can be performed at the base station to detect the transmitted pulses and reconstruct the data. The transmitter can be switched off most of the time while data is being accumulated. After accumulating, the transmitter is turned on and transmits a burst of short pulses. During the time laps between two pulses the transmitter can be switched off so that only power is being consumed while generating a pulse. This is the reason why UWB wireless communication can be much more power efficient compared to narrowband communication. To further maximize the battery life, the transmitter should be designed to minimize the energy consumed per transmitter pulse.

The base station can also be used as a calibration tool to wirelessly correct the center frequency or pulse amplitude if needed. In such a system, the base station monitors the pulse characteristics and sends information back to the implant to correct the frequency or amplitude. During the design it should also be kept in mind that reliability is highly important. This includes a realistic link budget, as well as circuit robustness against process and temperature variations.

4.2. Transmitter Architecture

The proposed UWB transmitter depicted in Figure 4.1 consists of a timing stage, pulse generator, output stage and antenna. It is assumed that the transmitter is part of a larger system which includes a power management subsystem which deliveres a stable power supply.

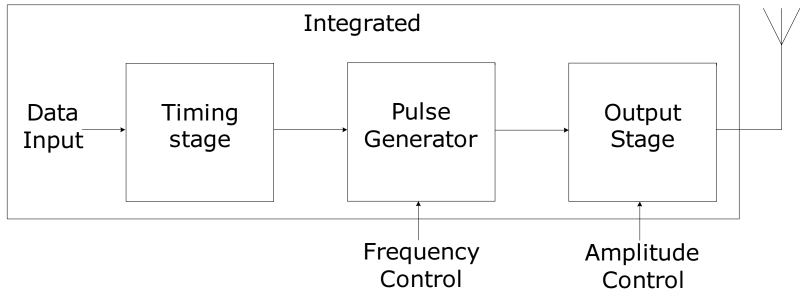

Figure 4.1.: Proposed UWB transmitter architecture.

Timing Stage

A timing stage modifies the input data such that it can control the pulse generator. This will depend on the type of modulation and pulse generator implementation. Further requirements will follow when the pulse generator architecture is known. We will discuss this in the next chapter.

Pulse Generator

To minimize power, the pulse generator should only consume power when a pulse is being generated. Hence, the generator must be able to be switched on and off rapidly. It is also required to have frequency control to adjust the desired operating frequency and, if required, to compensate for any process corner and device mismatch. With operating frequency we mean the pulse center frequency of the main radiation lobe seen in the power spectral density. Furthermore, it is highly desired if the pulse generator can generate pulses with different phases. Binary Phase Shift Keying (BPSK) makes use of two signals separated by 180°. This modulation scheme has a 3 dB improvement in bit error performance compared to On-Off Keying (OOK).

Output Stage

The output stage has to sense the output signal quantity of the pulse generator and convert it to a current which directly drives the antenna. Because this stage has to deliver a high peak current, the main focus will be on power efficiency. It also has to be able to switch on and off at the same rate as the pulse generator. Furthermore, it is desired to compensate the power loss variations in the channel by making the output stage variable in gain. This can also be used to comply with the FCC mask or the reduce power consumption.

4.3. Design Specifications

A realistic link budget is an important step towards a reliable communication system. Variables such as bitrate, battery capacity, environment loss and receiver architecture all have influence on the link budget. This section will address all these variables.

4.3.1. Bitrate

The required bitrate depends on the application. Typical biomedical data today does not require dozens of Mb/s since the amount of data is usually kept to a minimum to save power. In December 2009, Zarlink brought one of the first medical implantable RF transceiver into the market [48]. This transceiver operates in the 402-405 MHz band and supports a raw data rate up to 800 kb/s while consuming 12.5 mW. UWB can achieve the same data rate while consuming only a small fraction of this power. Nevertheless, a trade-off has to be made between bitrate and power consumption. To keep the power consumption to a minimum, we aim for a bitrate of 1 Mb/s. A low bitrate also directly translates to low average emission level, which relaxes the constrains to meet the FCC mask. A higher bitrate is possible, but is limited by the FCC mask and the duration of the pulse itself.

4.3.2. Wireless Link Range

UWB is only beneficial for short distances, which typically limits the range to several meters. For the patients convenience, it is required that the wireless link between the implant and the external base station covers an average sized room. In this design, we aim for a distance of 5 meter. This can be extended to 10 meter, which increases the path loss with an additional 6 dB.

4.3.3. UWB Path Loss

The path loss can be found when considering a transmitting and receiving antenna in free space separated by distance r. When the transmitting antenna radiates power P_{Tx}, then at distance r the power density equals $S = \frac{P_{Tx}}{4\pi r^2} G_{Tx}\ \left[\mathrm{W/m^2}\right]$. G_{Tx} denotes the transmitting antenna gain. The power in the antenna load P_{Rx} extracted from the antenna can be obtained by multiplying the incoming power density S with the effective area $A_e = \frac{\lambda^2}{4\pi} G_{Rx}\ \left[\mathrm{m^2}\right]$ of the receiving antenna. The difference between the input power of the transmitting antenna and the received power in the load of the receiving antenna is related by the propagation gain (PG) and is given by

$$PG = \frac{P_{Rx}}{P_{Tx}} = \left(\frac{\lambda}{4\pi r}\right)^2 G_{Tx}(f) \cdot G_{Rx}(f) \tag{4.1}$$

The $\left(\frac{\lambda}{4\pi r}\right)^2$ factor is sometimes called the free space propagation gain coefficient. This can be misleading since, knowing that $\lambda = c/f$, one could conclude that somehow free space attenuates the signal with increasing frequency. This, of course, is not the case. The frequency dependence enters the equation because of the definition of antenna effective area A_e.

It must be noted that equation 4.1 assumes two reflection and polarization-matched antennas aligned for maximum directional radiation and reception. Equation 4.1 also is not directly applicable to UWB systems since it describes the propagation gain at a single frequency. To elaborate this further into an UWB propagation gain, the bandwidth must be added to the model.

The UWB path loss based on the geometric average can be evaluated by using the function

$$H\left(f\right)=\frac{c}{4\pi fr} \tag{4.2}$$

and an ideal filter

$$H_{filter}\left(f\right)=\begin{cases}1 & f_L\leq f\leq f_H\\ 0 & elsewhere\end{cases} \tag{4.3}$$

The path loss (PL) in a specific frequency band can be found with

$$PL=-10\log_{10}\left(\frac{\int_{f_l}^{f_h}\left|H\left(f\right)\right|^2 G_{Tx}(f)\cdot G_{Rx}(f)\left|H_{filter}\left(f\right)\right|^2(f)df}{\int_{f_l}^{f_h}\left|H_{filter}\left(f\right)\right|^2 df}\right) \tag{4.4}$$

or written in closed form as

$$PL=-20\log_{10}\left(\frac{c}{4\pi r\sqrt{f_L f_H}}\right)-10\log_{10}\left(G_{Tx}(f_L,f_H)\cdot G_{Rx}(f_L,f_H)\right) \tag{4.5}$$

The $\sqrt{f_L f_H}$ term is often called the pulse geometric central frequency. Setting $f_L =$ 500 MHz, $f_H = 1$GHz and $r = 5$ m, the path loss equals 43.4 dB.

The UWB transmitting antenna gain is determined using CST Microwave and Matlab and equals approximately -15 dBi. This is the expected attenuation when the implant is located beneath 3 layers of tissue consisting of 25 mm of muscle, 15 mm of fat and 1.5 mm of skin. For the receiving antenna we assumed a constant gain of 2 dBi across the entire frequency band, which is the typical gain of an UWB dipole antenna.

4.3.4. Variables in the Link Budget

Equation 4.5 predicts the UWB free space path loss. Strictly, it is only valid for a transmitter and a receiver far away from each other in an infinite empty space. The assumption of far field is valid here considering the distance and frequencies used in this work. However, since the transmitter and receiver are located inside a building or room, we cannot assume free space. The path loss between the implant and the base station will vary with the patient and with it surroundings. A more realistic indoor path loss model is given by

$$PL_{Indoor}=PL_{1m}+10\cdot n\cdot\log_{10}(r) \tag{4.6}$$

where PL_{1m} is the free space path loss at 1 meter in dB and n is the path loss exponent that characterizes how rapidly the path loss increases with distance. The path loss exponent n has experimentally been determined in [55] and typically lies between 2 and 4, depending on the environment. The path loss exponent of an RF system located in an office operating at 914 MHz was found to be around $n = 3.5$. Using this to calculate the expected indoor path loss at 5 meter results in $PL_{Indoor,5\,m} = 53.7\,dB$. This is 10.5 dB higher than the free space loss at 5 meter. We can also extend this range to 10 meters, which will increase the path loss with an additional 10 dB according to equation 4.6. Hence, the indoor path loss at 10 meter equals $PL_{Indoor,10\,m} = 63.7\,dB$.

In [6] the additional path loss relative to free space path loss was simulated and measured using a realistic model of a hospital room. The additional path loss found in this work was 10 dB, which is in line with the estimation above. Also, the variation in path loss due to the patient arm movement, age, sex and orientation were investigated. An extra margin of 10 dB should be include in the link budget to account for these effect. Although this simulation was at a single frequency (402 MHz), it gives a good indication of the expected extra losses. With this knowledge, the total additional path loss in the link budget is set to 20 dB.

4.3.5. Receiver Architecture

At the time of writing this thesis, no receiver architecture nor modulation scheme has been selected. Some assumptions have to be made to complete the link budget analysis. The effect of in-band interference is expected to be a dominant factor for the wireless link performance and has to be taken into account when choosing the receiver architecture.

The numerical results in [49] show that On-Off Keying (OOK) with a non-coherent receiver is the most energy efficient for short transmission distances (<5m). OOK considers a received pulse as logic '1' and no reception as logic '0' in a defined time window. This is a very energy efficient way of communicating, although the efficiency depends on the data to be transmitted. Disadvantage is that the system is not very robust when no reception is considered as a logic '0'. The robustness can be improved by addressing more pulses to one bit at the expense of reduced throughput.

Auto-correlation and energy detection receivers are both non-coherent UWB architectures which do not require channel estimation. Unlike straightforward energy detection circuits, auto-correlation receivers allow to detect UWB pulses below the noise floor. Disadvantage is that the delay used in auto-correlation receivers has to be accurately known. This introduces some design challenges when implementing the delay in an integrated circuit.

We will assume an energy detection receiver with OOK in further calculations. However, it is realized that other, more sophisticated receiver architectures might be a better solution for this particular application. More work has to be done on this topic.

Bit Error Rate

The Bit Error Rate (BER) gives insight to the receiver performance and is related to the energy per bit to noise power spectral density ratio E_b/N_0. For a non-coherent receiver with OOK, the probability of a low bit being received as a high bit is given by [53]

$$P_{eM} = 1 - Q\left(\sqrt{2E_b/N_0}, \sqrt{2 + E_b/2N_0}\right) \tag{4.7}$$

where Q(·) is the Marcum-Q function. The probability of a high bit being received as a low bit equals [53]

$$P_{eS} = \exp\left(-1 - E_b/4N_0\right) \tag{4.8}$$

The theoretical BER of OOK in combination with a non-coherent receiver can be calculated with [53]

$$P_e = \frac{1}{2}\left(P_{eS} + P_{eM}\right) \tag{4.9}$$

Figure 4.2 shows the BER versus the bit energy-to-noise power spectral density ratio E_b/N_0. From this analysis, an E_b/N_0 of 13.5 dB is required to obtain a BER of 10^{-3}.

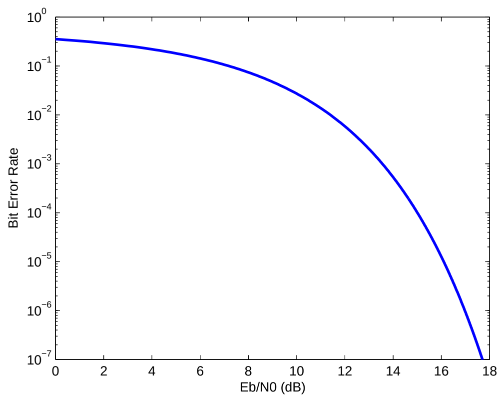

Figure 4.2.: Bit error rate vs. bit energy-to-noise power spectral density E_b/N_0 for OOK non-coherent receiver.

The analysis above is based on narrow band communication. The BER performance for UWB systems will be different because UWB occupies a larger bandwidth. This leads to a higher noise floor and also has a higher probability of in-band interference. However, the occupied bandwidth in this design in rather small compared to other UWB systems. Hence, the required E_b/N_0 will be higher than the calculated 13.5 dB, but less than UWB systems having several GHz of bandwidth.

A detailed BER analysis for sub-GHz UWB biomedical communication will not be done in this work. Instead, we compare the BER performance of UWB systems to our design which will give some idea of the required E_b/N_0. In [54], a 500 MHz bandwidth non-coherent receiver shows to require an E_b/N_0 around 16 dB to obtain a BER of 10^{-3}. In [52] the required E_b/N_0 equals 17 dB for a system having almost the same receiver specifications as this design. Similar values where found in [50, 51].

Based on the BER vs E_b/N_0 performance mentioned above, we set the minimum E_b/N_0 to 17 dB.

4.4. Link Budget

Determining the pulse power is the last piece to the link budget puzzle. When we know the receiver sensitivity, we can calculate the required average *pulse* power. The average pulse power delivered to the antenna should be equal to or greater than

$$P_{Tx,pulse} = P_{sens} + L_{add} + PL - G_{Rx} - G_{Rx} \tag{4.10}$$

Here is L_{add} the additional losses and PL the UWB path loss. The receiver sensitivity P_{Sens} is the required signal strength at the input of the receiver to produce an output signal with a specified BER. This can be calculated with

$$P_{Sens} = P_n + E_b/N_0 + IL \tag{4.11}$$

where P_n is the total average noise power per bit give by $P_n = N_0 + 10\log_{10}(R_b) + \mathrm{NF}$. For this receiver we assumed a Noise Figure (NF) of 5 dB and 3 dB Implementation Loss (IL). Substituting all parameters into Equation 4.10 results in an average pulse power of $P_{Tx,pulse}$ =-12.6 dBm = 54.95 μW contained in a -10 dB 500 MHz bandwidth. The complete link budget is given in Table 4.1.

It is realized that aspects such as narrowband interference and processing gain are neglected in this analysis. However, we included some safety margins and added additional losses to important link budget variables. It is therefore expected that the proposed system can provide a reliable communication link.

Table 4.1.: Link Budget

Term	*Data*	*Unit*	*Comment*
System parameters			
R_b	1	Mb/s	Bit rate
T_{Pulse}	6	ns	Pulse width
DC	0.6	%	Duty cycle ($DC = T_{Pulse}R_b$)
f_{BW}	500	MHz	-10 dB Bandwidth
Transmitter calculations			
$P_{Tx,pulse}$	-12.6	dBm	Tx average pulse power
G_{Tx}	-15	dBi	Tx antenna gain
$f_c^{'}$	707	MHz	Geometric central frequency $\left(f_c^{'} = \sqrt{f_L f_H}\right)$
PL	43.4	dB	Free space path loss at 5 m $\left(PL = -20\log_{10}\left(c/4\pi r f_c^{'}\right)\right)$
L_{Add}	20	dB	Additional losses (indoor path loss, patient movement, alignment)
Receiver calculations			
G_{Rx}	2	dBi	Rx antenna gain
P_{Rx}	-89	dBm	Rx power$\left(P_{Rx} = P_{Tx,pulse} - PL_{FS} - L_{Add} + G_{Tx} + G_{Rx}\right)$
N_0	-174	dBm/Hz	Noise power spectral density (kT, $with\, T = 310\, K$)
N_b	-114	dBm	Noise power per bit ($N_b = N_0 + 10\log_{10}(R_b)$)
NF	5	dB	Rx noise figure
P_n	-109	dBm	Total average noise power per bit ($P_n = N_b + NF$)
E_b/N_0	17	dB	Minimum energy per bit to noise PSD ratio to reach BER=10^{-3}
IL	3	dB	Receiver implementation loss
P_{Sens}	-89	dBm	Receiver sensitivity ($P_{Sens} = P_n + E_b/N_0 + IL$)

4.5. Pulse Shape

Since the radiation resistance is known, we can determine the pulse amplitude using Matlab. Using a Gaussian pulse train allows us to calculate the peak current. The pulse train has a Pulse Repetition Frequency (PRF) of 1 MHz, f_{center}=750 MHz, f_H=1 GHz, f_L=500 MHz. The fractional bandwidth $f_{frac,BW}$ equals 0.66 and is calculated using

$$f_{frac,BW} = 2\frac{f_H - f_L}{f_H + f_L} \tag{4.12}$$

This pulse complies with the FCC definition of an UWB signal since the fractional bandwidth is greater than 0.2. The required peak amplitude can be determined in Matlab by using

$$P_{Tx} = \frac{1}{T}\int\limits_{t}^{t+1/PRF} i_{pulse}^2 R_{rad} dt \tag{4.13}$$

If $T = T_{pulse}$, the calculated power equals the average pulse power $P_{Tx,pulse}$ supplied to the antenna. The link budget calculations are based on this power. The pulse width

T_{Pulse} is defined as the time laps where the pulse is larger than 1% of the peak value, in this case $T_{Pulse} \approx 6$ ns. In the case that $T = 1/PRF$, the calculated power corresponds to the power averaged over one pulse repetition period. This power can be used to calculate if the maximum allowed Equivalent Isotropic Radiated Power (EIRP) of the FCC regulations is met. For simplicity, we will assume R_{rad} to be constant. We will check if this a good assumption later.

To obtain an average pulse power of 54.95 μW, the peak pulse current was found to be 5.5 mA. This is considered acceptable since new types of lithium batteries such as lithium carbon monofluoride (CFx) batteries offer a high energy density and can be pulsed at currents above 20 mA without a significant voltage drop. [28]. Note that the average current drawn from the battery is considerably less because the duty cycle is only 0.6% (DC=T_{Pulse}PRF), ensuring ultra-low power consumption. The pulse with the given properties above is shown in Figure 4.3a and 4.3b.

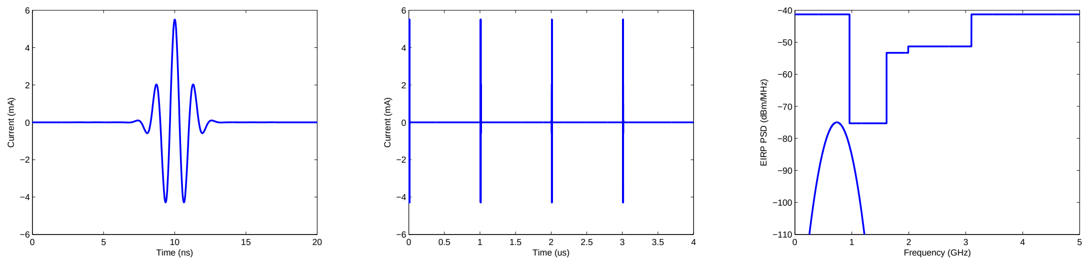

(a) Gaussian antenna driving current.

(b) Pulse train, PRF=1 MHz.

(c) PSD and FCC mask.

Figure 4.3.: Input current pulse train with corresponding PSD.

The corresponding Power Spectral Density (PSD) in W/Hz can be calculated with

$$PSD\,(f) = PRF\,|I(f)|^2\,R_{Rad} \tag{4.14}$$

where $I(f)$ is the Fourier transform of the pulse current waveform. The EIRP Spectral Density in dBm/MHz is given by

$$PSD\,(f) = 10\log\left(PSD(f)\right) + 10\log\left(G_a\right) + 90 \tag{4.15}$$

The 90 dB is added to convert from dBW/Hz to dBm/MHz. The calculated EIRP Spectral Density is shown in Figure 4.3c. There is some headroom left with respect to the FCC mask which allows for higher pulse power or higher bit rates.

However, in this analysis it is assumed that the gain and radiation resistance are constant. In other words, it is assumed that an ideal antenna (in terms of a flat frequency response) radiates an exact replica of the input signal, only attenuated by a constant factor. To see if this is a good assumption we simulate the radiated electric field located at 5 meter distance using CST Microwave Studio. Calculating the PSD from the E-field results in the actual EIRP Spectral Density, which *does* take the antenna into account.

The implanted antenna is driven with the same current Gaussian pulse as used in the previous analysis.

Figure 4.4a shows the electric field at 5 meter distance from the implanted antenna. Although it shows some small distortion, the original Gaussian shape is clearly present. In Figure 4.4b the two normalized calculated PSDs are shown. The solid blue line

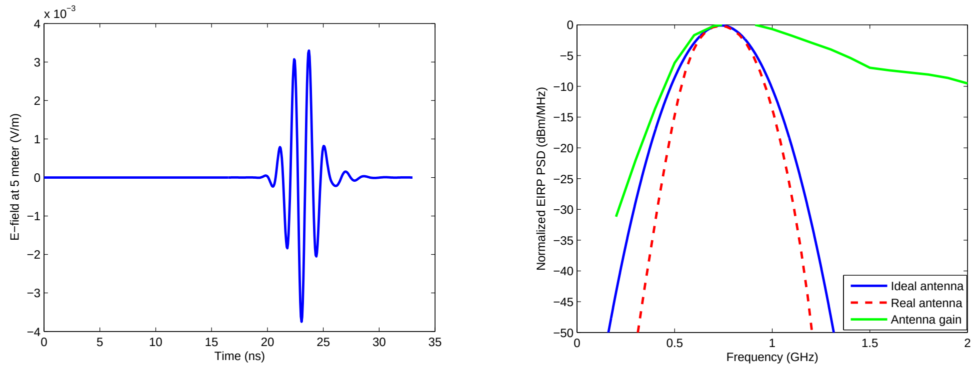

(a) Simulated E-field at 5 meter.

(b) Ideal and real antenna pulse transfer

Figure 4.4.: Comparison between ideal and real antenna EIRP Spectral Density.

represents the EIRP of a Gaussian pulse radiated from the 'ideal' antenna. The dotted line represents the real EIRP calculated from the E-field pulse at 5 meters. Notice that the bandwidth of the dotted EIRP is smaller because of the influence of the antenna. The antenna gain, indicated by the green line, attenuates more at the lower frequency side of the main lobe compared to higher frequencies. The difference in power can be found by integrating both PSD areas and compare them. It was found that the power of the actual EIRP was only 0.586 dB lower than the analysis with a constant gain.

This tells us two things. First, the information (pulse shape) is almost not affected by the antenna reactance as expected. This suggests that reliable data transfer is possible even with considerable variations in the antenna reactance. Secondly, assuming the antenna gain and resistance to be constant is a good approximation.

4.6. Human Exposure to RF Electromagnetic Energy

Knowing the pulse properties, antenna characteristics and PRF allows us to investigate if this system meets the limits of electromagnetic energy absorption by the body. There are two main criteria which has to be satisfied:

Peak electric field strength criterion For a pulsed EM field, the peak value of the instantaneous electric field strength in the frequency range of 0.1 to 300 000 MHz shall not exceed 100 kV/m [22].

Energy density criterion For short pulses ($< 30\ \mu$s), biological effects are dependent on the energy per pulse and correspond to a specific absorption per pulse. The spatial peak specific energy absorption (SA) for the general public applicable to pulsed exposure in the head between 0.3–6 GHz within any 50 μs interval is limited to 2 mJ per kg [22].

We can check this by simulating the electric field strength and SAR using CST Microwave Studio. It was found that the peak intantaneous electric field strength, located close to the antenna origin, is 7.3 V/m. So the electric field strength criterion is met with ease.

The *local* specific energy absorption can be calculated with the electric field:.

$$SA = \int_{t}^{t+T} \frac{\sigma E(t)^2}{\rho} dt \tag{4.16}$$

We used an electric conductivity σ of 0.75 [S/m] and a muscle mass density of ρ=1040 $\left[\text{kg/m}^3\right]$. With the simulated electric field pulse, we calculated the local SA to be 43.52 pJ/kg. Calculating the total SA within the 50 μs interval we have to multiply this with 50, given a PRF of 1 MHz. However, it is clear that the energy density criterion is also met easily.

The local maximum specific absorption ratio can be calculated with $SAR = SA/T_{Pulse}$ and in this case equals 7 mW/kg, given that the pulse width is 6 ns. This is also simulated in CST Microwave Studio and shown in Figure 4.5. This visually shows that the peak

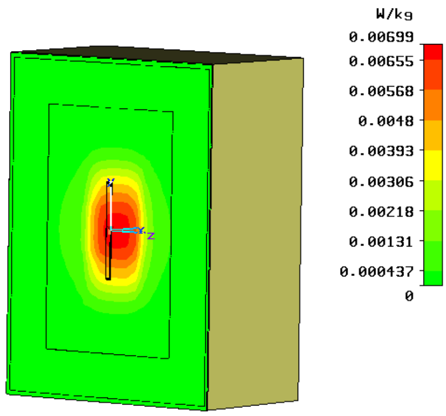

Figure 4.5.: Maximum SAR (10g average).

local power is absorbed close to the antenna. This simulation is based on the averaged SAR over a 10g cubic mass. In comparison, the maximum local SAR for *continuous* wave exposure equals 2 W/kg for the general public. The maximum local SAR for *pulsed* EM wave exposure equals 2000 W/kg. The total simulated SAR over the total tissue (or whole body SAR) equals only 0.18 mW/kg. Note that we simulated the antenna in a cube consisting of several tissue layers with a volume of only 104x116x84.5 mm^3. Hence, the whole-body SAR will even be lower for a real person.

In conclusion, the energy absorption by the tissue is well within the limits. The radiated pulse power in this design is too low and the exposure duration to short too cause any significant tissue heating which may result in adverse biological effects.

4.7. Summary

All required system design specifications for a realistic link budget where derived in this chapter. An current pulse with a peak value of 5.5 mA and pulse width of 6ns was found as antenna driving signal. The corresponding -10 dB bandwidth extends from 0.5 to 1 GHz. We aim for a bit rate in the order of 1 Mb/s. This will keep the average power consumption and emission level low, which relaxes the constrains to meet the FCC mask. Higher bit rates can be achieved, but depend on the body losses and FCC mask. For the receiver architecture we assumed a non-coherent energy detecting scheme with OOK modulation since this is the most energy efficient for distances shorter than 5 meter. However, it is realized that other, more sophisticated receiver architectures might be a better solution for this particular application.

EIRP Spectral Density calculations based on the electric field simulations showed that the antenna almost does not affect the pulse shape, although the radiated pulse bandwidth will be slightly less than the antenna driving pulse. Still, reliable data transfer is possible even with considerable variations in the antenna reactance.

Finally, it was shown that the RF electromagnetic energy aborption is well within regulation limits. The radiated pulse power in this design is too low and the exposure duration to short to cause any significant tissue heating.

5. Circuit Design

In this chapter the circuit design of a sub-GHz UWB transmitter is treated. General design aspects such as choice of technology, process variations, temperature range and power supply are discussed in the first section. Consequently, the system design specifications found in the previous chapter are used to choose the pulse generator topology. After this follows the pulse generator circuit implementation, where process variations are taken into account to design a reliable and realistic UWB transmitter. Finally, the output stage topology and circuit design will be discussed.

5.1. General Circuit Design Considerations

Choice of technology

The choice of IC technology used for this design is based on the previous work done in the Biomedical Electronics Group of Delft University. Since this design will be part of a larger fully implantable system, it has to be integrated in one chip using the same technology. The technology used for this project is AMIS I3T25 0.35 μm.

The reason why this technology was chosen in our group is related to the requirements of other subsystems. For example, the neural stimulator requires high voltage transistors because during neurostimulation the voltage can be as high as 15V. Standard technologies, especially with small sizes, cannot handle these high voltages. I3T25 provides both low and high voltage transistors and is suitable for analog and digital design. Another important aspect is that the minimum gate length is 1.7 times smaller compared to other technologies which where considered at the time. This can save valuable chip area and allows to work at higher frequencies. Other trade-offs such as power consumption (switching and static leakage current), temperature dependence and available documentation were made between different technologies and lead to the use the AMIS I3T25 0.35 μm technology. We will not go in more detail on the choice of technology since the choice was already made before this work.

I3T25 Process information

The CMOS process within the 0.35 μm AMIS I3T25 technology is a single level poly, twin-tub CMOS process using an n-type epitaxial layer on top of a p-type substrate [56]. It is developed for the design of circuits operating at a supply voltage of 3.3 volt, but also offers high voltage transistors which extend to a voltage range of 18V.

Furthermore it has the following analog capabilities:

- Medium voltage transistors
- Precision highly linear metal/metal capacitors
- Precision high Ohmic polysilicon resistors
- (Floating) medium voltage NDMOS
- Low voltage PNP bipolar transistors
- Low voltage NPN bipolar transistors

Process variations

In order to verify the robustness of an integrated circuit design, the circuit has to be simulated over worst case process corner and device mismatch. This will give a good indication how reliable the circuit will be over the extreme parameter variations that can occur during the fabrication process.

Temperature range

The human body has an excellent internal temperature 'regulator' which tries to keep the body temperature close to 37 °C. The temperature of the human body therefore rarely changes drastically. Still, we will consider a temperature range between 30 and 45 °C in this design.

Power supply

In this design it is assumed that a power management system is in between the battery and the circuit, providing a stable power supply. It is also assumed that the supply can deliver the required energy of each pulse within the pulse width.

There are no specification given for the supply voltage, this will follow during the circuit design.

5.2. Pulse Generator Topology

In this section we will discuss various pulse generator topologies and their advantages and disadvantages.

Pulse generator based on filter

A filter based pulse generator which is driven by an impulse will generate a pulse that depends on the transfer function of the filter. The authors in [59] used an 8th order Daubechies scaling function state-space filter to generate an UWB pulse. Each element in the state-space description of the orthonormal ladder filter is implemented using gm cells and capacitors. Although a large variety of pulse shapes can be designed, it consumes too much power (> mW) and occupies a large chip area.
Others use an LC ladder filter topology [60], however, the AMIS I3T25 technology does not provide inductors. But even if it did, it is likely that it will occupy too much area.
Another approach is to generate a rectangular or quasi-Gaussian pulse which is shaped by the antenna [58]. Advantage is that low power consumption can be achieved (235 μW with PRF=100 MHz). However, this solution is not applicable to this design due to the non-predictable properties of the antenna.

Pulse generator based on combination method

An all-digital approach to generate pulses is presented in [61]. The pulses are generated in 4 different phases by means of NAND, NOR and delay blocks. In the output stage, the four triangular pulses are combined to form the output pulse. Disadvantage is that an accurate delay block is required for a robust pulse generator, as any variation in the delay blocks will change the pulse shape.

Pulse Generator based on oscillator

Pulse generating by means of an oscillator can be achieved by turning the oscillator ON for a certain time duration and turn it and OFF again. Doing so generates a pulse which occupies a bandwidth dependent on the time duration. The energy consumed per pulse can be very low, in the order of a few pJ [62]. This is a low-complexity, low area and energy efficient solution. Disadvantage is that the pulse shape is difficult to design orthogonally since any change in pulse shape will change the pulse center frequency, amplitude and bandwidth.

Choice of topology

The choice of pulse generator topology is based on the design philosophy described in previous chapter; low area, low complexity, robust and only consuming power when a pulse is being generated. Although a filter based pulse generator can generate a larger variety of pulse shapes, it also requires a complicated filtering circuit and therefore is not area efficient. An oscillator based pulse generator can be build with only a hand full of components and can be very energy efficient. Because this topology is in line with the design philosophy, it is decided that an oscillator based pulse generator will be used for this design.

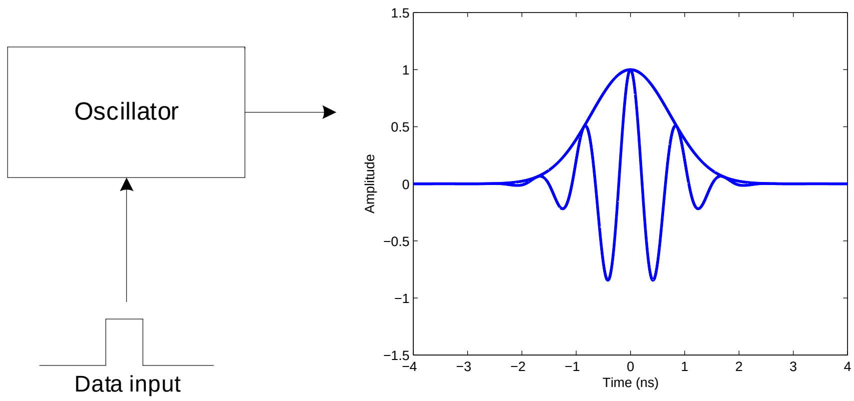

Figure 5.1.: Oscillator based pulse generator principle.

5.3. Pulse Generator Circuit Analysis

The main principle of an oscillator based pulse generator is explained with the aid of Figure 5.1. By switching the oscillator on with the data input, the amplitude will start to increase during start-up. By switching the oscillator off before the steady state is reached the pulse amplitude decays again, resulting in a typical UWB pulse. The LC tank based oscillator is by far the most used circuit implementation to realize this type of pulse generator [62, 63]. And for good reason, because it can offer a large output voltage swing, is easy tunable in frequency and only uses a single tail current source. Most of these pulse generators are designed to generate pulses which occupy a bandwidth in the commercial 3-5 GHz band.

However, the LC oscillator has a major drawback which makes it unsuitable for sub-GHz biomedical applications. Chip area is extremely limited for biomedical implants, especially when this circuit has to be integrated with the other subsystems. Inductors will occupy a lot of chip area. Moreover, integrated inductors usually have a poor Q-factor at low frequencies. And as already mentioned, the I3T25 technology does not provide inductors. So we have to look for alternatives.

Relaxation Oscillator

The authors in [64] proposed a pulse generator based on a relaxation oscillator. It is designed to oscillate at 5 GHz and with an input pulse of 0.6 ns it produces an UWB pulse with 4-GHz bandwidth. Digital modulation can be performed directly on the pulse generator circuit without additional circuitry. The available bipolar transistors in this technology are restricted to a specific application. The typical current gain factor is low, around 20, which makes it difficult to obtain high loopgain at high frequencies. Moreover, the area of a minimum voltage npn transistor is 25 μm^2, which is a factor 142 larger than the minimum size MOS transistor. Although this pulse generator was build with bipolar transistors, it can also be implemented with MOS transistors. We therefore will investigate the MOS oscillator based pulse generator in more depth.

Relaxation oscillators (also called source-coupled multivibrators) are used very frequently in systems requiring voltage-controlled oscillators (VCOs) because of their ability to provide high frequency, symmetrical output waveforms and stable performance over temperature and process variations. Although they have worse phase noise performance compared to LC oscillators, this does not result in a decrease of performance in this design because we are dealing with wideband pulses. However, the LC oscillator has the advantage that it provides much smaller harmonics compared to relaxation oscillators. Lower harmonics improve the spectral efficiency of the pulse since more energy is focused in the desired operating frequency band.

When looking at the circuit depicted in Figure 5.2 , it may not be obvious at first

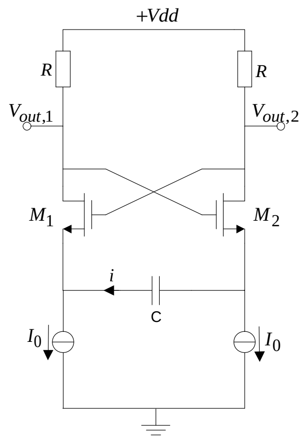

Figure 5.2.: Source-coupled multivibrator.

sight, but nearly sinusoidal oscillations can be realized using this multivibrator. The oscillator makes a smooth transition between the relaxation regime and the sinusoidal regime when decreasing the capacitance value C. When this multivibrators is forced to operate at its maximal frequencies, the output signal strongly resembles a sinusoidal waveform.

An interesting fact is that another configuration of the multivibrator can move in the opposite way, making the transition from the sinusoidal regime at low frequencies to the relaxation regime at high frequencies. More details on this subject can be found in [66, 68, 67].

We will show that the inductor-less circuit shown in Figure 5.2 can operate like an LC oscillator when the components are given appropriate values.

5.3.1. Circuit Analysis

To analyze how the circuit in Figure 5.2 can generate nearly sinusoidal oscillations, we use its small signal equivalent circuit shown in Figure 5.3. From this we will calculate the start-up condition, oscillating frequency and amplitude.

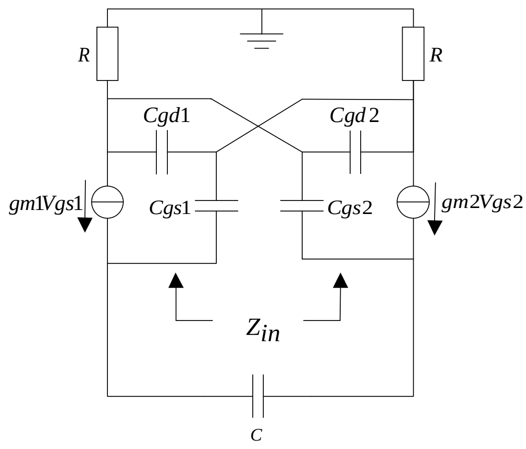

Figure 5.3.: Source-coupled multivibrator and its simplified small signal circuit.

Determining start-up condition

Assuming a symmetric circuit, ($C_{gs1} = C_{gs2} = C_{gs}$, $C_{gd1} = C_{gd2} = C_{gd}$, $g_{m1} = g_{m2} = g_m$) one can find that for the circuit depicted in Figure 5.3 the input impedance seen from the capacitor is given by [69]

$$Z_{in}(s) = 2\frac{\left(g_m^{-1} - R\right) + sRg_m^{-1}\left(C_{gs} + 4C_{gd}\right)}{\left(1 + s\frac{C_{gs}}{g_m}\right)\left(1 + s4RC_{gd}\right)} \tag{5.1}$$

We can obtain the characteristic equation by calculating the roots of

$$Z_{in}(s)\, sC + 1 = 0 \tag{5.2}$$

which can be rewritten as

$$s^2\left[\frac{2RC}{g_m}\left(C_{gs} + 4C_{gd} + \frac{2C_{gd}C_{gs}}{C}\right)\right] + s\left[2C\left(\frac{1}{g_m} - R\right) + 4RC_{gd} + \frac{C_{gs}}{g_m}\right] + 1 = 0 \tag{5.3}$$

To obtain sinusoidal oscillations, the solution for s must be purely imaginary. In other words, the two poles must be a complex-conjugated pair which lie on the imaginary axis. This condition is obtained when the coefficient of the second term in Equation 5.3 is equal to zero. It directly follows that

$$g_m = \frac{1}{R}\left(\frac{1 + \frac{C_{gs}}{2C}}{1 - \frac{2C_{gd}}{C}}\right) \tag{5.4}$$

For start-up condition it must be guaranteed that at least one pole lies in the positive halfplane so that oscillation can take place. This must be valid over *all* process variations. A safety margin should thus be included to place the poles far enough in the positive halfplane such that oscillation will always occur. Hence, the start-up condition is given by

$$\boxed{g_m > \frac{1}{R}\left(\frac{1+\frac{C_{gs}}{2C}}{1-\frac{2C_{gd}}{C}}\right)} \tag{5.5}$$

This means that truly sinusoidal oscillation will never be achieved in practice because the poles are not purely imaginary. There is a trade-off to be made between a more robust design or a better approximation of a sinusoidal oscillation.

Determine oscillating frequency

If the coefficient of the second term in Equation 5.3 is zero, the complex-conjugate poles (in rad/sec) are equal to

$$s_{1,2} = \pm j\sqrt{\frac{g_m}{2RC\left(C_{gs} + 4C_{gd} + \frac{2C_{gd}C_{gs}}{C}\right)}} \tag{5.6}$$

The frequency (in Hz) is given by

$$\boxed{f = \frac{1}{2\pi}\sqrt{\frac{g_m}{2RC\left(C_{gs} + 4C_{gd} + \frac{2C_{gd}C_{gs}}{C}\right)}}} \tag{5.7}$$

Determine amplitude

To calculate the large signal steady state voltage amplitude between the two drains in Figure 5.2 we must consider that $g_{m1} \neq g_{m2}$. Instead we write that $g_{m1} = g_{m0}\sqrt{1 - \frac{i}{I_0}}$ and $g_{m2} = g_{m0}\sqrt{1 + \frac{i}{I_0}}$. The steady state current i can be calculated using the van der Pol equation. An approximation of i can be written as [68].

$$i \approx I_0\sqrt{8\left(1 - \frac{1}{Rg_{m0}}\right)} \tag{5.8}$$

The differential peak-to-peak voltage between drains equals $v_{diff} = 2Ri$, hence

$$\boxed{v_{diff} \approx \sqrt{32}RI_0\sqrt{1 - \frac{1}{Rg_{m0}}}} \tag{5.9}$$

Note that this is only valid when the start-up condition is met.

5.3.2. Influence of process variations

The circuit discussed in previous section is implemented using resistors. Resistor values in this technology can have a large spread over process variation (±25%) [57]. It can be seen in Equations 5.5 and 5.9 that any variation in R will have a large influence on the start-up condition and output voltage because of its 1:1 relationship. Increase in R will result in a $\sqrt{R}$ decrease in oscillating frequency. We therefore need to minimize the variation over process corners to obtain a robust design.

The 5 different MOS corners for the I3T25 technology are given in Table 5.1. Awcs denotes worst case speed and awcp denotes worst case power. Awc1 and awc0 are the combination of the two. The effect on the transistor parameters for worst case speed and power are also given in this table.

Table 5.1.: Process corners

Corner type	6σ corner
Typical	typ
Weak N, Weak P	awcs
Strong N, Strong P	awcp
Strong N, Weak P	awc1
Weak N, Strong P	swc0

	Worst case speed	Worst case power
Transconductance	Minimum	Maximum
Threshold voltage	Maximum	Minimum
On resistance	Maximum	Minimum
Capacitance	Maximum	Minimum
Switching times	Maximum	Minimum

There are a lot of resistor and transistor process corner combinations possible which have a large impact on the circuit performance. We will discuss how robust this implementation is and if it can be improved when the resistors are implemented using MOS transistors.

Start-up condition

Some resistor and transistor corner combinations result in a non-oscillating circuit. For example, a low speed corner in combination with a minimum resistor will lower the transistor gm and decrease the resistor value. At some combination the start-up condition will not be met and oscillation will not start.

The resistor load can also be implemented using a MOS transistor with its gate and drain shorted (diode-connected transistor). This simple resistor implementation can provide a reasonable linear voltage-current relationship, even for large signal swings [73]. This has been confirmed using Cadence RF Spectre simulations.

When the resistor is implemented with a diode-connected transistor as shown in Figure 5.4, we can approximate R with $1/g_{mR}$. The start-up condition can then be written as

$$g_{m0} > g_{mR}\left(\frac{1+\frac{C_{gs}}{2C}}{1-\frac{2C_{gd}}{C}}\right) \tag{5.10}$$

A process corner with weak N means that *all* NMOS transistor undergo to same relative reduction in speed. If the resistor and cross-coupled gm cell are both implemented

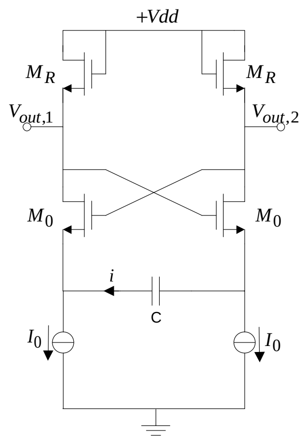

Figure 5.4.: MOS relaxation oscillator.

with the same transistor type (NMOS in this case), then the gm value of both transistor will undergo the same amount of variation over process corners. This means that the *ratio* of g_{m0}/g_{mR} remains intact and the start-up condition will almost not be affected. There will be a small variation in start-up condition because the transistor capacitances will also change over corners. However, when looking at the start-up condition it shows that this effect can be minimized by choosing a capacitor C such that $C \gg C_{gs}$ and $C \gg C_{gd}$.

Amplitude

When using a diode-connected transistor we can write for the differential output voltage that $v_{diff} \approx \frac{\sqrt{32}I_0}{g_{mR}}\sqrt{1-\frac{g_{mR}}{g_{m0}}}$. Since the current through the diode-connected transistor and the cross-coupled pair transistor is the same, we can relate I_0 to g_m by writing $g_m = \sqrt{2KI_0\left(W/L\right)}$, where $K = \mu_{eff}C_{ox}$[1]. The peak-to-peak differential output voltage in terms of bias current and transistor size now becomes

$$v_{diff} \approx \sqrt{16I_0\frac{L_R}{KW_R}\left(1-\sqrt{\frac{W_RL_0}{W_0L_R}}\right)} \tag{5.11}$$

Looking at this expression, we conclude that any variation of parameter x will only result in $\sqrt{x}$ in output voltage. This is especially true when $W_0/L_0 > W_R/L_R$, which is required to start oscillations. However, some amplitude control might be required in the output stage to compensate for variations in oscillator amplitude, path loss and power absorption in the tissue.

[1] $\mu_{eff} = \frac{\mu_0}{1+\theta(Vgs-Vth)}$, where θ typically lies between $0.05 \leq \theta \leq 0.25$ $\left[V^{-1}\right]$, so $\mu_{eff} \approx \mu_0$ is a good approximation in most situations.

Frequency

The oscillating frequency in terms of bias current and transistor parameters is given by

$$f = \frac{1}{2\pi}\sqrt{\frac{2KI_0\sqrt{\frac{W_R W_0}{L_R L_0}}}{C\left(C_{gs} + 4C_{gd} + \frac{2C_{gd}C_{gs}}{C}\right)}} \tag{5.12}$$

If we consider the worst case speed process corner, K will become smaller and the transistor capacitances will become larger, causing the oscillating frequency to drop significantly. Exactly the opposite holds for the worst case power corner.

To compensate for this effect, a suitable parameter in Equation 5.12 has to be chosen to correct the frequency over process variations. The only two possible parameter that can be chosen are the bias current I_0 and the capacitor C. Most designers choose I_0 to correct the frequency [65, 64]. Doing so will also change the output voltage during tuning since its proportional dependence on I_0. But this can be resolved by using the replica biasing technique. However, the power consumption will still vary over process variations.

Since this is not an attractive solution, we choose to use capacitor C to adjust the frequency. The reasoning is as follows: Tuning capacitor C will not affect the power consumption in any way. Also the differential output voltage will not be affected by tuning C according to Equation 5.11. However, note that the amplitude calculations are an approximation. We will have to check this with simulations later. Tuning the capacitor *does* have a small effect on the start-up condition, but as mentioned before, this can be minimized by choosing a capacitor C such that $C \gg C_{gs}$ and $C \gg C_{gd}$.

Chip area

To compare occupied chip area of a passive resistor and diode-connected transistor, we look at the required dimensions to obtain a 1 kΩ resistance. The 'HIPOR' passive resistor requires a minimum area of 25 μm^2 to create a 1 kΩ resistance is. The resistance for the transistor implementation depends on the transistor parameters and bias current: $R = 1/\sqrt{2KI_0\,(W/L)}$. When assuming a bias current of 100 μA, the required chip area of the transistor is only 4.4 μm^2. This difference becomes even larger for higher values of R. The use of NMOS transistors also is an advantage for chip area because a PMOS transistor requires a 2.5 times larger W/L ratio to obtain the same gm as the NMOS transistor because the hole mobility is less than the electron mobility.

In conclusion we can say that the NMOS diode-connected transistor circuit implementation will be more robust over process variations compared to the circuit employing a passive resistor.

5.4. Pulse Generator Circuit design

In this section the equations derived in the previous section will be used to assign the circuit parameters their appropriate values. First, the desired operating conditions will be defined.

For the frequency, we aim the center frequency of the pulse to be 750 MHz. But if required, this frequency can be made higher or lower by changing capacitor C. The required output voltage depends on the input voltage capabilities of the next stage, as a too large input voltage can cause distortion within this stage. A peak-to-peak differential input voltage of 1V is within the voltage range of most transconductors without causing too much distortion [72]. We therefore will assume $v_{diff} = 1$ V during the following calculations. We will check if this assumption is correct later.

Robustness factor

The robustness of the circuit will be defined in the start-up condition by introducing a robustness factor θ to the equation such that $g_{m0} = g_{mR}\theta$, where

$$\theta > \left(\frac{1 + \frac{C_{gs}}{2C}}{1 - \frac{2C_{gd}}{C}} \right) \tag{5.13}$$

The robustness factor θ must be larger than one for all (process) variation. In order for θ to be almost independent on the capacitances we note that C must be larger than C_{gd} and C_{gs}. To have some idea of the influence of C_{gd} and C_{gs} to θ and the required tuning capacitor C, we must find the MOS capacitances.

In saturation region the gate-source capacitance can be approximated by [73]

$$C_{gs} \approx \frac{2}{3} \frac{\epsilon_0 \epsilon_r W L}{t_{ox}} \tag{5.14}$$

The typical gate oxide thickness (t_{ox}) in this technology is 7 nm [57]. Furthermore we have that $\epsilon_0 = 8.854 \cdot 10^{-12}$ F/m and $\epsilon_r = 3.9$. If we use the standard W/L ratio of 10/0.3 [μm/μm], we calculate the gate-source capacitor to be $C_{gs} \approx 11.5$ fF.

The gate-drain capacitance roughly equals $C_{gd} \approx WC_{ov}$, where C_{ov} is the overlap capacitance [73]. Using the circuit in Figure 5.5 we simulated the overlap capacitance to be C_{ov}= 2 fF (the body node is connected to the source, which is not drawn here).

In order to keep the influence of the MOS capacitances to θ limited to within 10%, C should be larger than 100 fF. Now that we can minimize the variation in θ, we can set the robustness factor θ to the desired value. To guarantee start-up condition over all process variation, we set the robustness factor θ to 1.3. We will use process variation simulations in the next chapter to check if this is good enough. If we assume that the current through all transistors in Figure 5.4 is the same and assuming that $K_o = K_R$, we can write θ in terms of transistor size only. The robustness factor θ can be set with

$$\boxed{\theta = \sqrt{\frac{W_0 L_R}{W_R L_0}}}$$

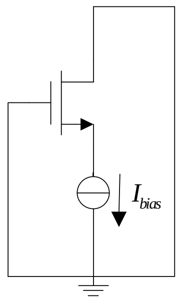

Figure 5.5.: Circuit used to extract small signal parameters.

Determine minimum current consumption

Since power consumption is one of the key design aspects for biomedical circuit design, we need an expression that relates the required bias current to the desired operating frequency, robustness factor and differential output voltage. First we use the expression $g_{m0} = g_{mR}\theta$ to include the robustness factor in the equation. For the output voltage we can write that $v_{diff} \approx \sqrt{16\frac{I_0 L_R}{K W_R}\left(1 - \frac{1}{\theta}\right)}$.[2]

Rewriting this equation to the bias current I_0 yields

$$I_0 \approx \frac{K W_R}{16 L_R \left(1 - \frac{1}{\theta}\right)} v_{diff}^2 \tag{5.15}$$

Recalling the oscillating frequency Equation 5.12, and knowing that $\theta = \sqrt{\frac{W_0 L_R}{W_R L_0}}$, we can write that

$$f = \frac{1}{2\pi}\sqrt{\frac{2 K I_0 \frac{W_R}{L_R}\theta}{2C\left(C_{gs} + 4C_{gd} + \frac{2C_{gd}C_{gs}}{C}\right)}} \tag{5.16}$$

If we calculate W_R/L_R using Equation 5.16 and substitute this in Equation 5.15, we obtain the bias current in terms of frequency, robustness factor and differential output voltage

$$\boxed{I_0 \approx \pi f v_{diff}\sqrt{\frac{C\left(C_{gs} + 4C_{gd} + \frac{2C_{gd}C_{gs}}{C}\right)}{8\left(\theta - 1\right)}}} \tag{5.17}$$

To have some idea of the order of magnitude for the required bias current we can use the results of previous section. If we require that $\theta = 1.3$, $v_{diff} = 1$ V, f=750 MHz and assume for M_R the standard W/L ratio of 10/0.35 ($C_{gs} = 11.5$ fF, $C_{gd} = 2$ fF, C=100 fF), it follows from Equation 5.17 that the minimum bias current of each current source should be equal to 68 μA.

[2] Note that for large values of θ, v_{diff} will go to its asymptotic value of $\sqrt{16\frac{I_0 L_R}{K W_R}}$.

Note that these equations assume ideal current sources. Also the diode-connected transistors will introduce a small capacitance to the circuit. Furthermore it assumes that the poles both lie on the imaginary axis. When θ is larger than 1, this is not entirely true since the poles move along the root locus to a lower frequency in the right halve plane. The required bias current is therefore expected to be higher than the predicted 68 μA. However, Equation 5.17 offers a strong insight on the circuit performance in terms of important design parameters and provides a good starting point.

Determine minimum supply voltage

If the ideal current sources in Figure 5.4 are implemented with transistors we can write

$$V_{DD} = V_{GS,R} + V_{GS,0} + V_{DS,I} \tag{5.18}$$

For transistors operating in strong inversion it holds that

$$V_{GS} = \sqrt{\frac{2I_0 L}{\mu_{eff} C_{ox} W}} + V_{TH} \tag{5.19}$$

and the drain-source voltage of the current source transistor is given by

$$V_{DS,Sat} = V_{GS} - V_{TH} = \sqrt{\frac{2I_0 L}{\mu_{eff} C_{ox} W}} \tag{5.20}$$

The minimum supply voltage therefore equals

$$\boxed{V_{DD,min} = \sqrt{\frac{2I_0 L_R}{\mu_{effR} C_{oxR} W_R}} + V_{TH,NR} + \sqrt{\frac{2I_0 L_0}{\mu_{eff0} C_{ox0} W_0}} + V_{TH,N0} + \sqrt{\frac{2I_0 L_I}{\mu_{effI} C_{oxI} W_I}}} \tag{5.21}$$

Using Table 5.2 we can calculate the required voltage supply (the datasheet uses the expression βlin=$\mu_{eff} C_{ox} \frac{W}{L}$).

Table 5.2.: Key electrical Parameters.

NMOS Device W/L	Parameter	Units	Low	Typical	High
0.5/0.35	$V_{TH,N}$	V	0.427	0.615	0.799
	βlin	uA/V^2	132	210	276
10/0.35	$V_{TH,N}$	V	0.466	0.593	0.709
	βlin	uA/V^2	3724	5066	5961

If we set L_R and L_0 to minimum length it follows that $W_0 = \theta W_R^2$. Thus, for $W_0 = 10\,\mu m$ it follows that $W_R = 4.5\,\mu$m. For the current source transistor we can set the ratio to a minimum of $W_I/L_I = 0.5/0.35$. Doing so will result in a typical minimum supply voltage of 2.5 V if we assume the minimum calculated bias current of 68 μA.

However, since we expect that the required bias current will be larger than 68 μA, the required minimum voltage supply will be even higher. Also note that the required supply voltage strongly depends on the threshold voltage $V_{TH,N}$ and also on βlin. Both can vary considerable over process corners as shown in Table 5.2. For the worst case speed corner the minimum required voltage supply increases to 2.8 V. The W_I/L_I ratio of the current source transistor can be increased to reduce the supply voltage.

These threshold voltages are valid under the condition that Vbs=0. The body and source are therefore connected together to eliminate the body effect and to keep the supply voltage low. This is possible since the I3T25 0.35 μm AMIS technology is a twin-well process. This has been confirmed by checking the layout properties in the documentation and by conducting Cadence Spectre simulations.

The calculation made so far will be checked by simulating the oscillator in Cadence. We found that the following dimensions result in the preferred oscillation performance: $W_R = 3\,\mu$m, $W_0 = 5\,\mu$m, $W_I = 5\,\mu$m, $L_0 = L_I = L_R = 0.35\,\mu$m, $C = 100\,$fF, $I_0 = 87\,\mu$A. The simulated differential output voltage is shown in Figure 5.6. With these dimensions the simulated frequency is f =747 MHz, the peak differential voltage equals v_{diff}=528 mV and the robustness factor θ is 1.4. The required supply voltage in the typical process corner was found to be $V_{DD} = 2.2\,V$. To include the worst case speed corner we must increase this to $V_{DD} = 2.5\,V$. These values are well in line with the predictions of Equation 5.21.

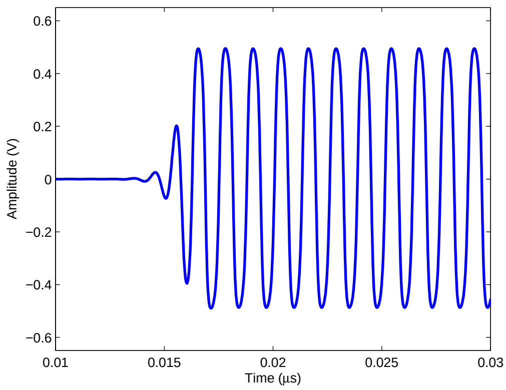

Figure 5.6.: Output voltage v_{diff} simulated in Cadence RF Spectre.

5.4.1. Pulse generating circuit implementation

Generating the UWB pulses is done by switching the current sources on and off. This principle is shown in Figure 5.7. For now, let's ignore transistor M8, M9, M10 and M11. Their function will be explained later. The data input, represented by digital signal D_1,

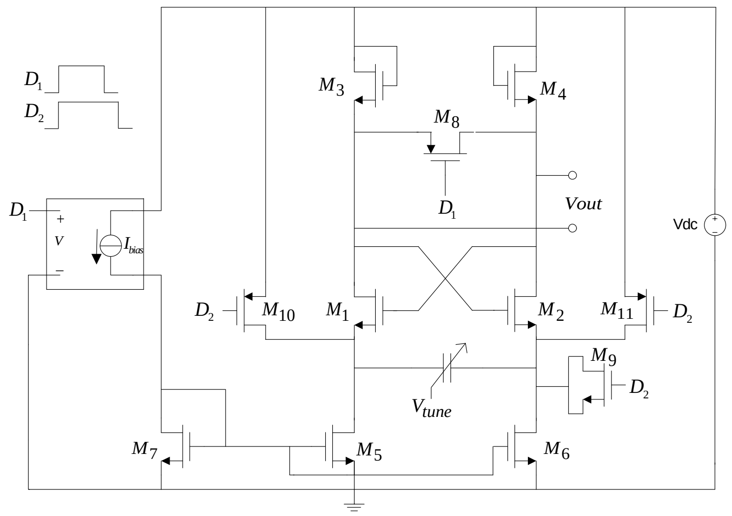

Figure 5.7.: MOS pulse generator principle.

is connected to a Voltage Controlled Current Source (VCCS). A bias current will flow through the current mirror and the oscillator when a logic '1' is presented to the VCCS. A logic '0' will switch off the oscillator. The pulse shape is determined by the rise and release time of the oscillator and the duration of the data input D_1.

Turn-off effects

In contrast to the LC pulse generator and the relaxation oscillator with passive load resistors, this circuit implementation with the diode-connected transistor cannot generate pulses without additional circuity. This can be understood when we consider what happens at the moment the oscillator is switched OFF after oscillation. At this moment the bias current through M3 and M4 drops to zero so that $1/g_m$ becomes very large. This will influence the pulse shape since the release time constant is now much larger than the rising time constant. This effect can be seen in Figure 5.8a.

This problem can be solved by introducing a component which decreases the release time when the oscillator is switched off. By adding transistor M8 between the two drains as shown in Figure 5.7 and drive it with the same digital input D_1 as the VCCS, the charge will be removed from the output nodes. The change in time constant can be influenced by the dimensions of M8. The improvement of the pulse shape can be seen in Figure 5.8b. With a digital input signal of 4 nsec this circuit produces a pulse with a -10 dB 500 MHz bandwidth.

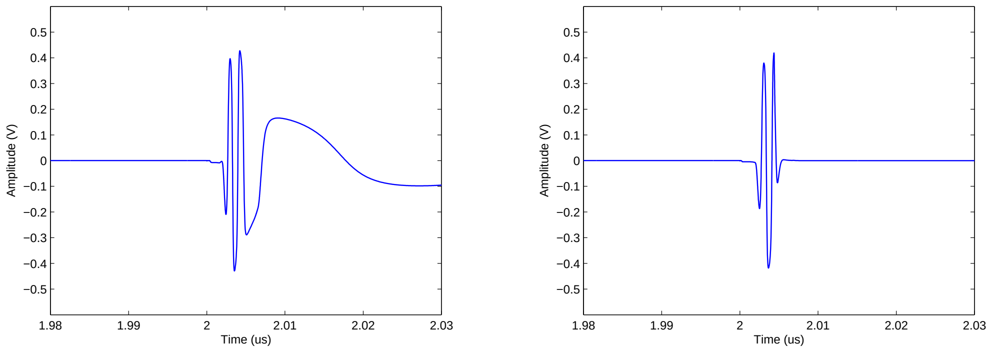

(a) Pulse without M8

(b) Pulse with M8

Figure 5.8.: Effect of M8 on pulse shape

Another problem arises when the oscillator is switched off since the drain voltage of M1, M2, M5 and M6 will not be well defined. They depend on the supply voltage and the leakage current of the transistors, which change over process variation. If there is any mismatch, an offset is observed at the differential output voltage. As a result, the pulse voltage will not be exactly zero after the oscillator is switched off. To solve this, these undefined voltage nodes are defined using two additional transistors M10 and M11 connected between the supply voltage and the source of M1 and M2. When the oscillator is switched off, M10 and M11 will fix these voltage nodes to the supply voltage. Since both outputs will be forced to the supply voltage, the differential output voltage is guaranteed to be zero after the pulse is generated. M10 and M11 are driven by binary signal D_2, which is slightly longer in time compared to D_1 so that the pulse shape is not affected by the switching action. The relation between D_1 and D_2 will be discussed later in this chapter.

5.4.2. Defining initial pulse condition

Looking at the MOS relaxation oscillator we note that the circuit is symmetrical. This means that the circuit is completely balanced and that theoretically oscillation will not start. For a practical oscillator, noise and device mismatch will cause the initial source voltage of M1 to be slightly larger or smaller than M2 so that the capacitor can be charged. This difference will be amplified due to the positive feedback and the oscillation starts. Because the noise and device mismatch are not well defined, the start-up condition is not always the same. For some cases the oscillation starts with a negative voltage swing and for other cases the pulse will start with a positive swing. This effect can be clearly seen over 10 Monte Carlo device mismatch runs. This is depicted in Figure 5.9a.

To obtain a robust pulse generator, the initial pulse condition must be defined so that each pulse has the same phase. This is also required for some modulation schemes. Simple energy based receivers only measure the received energy, they do not measure the pulse phase. However, more complex receiver architectures such as BPSK (Binary Phase Shift Keying) also measure the phase. Since more information can be gathered using the same pulse energy, the BER performance for BPSK systems will be better compared to energy detecting systems. It is therefore desired that each transmitted pulse has a well defined phase.

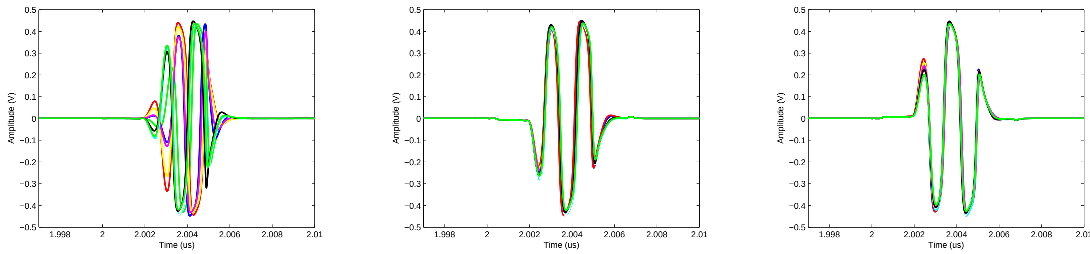

(a) Pulse without initial defined pulse condition

(b) Initial push right

(c) Initial push left

Figure 5.9.: Defining pulse shape by making the initial oscillator unbalanced guarantees the same pulse shape over device mismatch.

Defining the initial pulse condition can be achieved by making the oscillator unbalanced before the pulse is generated. For example, making M1 larger in size compared to M2 will make put the circuit in an initial unbalanced state. But the initial state will still depend on device mismatch and the circuit is also unbalanced during oscillation. A second approach is to inject an amount of charge at one side of the circuit at the moment the circuit is switched on. This will 'push' the oscillator into a defined unbalanced initial state. A single transistor circuit implementation (M9) is shown in Figure 5.7. The gate voltage of transistor M9 is driven with digital signal D_2. Due to the change in voltage, some charge on the transistor will be injected into the circuit. The improvement in pulse shape robustness can be seen in Figure 5.9b.

5.4.3. Realizing BPSK modulation

The concept of fixing the initial condition by injecting charge at one side of the circuit can be used to realize a transmitter capable of transmitting BPSK modulated pulses. By simply injecting charge at the left side or the right side of the circuit we can generate two types of pulses which are 180 degrees out of phase. The two different pulses are shown in Figure 5.9b and 5.9c. Note that the pulse shape is the same for each Monte Carlo device mismatch run. This implementation is extremely simple, does not affect the pulse shape and only requires one additional transistor.

5.4.4. Frequency tuning

As already mentioned in Section 5.3.2, the frequency tuning to compensate process variations will be done by changing the value of capacitor C. A varactor can be used so that the capacitance can be tuned by applying a tuning voltage. Standard varactors are not available in this technology, so it has to be realized using transistors. The accumulation-mode MOS varactor (A-MOS) shown in Figure 5.11a has some advantages above the inversion-mode varactor (I-MOS) and the diode varactor. A-MOS varactors, when used in LC oscillators, offer the lowest varactor losses and lowest phase noise, while the tuning range of the three varactors are comparable [70]. A typical accumulation-mode C-V curve is depicted in Figure 5.10. By choosing a bias point on this curve, the varactor capacitance can be controlled which makes it possible to tune the oscillating frequency.

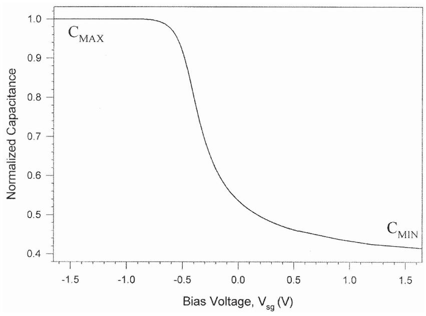

Figure 5.10.: Typical accumulation-mode MOS varactor C-V curve [71].

A problem occurs when the oscillator has to be switched on and off. If the oscillator is switched off, the drain voltage of M5 and M6 (the gate of the varactor) will be fixed to the supply voltage as mentioned before. When the circuit is switched on, the gate voltage of the varactor will drop down and starts to oscillate around approximately 1 V. Since the capacitance of the varactor is strongly related to the gate voltage, the capacitance will change drastically when the circuit is switched on or off. The result is that the oscillator's frequency of preference is changing during start-up.

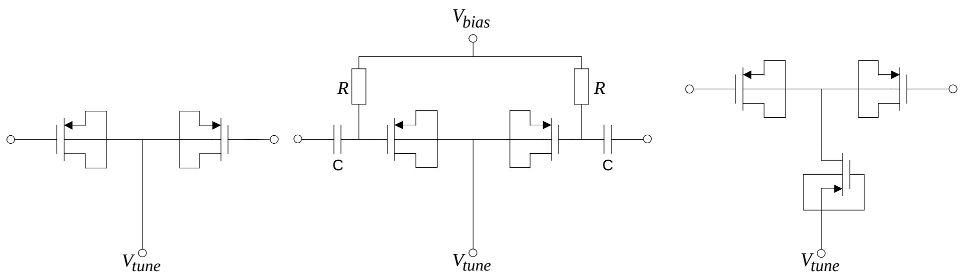

(a) No compensation (b) Separate biasing by coupling capacitors. (c) Constant biasing with large resistance.

Figure 5.11.: A-MOS varactor biasing methods

A way to solve this problem is to use a biasing method that separates the varactor gate voltage from the voltage swing at the drain of M5 and M6. A circuit implementation is shown in Figure 5.11b. The two coupling capacitors allow the varactor to be biased separately with a reference voltage. The drawback of this approach is that the two coupling capacitors must be (much) larger than the capacitance of the varactor to notice any effect of the varactor. It therefore requires a lot of valuable chip area.

In order to have a constant varactor biasing we notice that its body to gate voltage V_{bg} must be constant during oscillation. The gate voltage is determined by the oscillating voltage, so we have to adjust the body voltage. For example, if the gate voltage drops by 1.5 V, the body voltage must also drop by 1.5 V. A simple way to achieve this, is by adding a very large resistance between the tuning voltage and the body. The working principle will be explained with the aid of Figure 5.12.

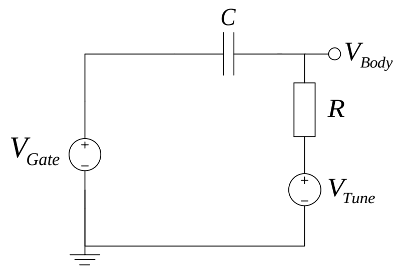

Figure 5.12.: Constant varactor biasing equivalent circuit

In this equivalent circuit the tuning voltage V_{tune} is fixed and V_{gate} is the varying gate voltage which ranges from the supply voltage (2.5 V) to 1 V. When the circuit is switched off, V_{gate} equals 2.5 V and the voltage at V_{body} equals V_{tune} because of the large resistor R. When the circuit is switched on, Vgate will drop and starts to oscillate around 1 V DC. Since V_{tune} is fixed, V_{body} must also drop with the same amount as V_{gate}. The result is that the varactor bias V_{Var}=V_{body}-V_{gate} is insensitive to the (large) variation in V_{gate}.

Figure 5.11c shows a MOS implementation where the resistance is implemented with a transistor with V_{gs}=0. The effectiveness of this solution can be seen in Figure 5.13. Figure 5.13a shows the varactor without the large resistance. Due to the large voltage drop during switching, the body-gate voltage varies with 1.8 V. If the large resistance is added as shown in Figure 5.11c, the plot in Figure 5.13b is the result. The body-gate voltage only changes 0.2 V at the moment the pulse is generated. The effect of the large voltage drop is not noticed by the varactor. This simple, low area and effective constant varactor biasing circuit has major advantages compared to the solution shown in Figure 5.11b. Therefore we will use the varactor implementation of Figure 5.11c.

This solution might also be useful for other applications that require capacitance tuning. It is then important to also consider the phase noise. We did not consider phase noise here since it is not important for UWB systems. We tested if the modified varactor in Figure 5.11c degrades the phase noise in a LC oscillator. Simulations showed that there was no noticeable effect on the phase noise or the tuning range. This can be explained by the fact the MOS noise sources are current dependent. Since this transistor has zero gate-source voltage, a negligible current is flowing through the transistor, causing negligible noise.

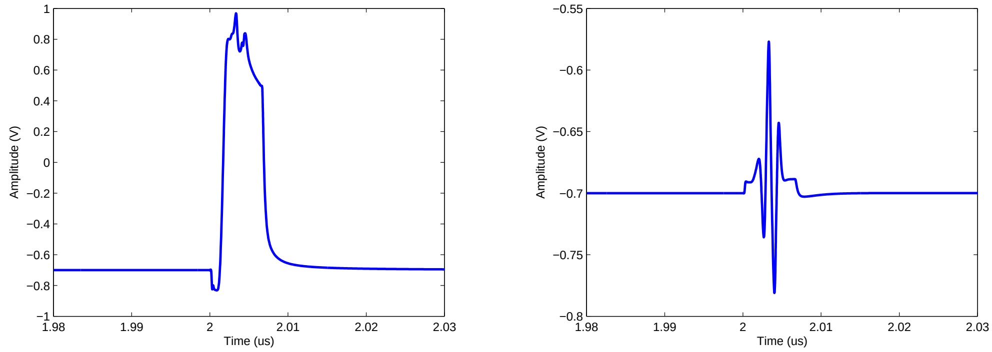

(a) No compensation, $\Delta V_{BG} = 1.8$ V

(b) Constant biasing, $\Delta V_{BG} = 0.2$ V

Figure 5.13.: Body-gate voltage during oscillation

5.5. Output Amplifier

The output stage must sense the pulse generator differential output voltage and convert it to a current. Hence, the resulting amplifier is a transconductance amplifier. If we consider a differential peak-to-peak voltage of 1 V, and the peak-to-peak output current to be 11 mA, a transconductance of 11 mA/V is required. The load of this amplifier is the earlier developed equivalent antenna model shown in Figure 3.12 on page 35. The input signal needs some special attention because the pulse generator is switched on and off. The moment the pulse generator circuit is enabled, the two input signal fed to the amplifier V_{in+} and V_{in-} make a large voltage drop and oscillate around a DC point of approximately 1 V as shown in Figure 5.14. An amplifier topology has to be chosen that

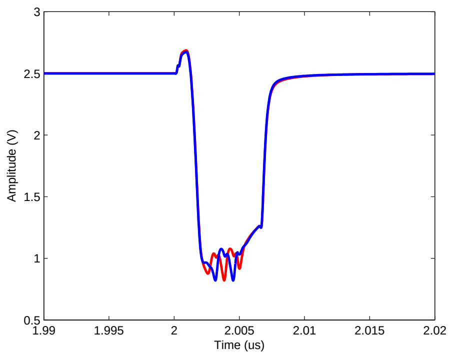

Figure 5.14.: Input voltage V_{in+} and V_{in-}.

can deal with these kind of input signals.

In order to minimize power consumption, a single ended output stage is preferred. To further reduce power consumption, the amplifier has to be completely switched off when there is no input data. It also has to provide some gain control to compensate for the tissue absorption and process variations.

5.5.1. Amplifier topology

Realizing a switchable variable gain amplifier with a transconductance of 11 mA/V is a challenging task. There is a large variety of transconductor stages to choose from. Linear transconductor amplifiers can be realized using multiplicative compensation which makes use of two stages that have an inverse transfer function. The overall transfer is therefore linearized. The transconductance gain is usually limited by the current and transistor size.

A different approach is to use negative feedback to increase the transconductance. Negative feedback will increase the input impedance, output impedance and the linearity. However, this amplifier does not require exceptional high linearity. The allowed amount of distortion depends on the pulse spectral efficiency requirements, which we will check later with simulations. Moreover, feedback is only beneficial if sufficient loopgain can be realized. The AMIS I3T25 0.35 μm technology was not chosen for its high frequency performance, making it difficult to create high loopgain at the targeted pulse center frequency. Negative feedback also involves a trade-off between bandwidth and overall gain. Since this amplifier needs a very large transconductance *and* large bandwidth, we have look for alternatives.

We will consider an amplifier which consists out of two parts: the input stage is a transconductance amplifier and the output stage a current amplifier. The proposed circuit is shown in Figure 5.15. A differential pair will sense the differential input voltage and convert it to a current. This current will be amplified using simple current mirrors. The complete amplifier will be designed in class A. The reason for this is that the complete pulse generating circuit, including output stage, will be switched off when no pulse is generated. It is expected that a class AB output stage will not result in significant reduction of power consumption.

5.5.2. Amplifier circuit design

The transconductance amplifier

The transconductance amplifier consists of M12 and M13. If we assume M19 to be an ideal current source and if M12 and M13 are matched and operate in saturation region, we can write the relationship of input voltage ($V_{diff} = V_{in+} - V_{in-}$) and output current ($I_{diff} = I_{D12} - I_{D13}$) to be [73]

$$I_{diff} = \frac{KW}{2L} V_{diff} \sqrt{\frac{4I_{Tail}}{K\frac{W}{L}} - V_{diff}^2} \tag{5.22}$$

where $K = \mu_{eff} C_{ox}$. If I_{Tail} is sufficiently large and V_{diff} sufficiently small, a fairly linear relationship can be obtained between input voltage and output current.

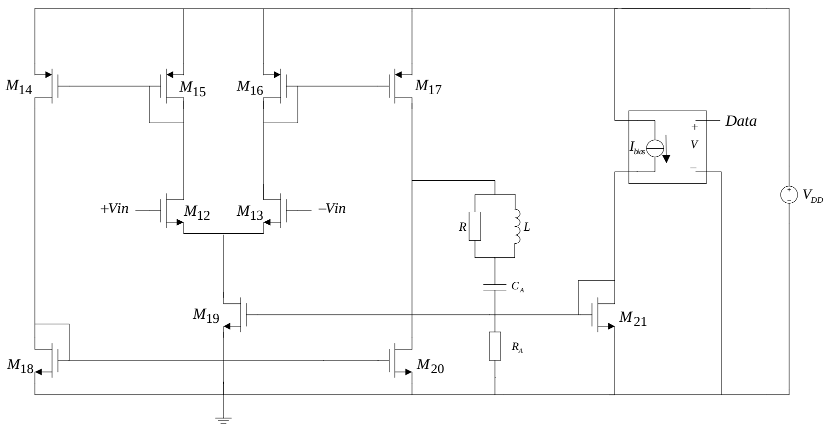

Figure 5.15.: Transconductance amplifier circuit implementation.

For large values of V_{diff}, one of the transistors will be switched off and the other will conduct the full tail current I_{Tail}. At this point, equation 5.22 is not valid since it assumes that both transistors are on. The voltage at which one transistor is switched off equals [73]

$$V_{diff,max} = \sqrt{\frac{2I_{Tail}}{K\frac{W}{L}}} \tag{5.23}$$

There is no increase in transconductance gain for $V_{diff} > V_{diff,max}$, which means that the amplifier starts to introduce distortion. We must therefore make sure that $|V_{diff}| < \sqrt{\frac{2I_{Tail}}{K\frac{W}{L}}}$ to obtain a reasonable linear transfer, meaning that W/L should be small. On the other hand we would like to have a large transconductance, which is proportional to W/L. An optimum has to be found for this ratio.

Before the W/L ratio is chosen, we must first determine a suitable range of I_{Tail} since this also has a large influence on the total power consumption. To obtain high current efficiency, it is required that a high percentage of the total current in the circuit flows through the output branch consisting of M17 and M20. This means that a high current mirror multiplication ratio of M17/M16 and M20/M18 is a must. Since we determined that the peak output current should be 5.5 mA and that the current mirror will be biased in class A, we require the bias current through M17 and M20 to be 5.5 mA.

We simulated the ac characteristics of a simple current mirror with different multiplication ratios and bias currents. It was found that the circuit performed well for a maximum current gain of approximately 15. If this current gain factor is used and the peak input voltage $V_{diff} = 0.5$, the minimum tail current should be biased at $I_{Tail} = 733\,\mu$A. With these numbers we can calculate the required W/L ratio to be 39. For minimum length L=0.35 μm it follows that W=14 μm.

The current amplifier

Now the dimensions of the transconductance amplifier are known, we must determine the optimum dimensions for the current mirror transistors consisting of M14, M15, M16, M17, M18 and M20. For this, we bias thetransconductance amplifier with an ideal current source and give I_{Tail}, M12 and M13 their calculated values. All PMOS transistors are made 2.5 times larger than the NMOS transistors to compensate for the higher electron mobility compared to the hole mobility. To obtain the optimum dimensions, we set the transistor length to the minimum value and sweep the transistor width while observing the pulse energy in load given by

$$E = \int_{t}^{t+1/PRF} i_{pulse}^2 R_{rad} dt \tag{5.24}$$

Looking at the result in Figure 5.16, it clearly shows a maximum pulse energy for a given transistor width. We will set the width of transistor M15, M16, M17, M18 and M20 to 7 μm.

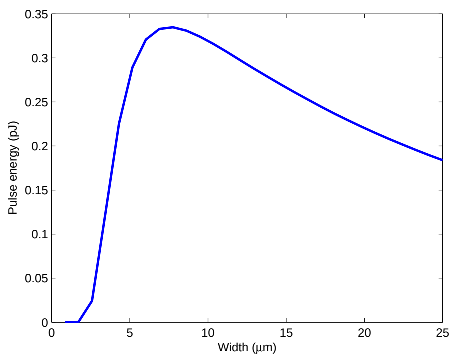

Figure 5.16.: Pulse energy vs. current mirror transistor width.

Some extra attention has to be spend on the output branch consisting of M17 and M20. Looking at the output node that connects the two drains and the antenna, we conclude that the voltage at this note is not well defined. This voltage will vary over process variations in an uncontrolled manner. The voltage cannot be set by the load since the antenna is mainly capacitive, no DC current flows through it. To properly bias this circuit, a bias feedback loop should be implemented which senses the output voltage node, compares this voltage to a reference voltage and adjusts a convenient node somewhere in the circuit. Disadvantage is that these kind of bias feedback loops can take a long time to settle. This poses no problem for most amplifier configurations. However, this *does* introduce a problem for this design since this amplifier is switched on and off within a few ns. If a bias loop is implemented, the amplifier has to be switched on before the pulse is generated to give the bias loop enough time too adjust the output node voltage. Since this can take a long time, it means that the circuit will consume the full circuit current when no pulse is generated and that power is consumed for no apparent reason.

To see if the voltage variation on the load is problematic, we must look at the antenna impedance and the voltage swing. It is important to include the reactance of the antenna since this is larger and varies more than the resistance. Simulations in CST Microwave Studio showed that when driving the antenna with a 5.5 peak current pulse, the maximum peak-to-peak voltage across the load is only 400 mV. The chance that transistor M18 or M20 will move out of saturation due to the antenna voltage swing is small if the voltage at the output node is somewhere in the middle of the supply voltage. This will have to be verified with process variation simulations.

5.5.3. Start-up effect on pulse in the antenna

Another problem is that an undesired current peak can be present in the antenna when the circuit is switched on. This can be caused by the a-symmetry of the circuit. Effects like these can be minimized by using a more symmetric circuit like a completely symmetrical amplifier with a differential output. Disadvantage is that this requires more current. And even so, all practical circuits will introduce some form of a-symmetry. A more brutal solution is to disconnect the antenna during turn-on, and connect it after the biasing in the circuit has settled. But this will most likely also introduce some sort of switching effect in the antenna. Moreover, it requires large transistors because of the high currents which have to be handled. Hence, adding components in the signal path is not an attractive solution. We will check how this turn-on current effect will influence the radiated signal with simulations in the next chapter.

Another effect is that the biasing of the circuit requires time to settle. If the amplifier is switched on at the same time as the pulse generator, the output current pulse will be distorted since the amplification occurs during the settling time of the amplifier. To solve this, we need to switch the amplifier on before the pulse generator is enabled. Hence, another digital signal is required for the switching of the output amplifier. We will call this signal D_3. The relation and realization of D_1, D_2 and D_3 will be discussed in the digital design in Section 5.6.

5.5.4. Variable gain control

A way of controlling the amount of gain should be included in this design. This is not only to compensate for the variations in tissue absorption and pulse amplitude, but also to comply with the FCC mask and to reduce power consumption if needed. The minimum gain should be based on how beneficial it is to transmit with very low emission levels to save power. If the power consumption becomes comparable to other subsystems, it does not add a significant reduction in power consumption to the whole system. We will decide the amount of variable gain in next chapter once the average power consumption and process variations of this circuit are known.

The principle of variable gain control used in this design is based on the switching of parallel connected transistors in a current mirror as shown in Figure 5.17. Instead

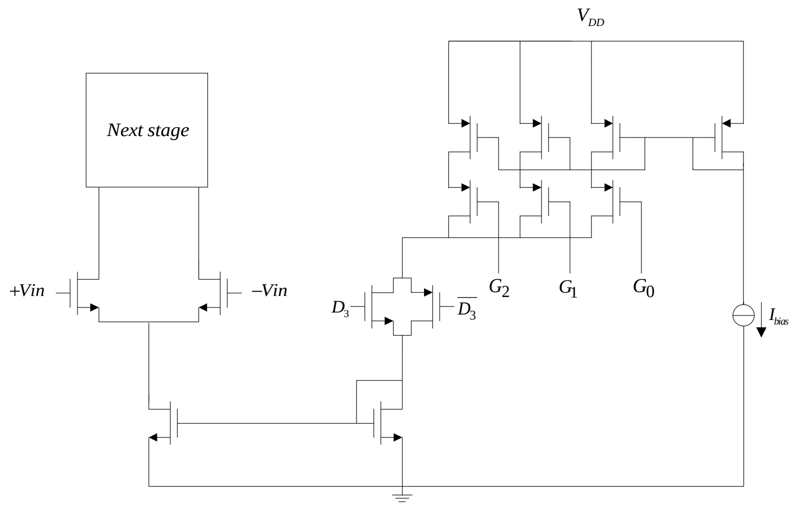

Figure 5.17.: Digital gain control with switchable current mirror.

of switching parallel transistors at the output branch (M17 & M20 in Figure 5.15), we will switch parallel transistors which control the tail current of the transconductance amplifier. This has several advantages compared to output branch switching. The currents are relatively small, making them easy to switch with small transistors. Moreover, the switching of the current sources takes place *outside* the rf path so that the pulse shape will not be affected. However, note that the range of variable gain is limited. The lower limit is set by the required tail current so that the amplifier still shows acceptable performance. The upper limit is set by the high current handling performance of the output transistors.

Eight different gain levels can digitally be set by a micro controller by making G_0, G_1 and G_2 logic '0' or '1'.

5.5.5. Current source implementation

Final step in the circuit design is to implement the bias sources. We need two switchable current sources for the pulse generator and one for the output transconductance amplifier. The current sources in this design are based on simple current mirrors as shown in Figure 5.18. It is assumed that a stable reference current is available in the implantable system which can be used to bias the pulse generator and the output amplifier.

Output impedance is one of the key design aspects of a current source. The channel length modulation will cause the output impedance to decrease because the effective channel length becomes smaller. This effect can be significant if minimum length transistors are chosen. If this is a problem, the length can be increased so that the effect of channel length modulation becomes less of influence. This will also make the gm smaller, so to compensate for this, the transistor width should be increased as well. However,

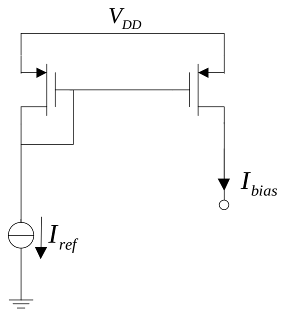

Figure 5.18.: PMOS current source implemented with a current mirror.

because of the increase W/L ratio, the capacitances will also increase. Also, the influence of process variations in current sources should be minimized. So, an optimum has to be found using simulations. We will deal with this in next chapter, where we will simulate the amplifier over all process variations.

Another challenge is to make the current sources switchable. This can be done by adding a single PMOS or NMOS transistors in series with the drain of the current mirror transistor. An NMOS device is effective at pulling a node to zero but is poor at pulling a node to a high voltage node such as V_{DD}. The output only charges up to $V_{DD} - V_{TH,N}$ since at this point the NMOS transistor turns off. Exactly the opposite holds for the PMOS transistor [74]. And as we already discussed, the threshold voltage can vary considerable over process corners.

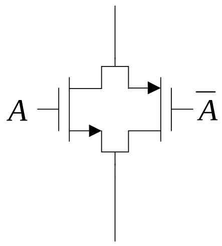

Figure 5.19.: Transmission gate

To avoid this voltage drop, we make use of a transmission gate shown in Figure 5.19 and implemented in Figure 5.17. This gate consists of an NMOS and PMOS transistors connected in parallel. By combining these transistors we can eliminate the threshold voltage drop since the node will always be charged to the right potential. Only a small voltage drop is observed due to the channel resistance.

The transmission gate has to be driven by two complementary digital signals. The realization of these digital signals will be discussed in the next section.

5.6. Digital Design

The three digital signals used in this design are D_1, D_2 and D_3. Signal D_1 is used to enable the current source of the pulse generator and also drives the charge-removing transistor M8. Signal D_2 controls the initial pulse condition circuit and also drives the two transistors M10 and M11 that connect the output nodes to the supply voltage after the pulse is generated. Signal D_3 enables the output amplifier.

Since properties such as input data time duration and modulation are not known yet, we have to make some assumptions here. We assume a digital signal named $DATA$ to be the given modulated data input and we will use this signal to realize all other digital signals. So a timing stage will be needed that modulates the original input data and converts it in to the $DATA$ signal which will be used in this design. Figure 5.20 shows the principle of realizing D_1, D_2 and D_3 using $DATA$, two delay blocks and two OR gates .

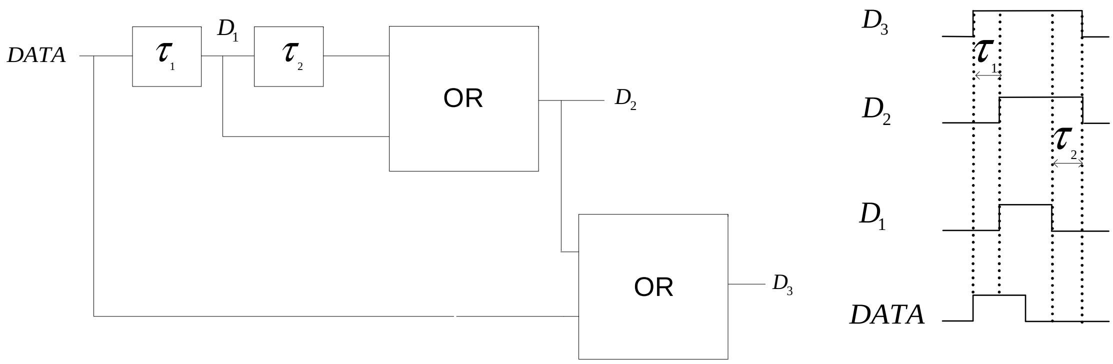

Figure 5.20.: Digital signal realization

The first delay block τ_1 controls the time duration between the enabling of the output amplifier and pulse generator. This delay gives the amplifier time to correctly biasing the circuit *before* the pulse is generated. Delay block τ_2 controls the amount of delay *after* the pulse is generated. This removes the pulse amplitude offset as explained in Section 5.4.1. An optimum combination of τ_1 and τ_2 must be found in terms of performance, pulse shape and power consumption. Note that only D_1, D_2 and D_3 will be used to enable and disable parts of the circuit. The $DATA$ signal will not be used for the switching action.

The accuracy of τ_1 and τ_2 does not have to be very high since D_2 and D_3 will be used for the switching action before and after the pulse is generated. Small variations in the delay will therefore not have a significant effect on the pulse shape. It will have a small effect on the average power consumption, so accurate delay blocks will minimize this influence.

Logic OR port

The logic OR gate is build using standard CMOS logic. A circuit implementation is shown in Figure 5.21.

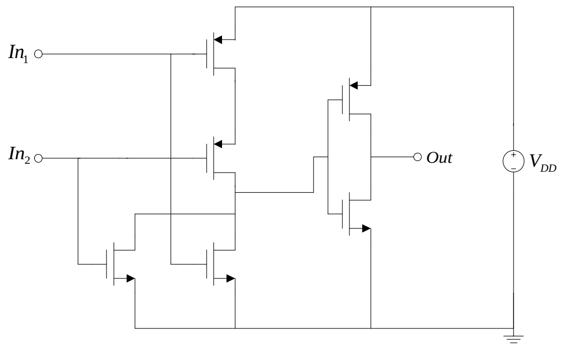

Figure 5.21.: CMOS logic OR gate implementation

Delay block

A simple way to implement a delay is using a cascade of current starved inverters. The delay can be controlled by adjusting the current which charges the inverter capacitances. However, due to the corner variations, the variation in the delay can be too large. Although this delay can be adjusted by a tuning voltage, it is not desired to calibrate the delay for each chip.

An alternative is to derive the delay using a reference clock. Unfortunately it is not known yet in this early stage of the design what clock frequency will be present in the system. We therefore have to implement the delay in the future when the clock properties are known.

At this point the circuit design is complete and the total UWB pulse generator circuit implementation is shown in Figure 5.22. The performance of this circuit will be thoroughly tested in the next chapter.

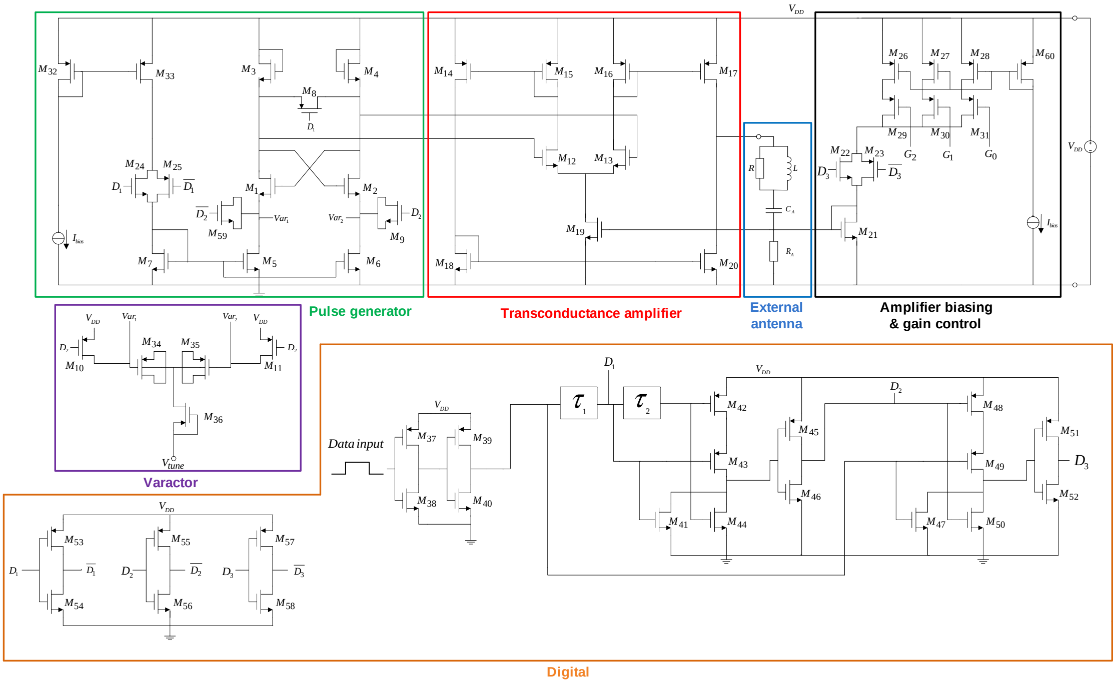

Figure 5.22.: Total UWB pulse generator circuit implementation.

5.7. Summary

A MOS-only sub-GHz UWB pulse generator is designed using the AMIS 0.35μm I3T25 technology. An oscillator based pulse generator was chosen as topology for its simplicity, low area and high efficiency properties. A relaxation oscillator was used as building block to realize the pulse generator since it can be designed robust over process variations and does not require inductors while it can generate nearly sinusoidal signals. The influences of process variations were taken into account during the circuit design and an expression was found which relates the required bias current to the desired operating frequency, robustness factor and differential output voltage.

A sudden change in pulse shape was observed when the circuit was switched off after enabling the oscillator. This was caused by the increase of pulse release time constant since the bias current of the transistors decreases when the circuit is switched off. This was solved by adding transistor M8 between the two output nodes to remove the charge.

The pulse shape during start-up is fixed by defining the initial pulse condition. This is done by injecting charge at one side of the circuit at the moment the oscillator is switched on. This puts the oscillator in a defined unstable initial state. This guarantees the same start-up condition each time the circuit is activated and eliminates the random influence of noise and mismatch in the circuit. BPSK modulated pulses can easily be achieved by injecting charge at the left side or the right side of the circuit.

A novel varactor biasing circuit was developed that keeps the varactor bias voltage constant even with large gate voltage variations which occur during the start-up of the oscillator. This solution does neither influence the tuning range nor phase noise.

The output amplifier consists of a cascade of a transconductance amplifier and a current amplifier. To keep the power consumption low, both amplifiers only consume power when a pulse is being generated. The transconductance amplifier consists of a simple differential pair and the current amplifier is implemented using current mirrors. Care has been taken to keep the output amplifier in the acceptable linear region for the given input signal.

To minimize the start-up effect of the output amplifier, the amplifier will be switched on before the pulse is generated. The time duration between the enabling of the output stage and pulse generator can be set by a delay block.

Digital variable gain control is achieved by adjusting the bias current of the transconductance amplifier in the output stage. Eight different gain levels can be selected by a micro controller to compensate for the variations in tissue absorption and pulse amplitude. This can also be used to comply with the FCC mask or to reduce power consumption if required.

The total circuit only consists of MOS transistors, making it excellent to be integrated on chip. The required supply voltage, when taking the worst case process corner into account, was found to be 2.5 V.

6. Simulation Results

In this chapter the circuit designed in previous chapter will be verified with simulations. In the first section the functionality of the circuit will be verified. After this, the robustness of the circuit is put to the test by varying process corners, device mismatch, load impedance, supply voltage and temperature. Finally, we will compare the designed circuit to other biomedical communication systems. All simulations will be done using Cadence RF Spectre.

6.1. Design verification

The design verification will be divided into several steps like the circuit design procedure in previous chapter. First, the pulse generator will be discussed.

6.1.1. Pulse generator

The functionality of the pulse generator will be verified first without the varactor and output amplifier circuit implementation. An ideal output amplifier with a transconductance gain of 11 mA/V is used to sense the differential output voltage and to drive the antenna with the required current. The capacitor C is implemented with an ideal capacitor. The width and length of transistor M8 is 2 μm and 0.35 μm, respectively. The current source transistors M32 and M33 are both given minimum length and a width of 0.5 μm, the multiplication factor of M33 is m=10. The width of the initial condition defining transistor M9 equals 2 μm.

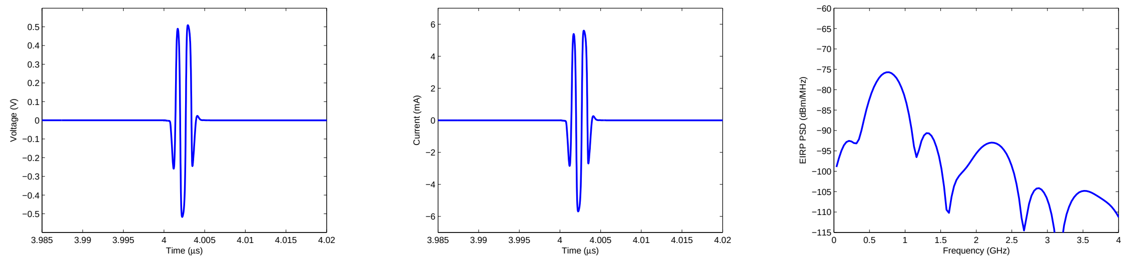

(a) Pulse generator output voltage (b) Current pulse in antenna (c) Pulse PSD

Figure 6.1.: Generated pulse with corresponding PSD

The generated pulse plotted in Figure 6.1 is obtained when the time duration of digital signal $DATA$ equals 3 ns. The properties of the (ideal) delay blocks are $\tau_1 = 1$ ns and

τ_1=0 because the output amplifier is not yet included in this simulation. Note that the EIRP PSD is based on the current in the antenna and takes the antenna losses into account. The pulse occupies a -10 dB bandwidth of 600 MHz centered around 750 MHz. This is larger than required, but recall that Section 4.5 on page 50 showed that the pulse bandwidth will decrease slightly due to the antenna gain characteristics. Thus, for now we will set the $DATA$ signal time duration to 3 ns. The calculated average pulse power equals 88.6 μW which is higher than the 54.95 μW calculated in the link budget on page 50.

To see how time variations in $DATA$ will change the pulse shape, we vary the time duration of $DATA$ from 2.5-3.5 ns. This is shown in Figure 6.2. A duration of 2.5 ns corresponds to a -10 dB bandwidth of 730 MHz, while the bandwidth for a 3.5 ns $DATA$ input equals 500 MHz. The change in pulse center frequency is negligible. So the bandwidth can be controlled by adjusting the time duration of $DATA$. But note that also the pulse energy will increase if the time duration is increased.

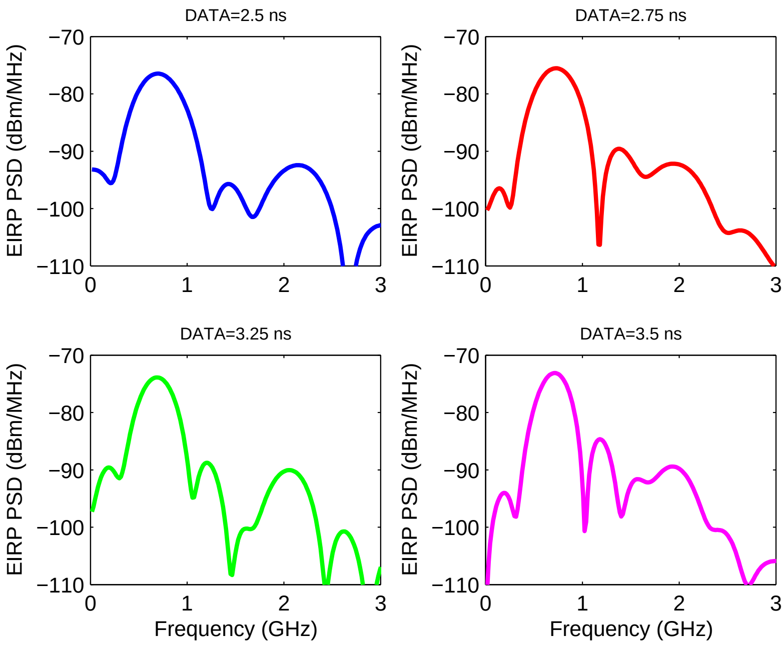

Figure 6.2.: Variation in digital signal 'DATA' length

To verify the performance over process corners, we simulate the pulse generator in the other 4 process corners (Figure 6.1 shows the generated pulse for the typical process corner). The value of the capacitor C is adjusted such that for each process corner the center frequency of the pulse f_0 equals 750 MHz. The PSD for each process corner is shown in Figure 6.3. Note that the corrected pulse shape and amplitude are almost identical for each corner. The required capacitance value to obtain f_0 = 750 MHz for each process corner is summarized in Table 6.1.

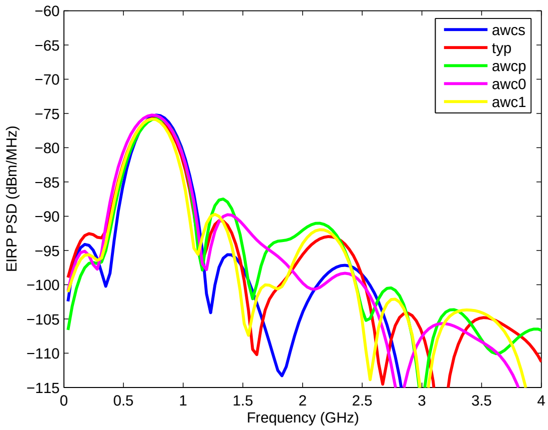

Figure 6.3.: Pulse PSD over all process corners.

Table 6.1.: Required capacitance value to obtain $f_0 = 750$ MHz

6σ corner	C (fF)
awcs	80
typ	110
awcp	140
awc1	135
awc0	85

Frequency tuning

Table 6.1 shows that the required capacitor tuning ratio C_{max}/C_{min} equals 1.75, which can be obtained by practical A-MOS varactors [70]. The maximum MOS capacitance of a transistor is equal to the oxide capacitance, hence

$$C_{max} = C_{ox} = \frac{\epsilon_0 \epsilon_r}{t_{ox}} WL \tag{6.1}$$

Note that since the two varactor transistors are connected in series, the required transistor capacitance of each transistor must be increased by a factor of 2. So, C_{max} must be equal to 280 fF to meet the requirements of Table 6.1. These minimum and maximum capacitance values provide the desired pulse center frequency in each process corner. A quick calculation shows that with these values, in the typical corner, the pulse center frequency can be tuned between 665 and 880 MHz. Although the higher frequency limit is high enough, it is desired that the pulse generator has the ability to be tuned at frequencies lower than 665 MHz. This will give the communication system more flexibility to choose a suitable operating frequency. We therefore have to increase the capacitance. This can be done by either adding a capacitor parallel to the varactor or to increase the transistor area. The parallel capacitor has the disadvantage that the tuning range will be reduced and that corner variation of the capacitor itself will introduce extra process variation. We therefore will increase the transistor area.

Normally, minimum length transistors are chosen to obtain maximum varactor quality factor Q. This is important if the varactor is used in an oscillator with low phase-noise requirements. However, this is not an issue for UWB pulse generators so the transistors length can be chosen larger. This has the advantage that a larger capacitor tuning ratio C_{max}/C_{min} can be obtained [70] and that the ratio of transistor length to width is still within practical limits. We set the transistor width to 14 μm and length to 5 μm.

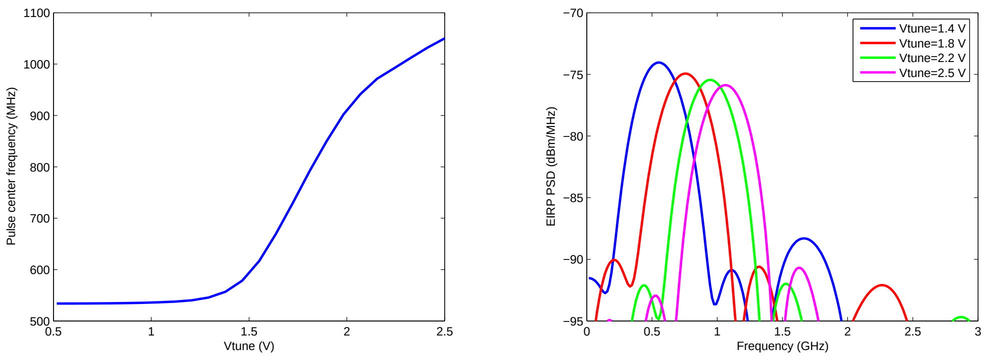

(a) Pulse center frequency f_0 vs. V_{tune}.

(b) PSD vs. V_{tune}.

Figure 6.4.: Tuning characteristics of the A-MOS varactor.

Figure 6.4 shows the pulse generator tuning characteristics of the A-MOS varactor in the typical process corner. The varactor covers a tuning range from 530 to 1050 MHz, which is large enough to cover all process variation and also offers a wide range of possible operating frequencies. The PSD in Figure 6.4b shows that the amplitude has a small variation over the tuning range. If required, this difference can be compensated by the gain control of the output amplifier.

6.1.2. Output amplifier

The previous simulation results are obtained with an ideal transconductance amplifier. The functionality of the complete circuit implementation shown in Figure 5.22 on page 83 will now be verified. The properties of the (ideal) delay blocks are given τ_1 = 1 ns and τ_1= 0.5 ns. One of the issues of the transconductance amplifier was the turn-on effect as discussed in Section 5.5.3. This effect can be observed in the gate bias voltage of the transconductance tail current transistor M19 as shown in Figure 6.5a. At the moment the amplifier is switched on, the gate voltage peaks and decays again. This also causes an undesired peak in the current pulse. Furthermore, we see that after the amplifier is switched off at 3.005 μs, the gate voltage slowly decays to zero. This happens because the gate voltage is only defined at the moment the circuit is switched on. During the OFF period, the gate voltage of M19 is not well defined and still allows some current to flow through M19. Consequently, there will also flow a much larger current through the output branch consisting of M17 and M20. So power is still being consumed while no pulse is generated.

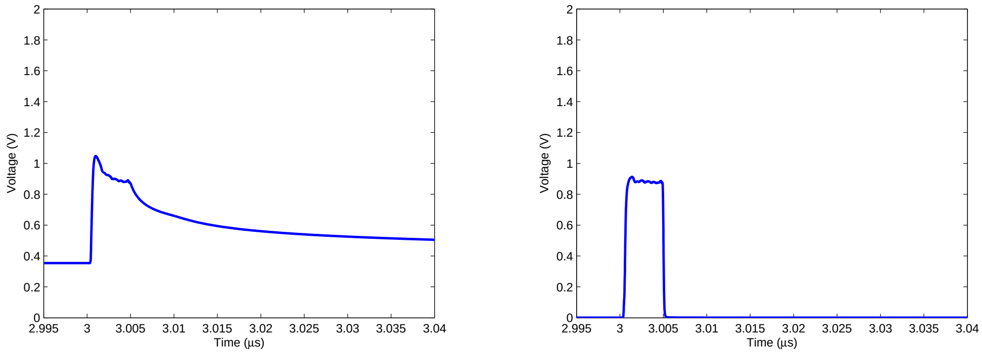

(a) Without transistor M61 (b) With transistor M61

Figure 6.5.: Gate bias voltage of transconductance tail current transistor M19

To solve this, transistor M61 was added that shorts the gate voltage of M19 to ground *after* the pulse is generated (the final circuit implementation can be seen in Figure 6.14 on page 97). The effect of this transistor can be seen in Figure 6.5b. Clearly, the gate bias voltage is well defined during the ON *and* OFF state of the amplifier. The turn-on effect is minimized and the power consumption is reduced significantly as we will see later.

Figure 6.6 shows the current pulse in the antenna and the corresponding PSD with the FCC mask. The pulse occupies a -10 dB bandwidth of 550 MHz centered at 750 MHz and the average pulse power equals 118 μW.

Looking at this result we see that the pulse Power Spectral Density (PSD) has side lobes that are at least 18 dB below the main lobe. These side lobes will be attenuated even more because of the antenna gain frequency behavior. The varactor tuning voltage used is 1.8 V.

Average power consumption

The average current consumption of the total circuit (without transistor M61) when using a Pulse Repetition Frequency (PRF) of 1 MHz is 49 μA. Note that this does not include the reference current source that we assume to be available in the implantable system.

For a supply voltage of 2.5 V this results in an average power consumption of 122.5 μW. When transistor M61 is added to the circuit, the average power consumption is reduced to 78 μW. So transistor M61 offers a 57% reduction in power consumption without changing the pulse shape. The average power consumption scales linearly proportional with the PRF.

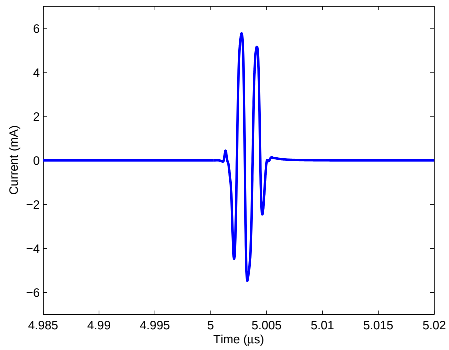

(a) Current pulse in the antenna

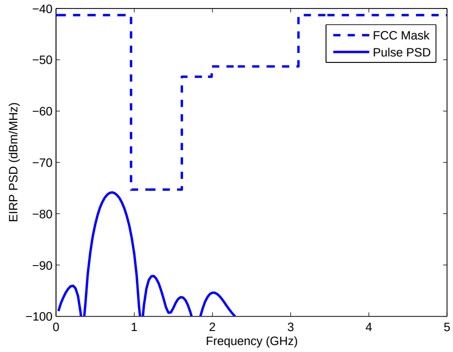

(b) Pulse PSD and FCC mask

Figure 6.6.: Final antenna current pulse and PSD.

Gain control

The digital gain stage can be controlled in 8 different levels. The ratio of the three parallel switching transistors is 8:4:2. The average pulse power and average power consumption versus digital control is shown in Figure 6.7. Note that the average pulse power is given by

$$P_{pulse} = \frac{1}{T_{pulse}} \int_{t}^{t+1/PRF} i_{pulse}^2 R_{rad} dt \tag{6.2}$$

and that the average power consumption is calculated using

$$P_{avg} = PRF \int_{t}^{t+1/PRF} I_{supply} V_{DD} dt \tag{6.3}$$

The average pulse power can be adjusted from 10 μW to 225 μW. Hence, a 13.5 dB tuning range can be achieved. The corresponding average power consumption ranges from 30 μW to 150 μW. Note that the increase in pulse power between digital=110 and digital=111 is very small. However, digital=111 is required to compensate for the lower gain in the worst case speed corner. Digital 001 can be used for the worst case power corner, but cannot be used in the typical corner since the transconductance amplifier will not be biased correctly anymore.

6.2. Process, antenna impedance, temperature and power supply variations

The robustness of the total circuit will be tested in this section by introducing various practical variations to the circuit.

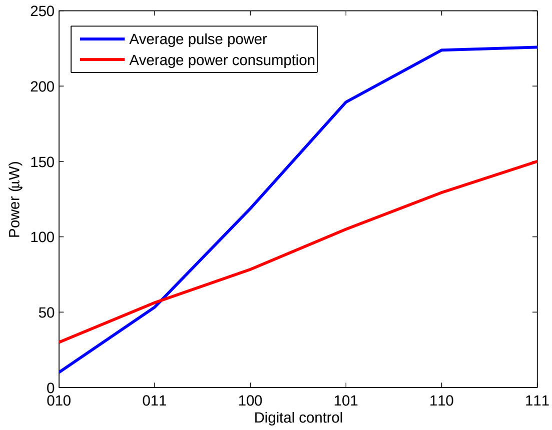

Figure 6.7.: Digital gain control vs. average pulse power and average power consumption for PRF=1 MHz.

6.2.1. Process corners

Although the performance of the pulse generator was already tested over process corners in Section 6.1.1, we will now verify the performance of the entire circuit. The simulated PSD for the awcs, awcp, awc0 and awc1 process corner is shown in Figure 6.8.

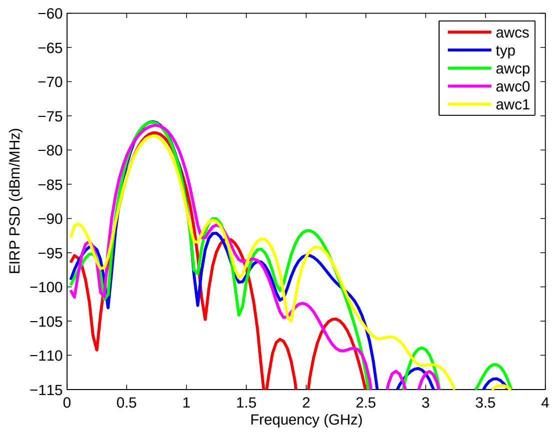

Figure 6.8.: PSD over worst case process corners

Although the pulse amplitude shows some small variations over the different process corners, this can be compensated by the digital gain control. The circuit shows correct functionality over all process corners.

6.2.2. Device mismatch

The effect of mismatch between identically designed MOS transistors is checked with a Monte Carlo simulation. Figure 6.9 shows the effect of device mismatch on the current pulse shape over 200 Monte Carlo runs.

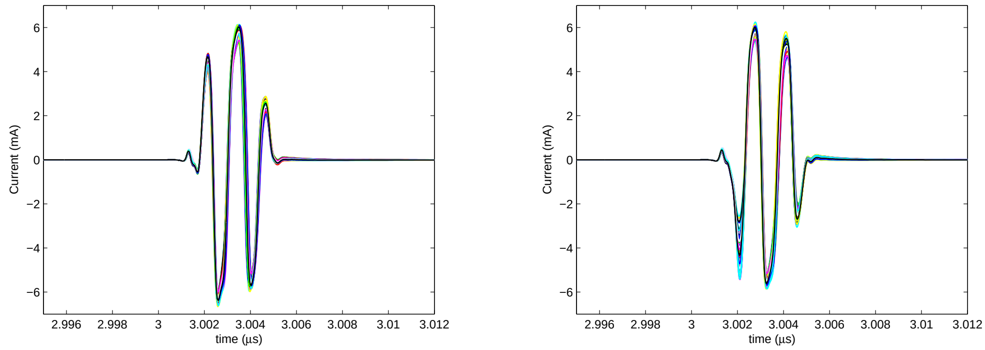

(a) BPSK '0' (b) BPSK '1'

Figure 6.9.: Monte Carlo simulations (200 runs, Digital=100)

From this figure we can conclude that the effect of device mismatch on the pulse shape is acceptable. The distribution in average pulse power and average power consumption is shown in Figure 6.10. Note that the Monte Carlo distribution has a typical bell-shaped curve. This gives a good indication of the statistical device mismatch performance. The worst case variation in pulse center frequency is only 30 MHz, which can easily be compensated by the varactor.

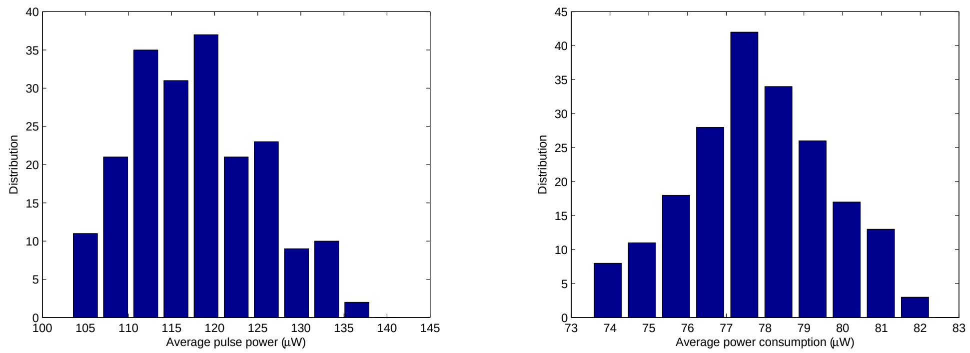

(a) Average pulse power (b) Average power consumption

Figure 6.10.: Monte Carlo distribution results (200 runs, Digital=100)

6.2.3. Antenna impedance

One of the main goals in this work is to make the wireless biomedical communication more reliable. This is achieved by driving the antenna with a current source so that the radiated pulse shape is insensitive to impedance variations of the implantable antenna. To verify this, we observe the change in current pulse shape while the antenna reactance is varied (we only vary the reactance since the variation in the antenna resistance is considerably less). The reactance is varied with the same amount we observed during measurements and simulations. This corresponds to the following component values in the antenna equivalent circuit model in Figure 6.11 : $3.5 \leq C_A \leq 5.5$ pF and $5 \leq L \leq 7$ nH, while R and R_A are held constant.

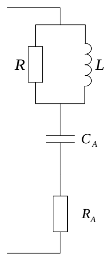

Figure 6.11.: Antenna equivalent circuit model for 300-900 MHz, $R_A = 10\,\Omega$, $3.5 \leq C_A \leq 5.5$ pF, $R = 400\,\Omega$, $5 \leq L \leq 7$ nH.

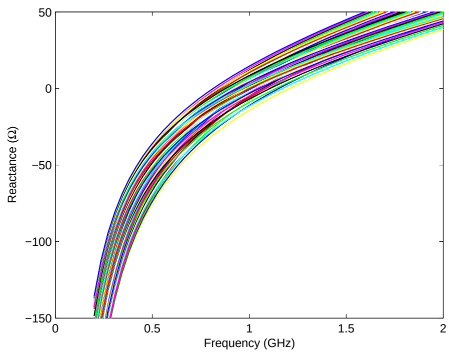

Figure 6.12.: Varying antenna reactance

The variation in antenna reactance is shown in Figure 6.12 and the effect on the two BPSK modulated pulses can be seen in Figure 6.13a and 6.13b. Clearly, this pulse generator circuit implementation is very robust against antenna reactance variations. This not only guarantees that the desired power is always delivered to the radiation resistance, but also allows us to better predict the received pulse shape. With proper receiver architecture and signal processing, this can improve the receiver sensitivity, allowing the receiver to receive signals with a very low signal-to-noise ratio.

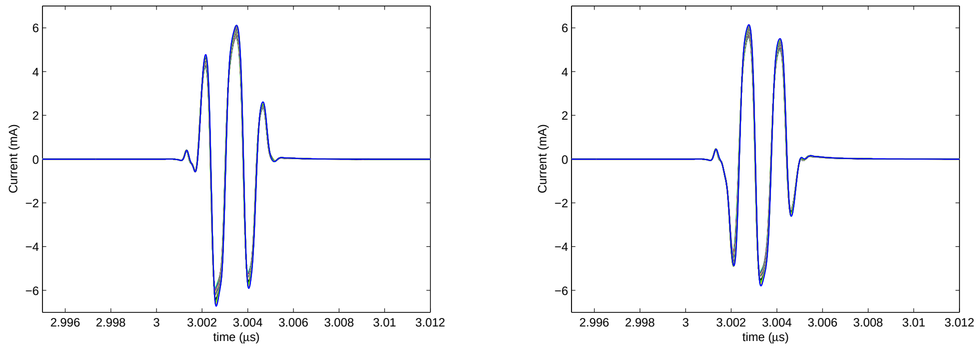

(a) BPSK '0'

(b) BPSK '1'

Figure 6.13.: Effect of varying antenna reactance on pulse shape

6.2.4. Temperature

The temperature in the human body rarely changes more than a few degrees. Still, we swept the temperature from 0 to 80 °C to see how this pulse generator performs over a large temperature range. Simulations showed that the change in pulse amplitude and center frequency was less than 6%, which gives the indication that this circuit implementation is very robust over temperature variations. For temperatures between 30 and 45 °C the change in amplitude and frequency is only 1% and therefore is negligible.

6.2.5. Supply voltage

Although we assumed that a power management system provides a stable power supply, it is important to also simulate the effect of variations in the supply voltage. Simulations showed that a 10% increase in supply voltage results in a 18% *decrease* in pulse center frequency. It was found that this was caused by an decrease in varactor body-gate bias voltage. If the pulse generator is switched off, the body voltage equals the tuning voltage and therefore does not change with varying supply voltage. However, the gate voltage increases with increasing supply voltage, increasing V_{BG} and makes the varactor capacitance larger for the same tuning voltage. This can easily be compensated for by adjusting the tuning voltage. However, it is realized that the supply voltage can fluctuate over time. It is therefore important to minimize this effect.

Since the used varactor provides a large tuning range, the pulse center frequency is sensitive to small variations of the varactor biasing (supply and tuning voltage). To minimize this effect, we can decrease the tuning range by adding a parallel capacitor to the varactor and decrease the varactor transistor size. This has been verified using a 50 fF highly linear floating capacitor and we reduced the size of both varactor transistors to

W=12 μm and L=3 μm. With this new configuration, a 10% change in supply voltage only results in a 5% change in pulse center frequency. The tuning range in the typical corner is reduced to 600 - 900 MHz. This is still large enough to cover all process corners and device mismatch.

So, it can be decided to improve robustness against supply voltage variations at the cost of reduced tuning range, or to rely on the performance of the power management system.

6.3. Final circuit implementation

The final circuit implementation is shown in Figure 6.14. All transistor parameters are summarized in Table 6.2.

Table 6.2.: Final circuit implementation transistor parameters

Transistor	W (μm)	L(μm)	m
$M_{1,2}$	9	0.35	1
$M_{3,4}$	5	0.7	1
$M_{5,6}$	5	0.7	2
M_7	5	0.7	1
M_8	2	0.35	1
$M_{9,59}$	5	0.35	1
$M_{10,11}$	2	0.35	1
M_{24}	2	0.35	1
M_{25}	5	0.35	1
M_{32}	2	1	1
M_{33}	2	1	10
$M_{34,35}$	14	5	1
M_{36}	0.5	0.35	1

(a) Pulse generator

Transistor	W (μm)	L(μm)	m
$M_{12,13}$	14	0.35	1
$M_{14,15,16}$	16	0.35	1
M_{17}	16	0.35	15
M_{18}	8	0.35	1
M_{19}	5	0.7	15
M_{20}	8	0.35	15
M_{21}	5	0.7	1
M_{22}	2	0.35	1
M_{23}	5	0.35	1
M_{26}	6	1	8
M_{27}	6	1	4
M_{28}	6	1	2
$M_{29,30,31}$	4	0.35	1
M_{60}	6	0.35	1
M_{61}	5	0.35	1

(b) Transconductance amplifier

τ_1	1	ns
τ_2	0.5	ns
$DATA$	2.5	ns
V_{DD}	2.5	V
I_{Bias}	4	μA

(c) Pulse generator and performance

Transistor	W (μm)	L(μm)	m
$M_{37,39,42,43,48,49,53,55,57}$	2.5	0.35	1
$M_{38,40,41,44,47,50,54,56,58}$	1	0.35	1
$M_{45,51}$	7.5	0.35	1
$M_{46,52}$	3	0.35	1

(d) Digital circuit

Comparison with other biomedical communication systems

There are not a lot of biomedical RF transmitters available on the market today, which makes it hard to make a good comparison on the circuit performance. On top of that, biomedical RF transmitters use different communication schemes, frequency bands, targeted wireless range and bitrate. Also this design uses a small electric antenna which has a low radiation resistance. This requires more current compared to antennas with a higher radiation resistance since the transconductance amplifier must be capable of delivering a high peak current.

One of the commercially available implantable RF transceiver is the Zarlink ZL70101 [48]. This transceiver operates in the MICS 402-405 MHz band and offers a maximum raw data rate of 800 kb/s. The continuous power consumption of the entire transceiver in transmitting and receiving mode equals approximately 12.5 mW. Note that this power consumption includes the receiver and the digital part as well. Although the datasheet does not provide the distribution of the power consumption, usually the transmitter is a dominant factor for power consumption. Even if we assume that the transmitter only contributes 10% of the total power consumption (1.25 mW), still the power consumption of this design (30 μW to 150 μW) is considerably lower.

Thus, we can carefully say that this designed biomedical transmitter can offer a higher bitrate while consuming less power compared to the Zarlink ZL70101.

6.4. Summary

The performance of the pulse generator circuit implementation was tested in this chapter using Cadence RF Spectre simulations. We can concluded that the circuit performs well over all process corners and device mismatch, meaning that the circuit is robust and giving a strong indication that the majority of the fabricated circuits will fall within the performance specifications. Furthermore, it was shown that this circuit implementation is very robust against antenna reactance variations. This guarantees that the desired power is always delivered to the radiation resistance and also allows us to better predict the received pulse shape, thereby increasing the reliability of the communication link.

It was shown that the pulse center frequency is sensitive to supply voltage variations since this has a direct influence on the varactor biasing. Therefore, a reliable and constant power supply is required. To minimize this effect, a capacitor can be added in parallel to the varactor at the expense of reduced frequency tuning range.

The pulse center frequency can be controlled from 0.55 - 1.1 GHz (or 600 - 900 MHz for better rejection of supply voltage variations) by adjusting the control voltage of the varactor. The -10 dB bandwidth equals 550 MHz and the digital gain control offers a 13.5 dB tuning range. For a 2.5 V supply and a 1 Mb/s raw bitrate the average power consumption ranges from 30 μW to 150 μW, depending on the pulse power controlled by the digital gain. This is considerably lower compared to commercially available implantable RF transceivers.

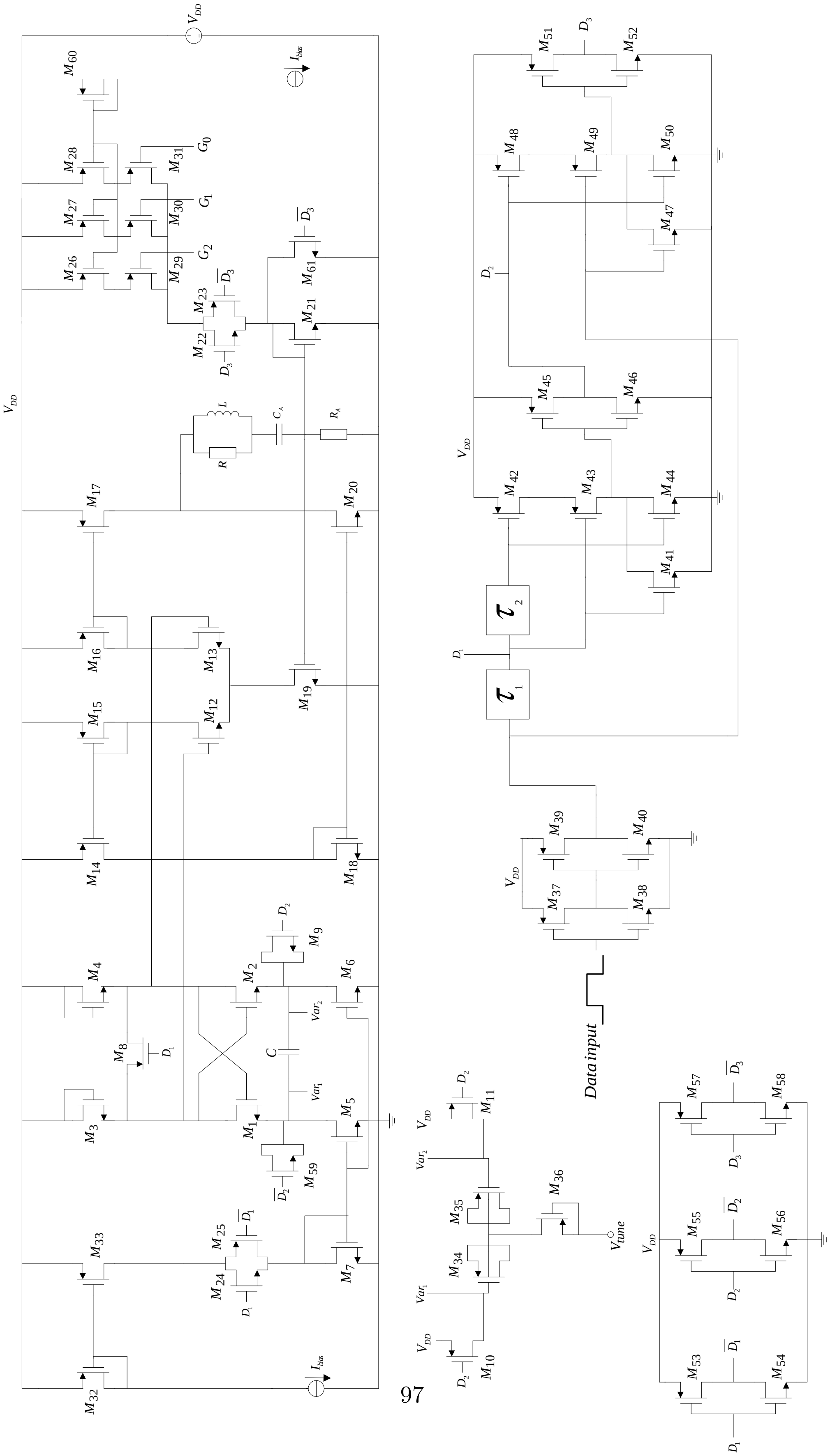

Figure 6.14.: Final pulse generator circuit implementation.

7. Conclusions and Recommendations

In this chapter the conclusions of each chapter are summarized in the conclusions. This is followed by an overview of the scientific contributions made in this work. Subsequently, a list of recommendations is provided for future work.

Conclusions

Implantable medical devices equipped with wireless communication can improve the treatment of medical disorders and thus improve the quality of life. Today's wireless biomedical communication systems do not meet all the requirements such as reliability, power efficiency and wireless range. This was the reason to investigate sub-GHz UWB biomedical communication. This new concept can offer all the above mentioned requirements and also has negligible tissue heating due to the low average emission level.

The electric characteristics of various human tissues were investigated to estimate the power absorption of the tissue over a broad frequency range. A layered tissue model consisting of muscle, fat, skin and free space was studied to model the human body and a power transfer factor was derived to calculate the absorbed power. It was found that although the optimum operating frequency varies with each patient, the best tissue penetration is achieved at sub-GHz frequencies. Increasing layer thickness or adding another layer will decrease and shift the optimum operating frequency to lower frequencies.

Various UWB electric dipole antennas were fabricated and immersed into muscle simulating liquid and raw pork meat to measure the input impedance. The result of these measurements was that all antennas showed a highly similar input resistance between 300-900 MHz. The variation in antenna reactance was more compared to the variations in antenna resistance. Based on these measurements, an antenna equivalent circuit model was developed which is valid in this frequency range. This lead to a detailed antenna-electronics interface investigation. It was found that for this application a *current* driven antenna results in the most reliable signal transfer. This is a fundamentally different approach of terminating an antenna compared to the traditional 50 Ω interface. Other antenna characteristics such as gain, efficiency and radiation pattern were simulated in CST Microwave Studio. Simulations showed that the antenna has a high ohmic efficiency despite the low radiation resistance and large reactance. This is due to the fact that the power delivered to the radiation resistance is independent of the reactance when the antenna is current driven. The antenna therefore does not suffer from impedance mismatches that can dominate the overall efficiency in conventional interfaces. Simulations also confirmed that a current driven antenna indeed was superior to the voltage and power driven antenna. The implantable antenna has an omnidirectional radiation pattern below 1 GHz, but quickly deviates from this typical dipole pattern with increasing frequency.

A system level design was carried out to obtain the design specifications for an UWB pulse generator. Variables such as bitrate, (indoor) UWB path loss, environment loss, battery capacity and receiver architecture were taken into account to obtain a realistic link budget. It was decided to use a 500 MHz bandwidth pulse centered at 750 MHz. We used a raw bit rate of 1 Mb/s in the link budget calculation, but this can be higher or lower depending on the application. It was also shown that the RF electromagnetic energy absorption with this link budget is well within the regulation limits. The radiated pulse power in this design is too low and the exposure duration to short to cause any significant tissue heating.

A MOS-only sub-GHz UWB pulse generator is designed using the AMIS 0.35μm I3T25 technology. An relaxation oscillator based pulse generator was chosen as topology for its simplicity, low area and high efficiency. The influences of process variations were taken into account during the circuit design and an expression was derived that relates the required bias current to the desired operating frequency, robustness factor and differential output voltage. The pulse shape during start-up is fixed by defining the initial pulse condition. This is done by injecting charge at one side of the circuit at the moment the oscillator is switched on. This puts the oscillator in a defined unstable initial state. This guarantees the same start-up condition each time the circuit is activated and eliminates the random influence of noise and mismatch in the circuit. BPSK modulated pulses can be generated by injecting charge at the left side or the right side of the circuit. Furthermore, a MOS-varactor is designed to make the oscillator tunable in frequency. A novel varactor biasing circuit was developed that keeps the varactor bias voltage constant even with large gate voltage variations which occur during the start-up of the oscillator. This solution does neither influence the tuning range nor phase noise.

The output amplifier consists of a cascade of a transconductance amplifier and a current amplifier. To keep the power consumption low, both amplifiers only consume power when a pulse is being generated. The transconductance amplifier consists of a simple differential pair and the current amplifier is implemented using current mirrors. Care has been taken to keep the output amplifier in the acceptable linear region for the given input signal. Digital variable gain control is achieved by adjusting the bias current of the transconductance amplifier. Eight different gain levels can be selected by a micro controller to compensate for the variations in tissue absorption and pulse amplitude. This can also be used to comply with the FCC mask or to reduce power consumption if required.

The performance of the pulse generator circuit implementation was tested using Cadence RF Spectre simulations. We can concluded that the circuit performs well over all process corners and device mismatch, meaning that the circuit is robust and giving a strong indication that the majority of the fabricated circuits will fall within the performance specifications. Furthermore, it was shown that this circuit implementation is very robust against antenna reactance variations. This guarantees that the desired power is always delivered to the radiation resistance and also allows us to better predict the received pulse shape, thereby increasing the reliability of the communication link.

Simulations showed that the pulse center frequency is sensitive to supply voltage variations since this has a direct influence on the varactor biasing. Therefore, a reliable and constant power supply is required. To minimize this effect, a capacitor can be added in parallel to the varactor at the expense of reduced frequency tuning range.

The pulse center frequency can be controlled from 0.55 - 1.1 GHz (or 600 - 900 MHz for better rejection of supply voltage variations) by adjusting the control voltage of the varactor. The -10 dB bandwidth equals 550 MHz and the digital gain control offers a 13.5 dB tuning range. For a 2.5 V supply and a 1 Mb/s raw bitrate, the average power consumption ranges from 30 μW to 150 μW, depending on the pulse power controlled by the digital gain. This is considerably lower compared to commercially available implantable RF transceivers.

Summary of Scientific Contribution

The following scientific contributions are the result of this work:

- *The concept of sub-GHz UWB biomedical communication is introduced*
  We proposed the concept of using sub-GHz UWB communication applied to implantable medical devices. The combination of sub-GHz and UWB makes is very interesting for wireless biomedical communication since UWB can offer high channel capacity, reliable communication, negligible tissue heating and ultra-low power systems. The advantage of using sub-GHz is the low path loss, good tissue penetration and low power electronics.

- *Investigated and modeled the electrical characteristics of human tissue*
  The electric characteristics of various human tissues were investigated to find the best operating frequency for sub-GHz UWB biomedical communication. A frequency dependent power transfer factor was derived for a layered tissue model consisting of muscle, fat, skin and free space to calculate the absorbed power over a broad frequency range. Also the influence of variations in tissue properties were investigated.

- *Fundamental research on electronics-antenna interface*
  The UWB properties of an implantable antenna are investigated. Implantable antenna measurements and simulations were done and an antenna equivalent circuit model was developed based on these results. The antenna-electronics interface was studied in great detail to obtain the most reliable signal transfer. It was found that for this application a *current* driven antenna offers the highest degree of reliability. This is a fundamentally different approach of terminating an antenna compared to the traditional 50 Ω interface. Also implantable antenna characteristics were investigated such as gain, efficiency and radiation pattern.

- *A robust MOS-only pulse generator is designed*
  A pulse generator based on a relaxation oscillator is designed that is very robust over process and antenna reactance variations. This circuit only consist of MOS

transistors, making it easy to be integrated on chip. The pulse generator is capable of generating BPSK modulated pulses and is tunable in frequency and output power. Furthermore, a novel varactor biasing circuit was developed that keeps the varactor bias voltage constant even with large gate voltage variations which occur during the start-up of the oscillator. The average power consumption is very low since the complete circuit only consumes power when a pulse is generated.

Papers and posters

- Published paper presented at the BIOCAS conference (Biomedical Circuits and Systems Conference) at Paphos, Cyprus, November 3-5, 2010
  Mark Stoopman and Wouter A. Serdijn, "*Sub-GHz UWB Biomedical Communication*"

- Published paper and poster presented at the ProRISC conference (Program for Research on Integrated Systems and Circuits), Veldhoven, the Netherlands, November 18-19, 2010, Mark Stoopman and Wouter A. Serdijn, "*Sub-GHz UWB Biomedical Communication*"

- Poster presented at the Microsystem and Innovation symposium organized by DIMES, Delft, April 27, 2010
  Marijn N. van Dongen, Senad Hiseni, Mark Stoopman, Chi Wing Wu and Wouter A. Serdijn "*Closed-loop Fully Implantable Neuromodulator System*"

Recommendations

Some recommendation are listed below for future work.

- *Antenna design*
  The results in this work are based on the measurements and simulations of a simple UWB antenna which is not specifically designed for implantable applications. With the proper antenna design, the implantable antenna radiation characteristics can be improved compared to the antenna used in this work. If the radiation resistance can be increased, this will reduce the required power consumption of the output amplifier. An interesting miniaturization of an UWB bow-tie antenna is given in [76], which is designed for the 300-960 MHz band and offers a 46% reduction in area compared to conventional bow-tie antennas. It is also suggested to look at the miniaturization technique used in [35].
  Antenna isolation is another important issue for implantable antenna design to improve radiation efficiency. Some research has already been done and can be found in [6].

- *Circuit design*
  The power consumption of this pulse generator circuit implementation can be decreased, but this will degrade the robust performance over process variations. Moreover, the total power consumption is dominated by the output amplifier so the relative improvement in power efficiency will be low if one wants to reduce the power consumption of the pule generator. It is therefore suggested to investigate how much the total power consumption can be reduced by using a more efficient output stage such as a class AB amplifier.
  Also the delay blocks has to be implemented. As already mentioned, the accuracy of τ_1 and τ_2 does not have to be very high since digital signal D_2 and D_3 will be used for the switching action before and after the pulse is generated. It is suggested to use a reference clock that is available in the system.

- *Integration with other subsystems*
  A timing stage has to be designed that modifies the input data such that it can directly control the pulse generator. Since this pulse generator is able to generate BPSK modulated pulses, this modulation has to be included in the timing stage design.
  The performance of the power management subsystem is important for the robustness of the pulse generator against power supply variations. If the supply voltage can fluctuate more than 5% over time, it is suggested to add a capacitor parallel to the varactor. This will reduce the frequency tuning range, but will significantly improve the circuit robustness against supply voltage variations. The details can be found in Section 6.2.5 on page 94.

- *Layout issues*
  During the layout, care must be taken to the combination of transistor M1&M2,

M3&M4 and M5&M6 as they are a dominant factor for device mismatch effects. Furthermore, simulations showed that the circuit performance is sensitive to parasitic capacitances between the drain of M1 and M2 (the two differential output voltage nodes). This must be taken into account during layout in order to minimize capacitance.
The output stage should be located close to the bondpad that connects the electronics to the external antenna. Although we do not expect a lot of problems here, it may be important to reduce the parasitic inductance. An example of an integrated chip on the back side of an antenna can be found in [26].

- *Receiver design*
  At the time of writing this thesis, a sub-GHz UWB receiver architecture for wireless biomedical communication is being investigated. The effect of in-band interference is expected to be a dominant factor for the wireless link performance and has to be taken into account. Since it has been shown in this work that the pulse shape can be better predicted than initially was assumed, this can be taken as an advantage. However, this will depend on the used receiver topology. In this work we assumed an energy detection receiver with OOK modulation. If it turns out that another receiver topology can achieve better performance, the link budget should be adjusted. But it is likely that this will not have a negative impact on the link budget since a reasonable high energy per bit to noise power spectral density ratio (E_b/N_0) is used in this work.

- *Measurements*
  When the chip is fabricated, its performance has to be tested. First, the electrical performance of the test chip itself must be verified. For correct functionality, the load should be implemented by the same antenna equivalent circuit model used in this work. One of the biggest drawbacks of using a current driven antenna is that the chip will be difficult to verify with measurements. The problem is that almost all measurement equipment is based on a 50 Ω interface. Since the electronics and antenna are not designed for a 50 Ω interface, this introduces some measurement challenges.
  The test chip should be equipped with various measurement point along the signal path to measure analog and digital signals. Also important biasing points have to be measured since testing for correct biasing is the first step in the measurement process. Given the frequencies used in this work, it is possible to verify the performance by measuring the time-domain pulses using an oscilloscope. Care must be taken to include the loading effects of the measuring probes since this can influence the measurement accuracy. The PSD of the generated pulse can be calculated by inserting the measured data into Matlab.
  Once the chip has been electrically verified, the chip (including antenna) should be placed inside a phantom which simulates the human body. Measurements done in free space will not give the correct results since the radiation characteristics will shift up in frequency compared to the in-body radiation characteristics. Preferably,

the in-body measurements take place in an isolated chamber to eliminate the effect of external electromagnetic interference. This is to verify the performance in an 'ideal' environment. This can be extended to measurements in an averaged sized room with electronic equipment that can cause interference (for example GSM). The receiver performance must be well known to fully characterize the received pulses.

Lastly, it has to be investigated how much the received pulses vary with the location of the chip and the movement (arm, body) of the phantom. Also, the optimum operating frequency and pulse power has to be verified experimentally.

A. Electromagnetic Wave Propagation

In this appendix the propagation constant, transmission and reflection coefficients of an EM wave in lossy environment will be derived. The basis for this derivation starts with Maxwell's equations in matter, here written in the steady-state frequency domain notation:

$$-\nabla \times \hat{\mathbf{H}} + j\omega\epsilon\hat{\mathbf{E}} + \sigma\hat{\mathbf{E}} = -\hat{\mathbf{J}}^{ext} \tag{A.1}$$

$$\nabla \times \hat{\mathbf{E}} + j\omega\mu\hat{\mathbf{H}} = -\hat{\mathbf{K}}^{ext} \tag{A.2}$$

where

$\hat{\mathbf{H}}$	magnetic field strength [A/m]
$\hat{\mathbf{E}}$	electric field strength [V/m]
$\hat{\mathbf{J}}^{\mathbf{ext}}$	source electric current density [A/m^2]
$\hat{\mathbf{K}}^{\mathbf{ext}}$	source magnetic current density [V/m^2]
$\epsilon = \epsilon_0\epsilon_r$	permittivity [F/m]
$\mu = \mu_0\mu_r$	permeability [H/m]
σ	conductivity [S/m]

A.1. Propagation Constant in Lossy Environment

We will consider an uniform plane wave which has only an x-component of electric field and y-component of magnetic field which are both function of the propagation direction z only.

$$\hat{\mathbf{E}} = \hat{E}_x(z)\,\mathbf{a}_x \tag{A.3}$$

$$\hat{\mathbf{H}} = \hat{H}_y(z)\,\mathbf{a}_y \tag{A.4}$$

Since this wave is only a function of z, we can set $\frac{\partial}{\partial x} = \frac{\partial}{\partial y} = 0$. Furthermore it is assumed that the plane wave is in a source-free region, i.e. the source does not appear in Maxwell's equations: $K = J = 0$. Calculating all field components of equation A.1 and A.2 with the assumptions made above, the remaining equations are

$$\frac{\partial \hat{H}_y}{\partial z} + (\sigma + j\omega\epsilon)\,\hat{E}_x = 0 \tag{A.5}$$

$$\frac{\partial \hat{E}_x}{\partial z} + j\omega\mu \hat{H}_y = 0 \tag{A.6}$$

Combining these two equations lead to a second order differential equation

$$\frac{\partial^2 \hat{E}_x}{\partial z^2} - j\omega\mu \left(\sigma + j\omega\epsilon\right) \hat{E}_x = 0 \tag{A.7}$$

If we let $\gamma^2 = j\omega\mu \left(\sigma + j\omega\epsilon\right)$, the wave equation reduces to

$$\frac{\partial^2 \hat{E}_x}{\partial z^2} - \gamma^2 \hat{E}_x = 0 \tag{A.8}$$

Similarly, we can write the magnetic wave equation

$$\frac{\partial^2 \hat{H}_y}{\partial z^2} - \gamma^2 \hat{H}_y = 0 \tag{A.9}$$

The general solutions to wave equation A.8 and A.9 are:

$$\hat{E}_x = \hat{E}_A e^{\gamma z} + \hat{E}_B e^{-\gamma z} \tag{A.10}$$

$$\hat{H}_y = \hat{H}_A e^{\gamma z} + \hat{H}_B e^{-\gamma z} \tag{A.11}$$

The *propagation constant* γ can be written as $\gamma = \alpha + j\beta$ where α and β are the solutions of the complex square root

$$\alpha = \omega\sqrt{\frac{\epsilon\mu}{2}\left[\sqrt{1+\left(\frac{\sigma}{\omega\epsilon}\right)^2} - 1\right]} \qquad \beta = \omega\sqrt{\frac{\epsilon\mu}{2}\left[\sqrt{1+\left(\frac{\sigma}{\omega\epsilon}\right)^2} + 1\right]}$$

A.2. Electromagnetic Transmission and Reflection Coefficients

To find the transmission and reflection coefficients, we define two homogeneous mediums with different dielectric properties as depicted in Figure A.1.

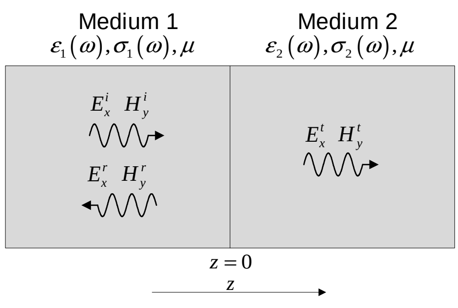

Figure A.1.: Plane wave propagating in two different mediums

An incident plane wave in medium 1 encounters a change of medium at $z = 0$, which causes a reflected and transmitted wave . Using equation A.6, the magnetic field components can be written in terms of incident electric fields components.

The total field in medium 1 is given by:

$$\mathbf{E_1} = \mathbf{E^i} + \mathbf{E^r} = \hat{E}_x^i \left(e^{-\gamma_1 z} + R_E e^{\gamma_1 z}\right) \mathbf{a}_x \tag{A.12}$$

$$\mathbf{H_1} = \mathbf{H^i} + \mathbf{H^r} = \frac{\hat{E}_x^i}{\eta_1} \left(e^{-\gamma_1 z} - R_E e^{\gamma_1 z}\right) \mathbf{a}_y \tag{A.13}$$

Here are R_E and T_E the electric reflection and transmission coefficient, respectively and η is the intrinsic wave impedance

$$\eta = \sqrt{\frac{j\omega\mu}{\sigma + j\omega\epsilon}} \tag{A.14}$$

The field equations in medium 2 are given by

$$\mathbf{E_2} = \mathbf{E^t} = T_E \hat{E}_x^i e^{-\gamma_2 z} \mathbf{a}_x \tag{A.15}$$

$$\mathbf{H_2} = \mathbf{H^t} = T_E \frac{\hat{E}_x^i}{\hat{\eta}_2} e^{-\gamma_2 z} \mathbf{a}_y \tag{A.16}$$

At the boundary $z = 0$ we have:

$$\hat{E}_x^i + R_E \hat{E}_x^i \mathbf{a}_x = T_E \hat{E}_x^i \mathbf{a}_x \tag{A.17}$$

$$\frac{\hat{E}_x^i}{\hat{\eta}_1} - R_E \frac{\hat{E}_x^i}{\hat{\eta}_1} \mathbf{a}_y = T_E \frac{\hat{E}_x^i}{\hat{\eta}_2} \mathbf{a}_y \tag{A.18}$$

Solving this results in

$$R_E = \frac{\hat{\eta}_2 - \hat{\eta}_1}{\hat{\eta}_1 + \hat{\eta}_2} \tag{A.19}$$

$$T_E = \frac{2\hat{\eta}_2}{\hat{\eta}_1 + \hat{\eta}_2} \tag{A.20}$$

Similarly we can calculate the magnetic reflection and transmission coefficients R_H and T_H:

$$R_H = \frac{\hat{\eta}_1 - \hat{\eta}_2}{\hat{\eta}_1 + \hat{\eta}_2} \tag{A.21}$$

$$T_H = \frac{2\hat{\eta}_1}{\hat{\eta}_1 + \hat{\eta}_2} \tag{A.22}$$

B. Measurement inaccuracy

The inaccuracy of the input impedance measurements taken with the Anritsu 37397D vector analyzer can be calculated with the aid of figure B.1.

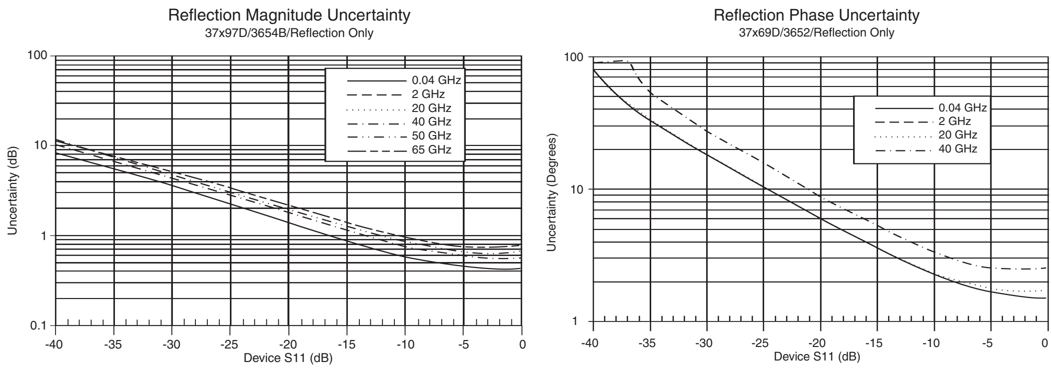

(a) Reflection magnitude uncertainty. (b) Reflection phase uncertainty.

Figure B.1.: Anritsu 37397D measurement uncertainty [41].

S-parameter and impedance are related by:

$$Z_{in} = Z_0 \left(\frac{1 + |S|\, e^{j\varphi}}{1 - |S|\, e^{j\varphi}} \right) \tag{B.1}$$

The variation of the reflection magnitude in Z can be written as

$$\frac{\Delta Z_{in}}{\Delta |S|} = 2Z_0 \frac{e^{j\varphi}}{\left(1 - |S|\, e^{j\varphi}\right)^2} \tag{B.2}$$

where the variation of the reflection phase in Z is:

$$\frac{\Delta Z_{in}}{\Delta \varphi} = j2Z_0 \frac{|S|\, e^{j\varphi}}{\left(1 - |S|\, e^{j\varphi}\right)^2} \tag{B.3}$$

The absolute error in Z is then given by

$$\begin{aligned} \Delta Z_{in} \quad = \quad & 2Z_0 \left| \mathrm{Re}\left\{ \tfrac{\Delta |S| e^{j\varphi}}{(1-|S|e^{j\varphi})^2} \right\} \right| + \left| \mathrm{Re}\left\{ \tfrac{j\Delta\varphi |S| e^{j\varphi}}{(1-|S|e^{j\varphi})^2} \right\} \right| \\ & + j2Z_0 \left| \mathrm{Im}\left\{ \tfrac{\Delta |S| e^{j\varphi}}{(1-|S|e^{j\varphi})^2} \right\} \right| + \left| \mathrm{Im}\left\{ \tfrac{j\Delta\varphi |S| e^{j\varphi}}{(1-|S|e^{j\varphi})^2} \right\} \right| \end{aligned} \tag{B.4}$$

C. Radiation Patterns

The following radiation patterns are the result of a simulated implantable antenna surrounded by 25 mm muscle, 15 mm fat and 1.5 mm skin. The output represents the directivity (linear scale). Note the change in radiation pattern over frequency.

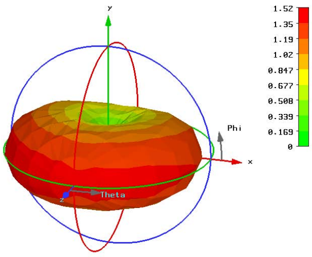

(a) 0.4 GHz.

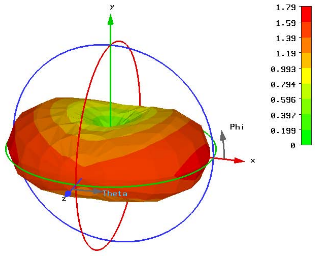

(b) 0.6 GHz

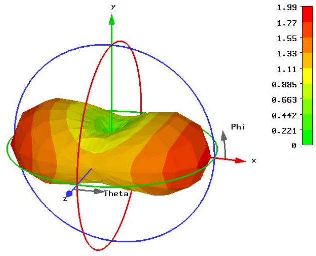

(c) 0.8 GHz

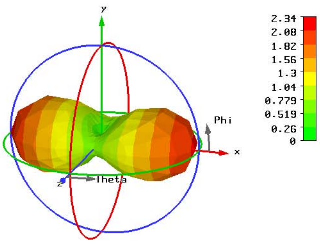

(d) 1 GHz.

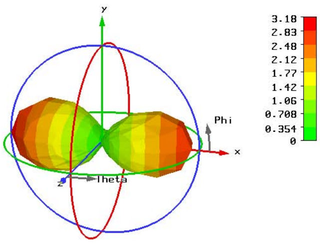

(e) 1.2 GHz.

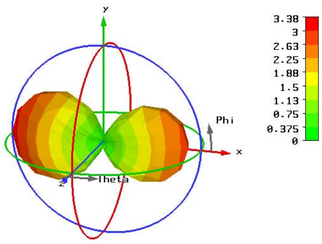

(f) 1.4 GHz.

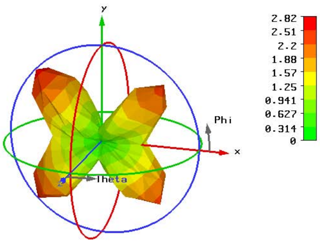

(g) 1.6 GHz.

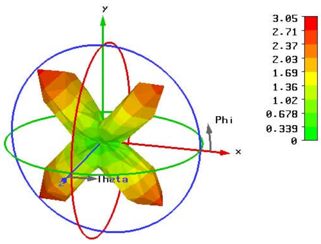

(h) 1.8 GHz.

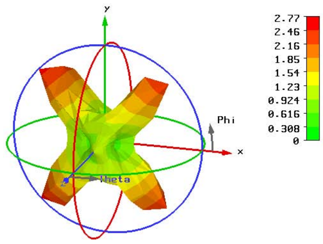

(i) 2 GHz.

Figure C.1.: Change in radiation pattern over frequency.

D. Paper and poster

Sub-GHz UWB Biomedical Communication

Mark Stoopman and Wouter A. Serdijn
Biomedical Electronics Group, Electronics Research Laboratory, Delft University of Technology, the Netherlands
mark.stoopman@gmail.nl, w.a.serdijn@tudelft.nl

***Abstract*—This paper proposes the use of sub-GHz impulse radio Ultra-Wideband (UWB) communication for implantable medical devices. This new concept can offer a more reliable, safer and lower power consuming wireless link compared to other biomedical communications today. An operating frequency below 1 GHz is required to minimize the dielectric absorption of the human tissue and simultaneously allows for low power electronics. Investigating the antenna-electronics interface show that a *current* driven antenna results in the most reliable signal transfer. This interface is not bounded to the conventional 50 Ω interface.**

***Index Terms*—Sub-GHz, UWB, biomedical, wireless communication, implantable medical device, antenna, current driven**

I. Introduction

The microelectronic revolution combined with the advances in chemistry, molecular biology and medicine will have a huge impact on the medical world in the near future. Deep brain stimulation, personalized drug delivery, and patient monitoring are just a few applications in this multibillion-dollar market. Medical implantable devices with wireless communication allow doctors to monitor and adjust the treatment of their patients without any further surgical procedure. This wireless link should be safe, reliable and power efficient. Today, wireless biomedical communication is achieved by inductive coupling or narrow band communication.

Inductive coupling has the advantage that no battery is required, thus ensuring a long lifetime. However, the communication range is limited to a few cm's and is sensitive to the position of the external coil. Depending on the quantity to be measured, this can make health monitoring an inconvenient and time consuming process.

Narrow band communication uses a higher carrier frequency and is based on far field wave propagation. This extends the wireless link range and also results in an increase of bandwidth. The drawback is that narrow band communication can suffer from frequency selective fading. Furthermore, unpredictable variations in the electrical properties of the body can cause a shift in the antenna resonance frequency, making it difficult to match. Finally, it is not very power efficient since traditional narrow band communication uses a continuous wave, resulting in continuous power consumption.

To overcome these problems, we propose sub-GHz UWB biomedical communication. UWB impulse radio uses carrierless, short duration pulses with possibly a very low duty cycle (<1%). This allows for an ultra-low power system with a very low average emission level. High bit rates can be achieved because of the large bandwidth. Another advantage is that UWB impulse radio has a high level of multipath immunity. The antenna-electronics interface is also more robust against variation of the tissue, since the information is spread out over a wide frequency range. Moreover, operating below 1 GHz puts less demands on the electronic circuits in terms of operating current. This in combination with the excellent tissue penetration makes it a good candidate for biomedical communication.

In this paper, the characteristics of human tissue are investigated in Section 2. In Section 3, an equivalent antenna circuit model is developed and possible driving signal quantities are discussed. Section 4 shows the implantable antenna simulation results. A link budget analysis is presented in Section 5. Finally, the conclusions are given in Section 6.

II. Human Tissue

The biomedical communication channel under consideration exists of the implanted medical device, the human body and the surrounding area of the patient. Tissue properties may vary with patient dependent on weight, health, age, position and sex, making it difficult to predict the channel. Still, we need to have an estimation of how much power at which frequency is lost to determine the best operating frequency band.

The dielectric properties of the tissues can be modeled using the complex relative permittivity given in [1]

$$\epsilon_r(j\omega) = \epsilon_\infty + \sum_{n=1}^{5} \frac{\epsilon_s - \epsilon_\infty}{1 + j\omega\tau_n} + \frac{\sigma_i}{j\omega\epsilon_0} \quad (1)$$

where ϵ is the permittivity [F/m], $\sigma(\omega)$ is conductivity [S/m], τ_n is the time constant [s] and ω is the angular frequency [rad/s].

The one-dimensional layered tissue model shown in Figure 1 is used to study the power loss. We assume that the implant is located closely underneath the skin. In this model the plane wave enters perpendicular to an isotropic, homogeneous medium and propagates from inside the muscle tissue, making a transition to fat, skin and finally free space. The other two dimensions extend to infinity.

978-1-4244-7268-0/10/$26.00 ©2010 IEEE

D:/School/TUDelft/Master/Afstuderen/Conference/Biocas Published - Sub-GHz UWB Biomedical

Sub-GHz UWB Biomedical Communication

Mark Stoopman and Wouter A. Serdijn
Biomedical Electronics Group, Electronics Research Laboratory, Delft University of Technology, the Netherlands
mark.stoopman@gmail.nl, w.a.serdijn@tudelft.nl

***Abstract*—This paper proposes the use of sub-GHz impulse radio Ultra-Wideband (UWB) communication for implantable medical devices. This new concept can offer a more reliable, safer and lower power consuming wireless link compared to other biomedical communications today. An operating frequency below 1 GHz is required to minimize the dielectric absorption of the human tissue and simultaneously allows for low power electronics. Investigating the antenna-electronics interface show that a *current* driven antenna results in the most reliable signal transfer. This interface is not bounded to the conventional 50 Ω interface.**

***Index Terms*—Sub-GHz, UWB, biomedical, wireless communication, implantable medical device, antenna, current driven**

I. Introduction

The microelectronic revolution combined with the advances in chemistry, molecular biology and medicine will have a huge impact on the medical world in the near future. Deep brain stimulation, personalized drug delivery, and patient monitoring are just a few applications in this multibillion-dollar market. Medical implantable devices with wireless communication allow doctors to monitor and adjust the treatment of their patients without any further surgical procedure. This wireless link should be safe, reliable and power efficient. Today, wireless biomedical communication is achieved by inductive coupling or narrow band communication.

Inductive coupling has the advantage that no battery is required, thus ensuring a long lifetime. However, the communication range is limited to a few cm's and is sensitive to the position of the external coil. Depending on the quantity to be measured, this can make health monitoring an inconvenient and time consuming process.

Narrow band communication uses a higher carrier frequency and is based on far field wave propagation. This extends the wireless link range and also results in an increase of bandwidth. The drawback is that narrow band communication can suffer from frequency selective fading. Furthermore, unpredictable variations in the electrical properties of the body can cause a shift in the antenna resonance frequency, making it difficult to match. Finally, it is not very power efficient since traditional narrow band communication uses a continuous wave, resulting in continuous power consumption.

To overcome these problems, we propose sub-GHz UWB biomedical communication. UWB impulse radio uses carrierless, short duration pulses with possibly a very low duty cycle (<1%). This allows for an ultra-low power system with a very low average emission level. High bit rates can be achieved because of the large bandwidth. Another advantage is that UWB impulse radio has a high level of multipath immunity. The antenna-electronics interface is also more robust against variation of the tissue, since the information is spread out over a wide frequency range. Moreover, operating below 1 GHz puts less demands on the electronic circuits in terms of operating current. This in combination with the excellent tissue penetration makes it a good candidate for biomedical communication.

In this paper, the characteristics of human tissue are investigated in Section 2. In Section 3, an equivalent antenna circuit model is developed and possible driving signal quantities are discussed. Section 4 shows the implantable antenna simulation results. A link budget analysis is presented in Section 5. Finally, the conclusions are given in Section 6.

II. Human Tissue

The biomedical communication channel under consideration exists of the implanted medical device, the human body and the surrounding area of the patient. Tissue properties may vary with patient dependent on weight, health, age, position and sex, making it difficult to predict the channel. Still, we need to have an estimation of how much power at which frequency is lost to determine the best operating frequency band.

The dielectric properties of the tissues can be modeled using the complex relative permittivity given in [1]

$$\epsilon_r(j\omega) = \epsilon_\infty + \sum_{n=1}^{5} \frac{\epsilon_s - \epsilon_\infty}{1 + j\omega\tau_n} + \frac{\sigma_i}{j\omega\epsilon_0} \qquad (1)$$

where ϵ is the permittivity [F/m], $\sigma(\omega)$ is conductivity [S/m], τ_n is the time constant [s] and ω is the angular frequency [rad/s].

The one-dimensional layered tissue model shown in Figure 1 is used to study the power loss. We assume that the implant is located closely underneath the skin. In this model the plane wave enters perpendicular to an isotropic, homogeneous medium and propagates from inside the muscle tissue, making a transition to fat, skin and finally free space. The other two dimensions extend to infinity.

978-1-4244-7268-0/10/$26.00 ©2010 IEEE

D:/School/TUDelft/Master/Afstuderen/Conference/Biocas Published - Sub-GHz UW

Delft Institute of Microsystems and Nanoelectronics

Closed-Loop Fully Implantable Neuromodulator System

Biomedical Electronics Group

Marijn N. van Dongen, Senad Hiseni, Mark Stoopman, Chi Wing Wu and Wouter A. Serdijn

Goal: Develop a more effective and patient friendly device for neural stimulation.

Methodology: Design a low power, small sized, smart and versatile system, comprising the following blocks:

Supply Electronics

- DC/DC-upconversion
- Variable conversion factor, to improve system efficiency
- Output range: 3V ~ 20V
- Stable output
- High efficiency
- Minimized chip area

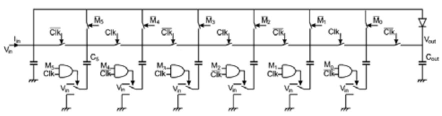

Solution: Charge pump with variable number of stages

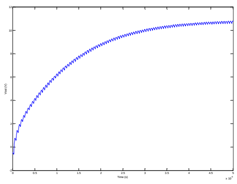

Action Potential Detector

- To be very compact and power-efficient.
- To isolate the Action Potentials (APs) even in case of limited SNR.
- To detect APs in multi-electrode neurodevices.

Solution: Detecting subsequently a positive and a negative spike of each AP.

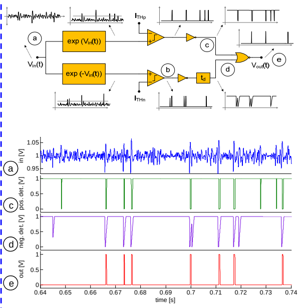

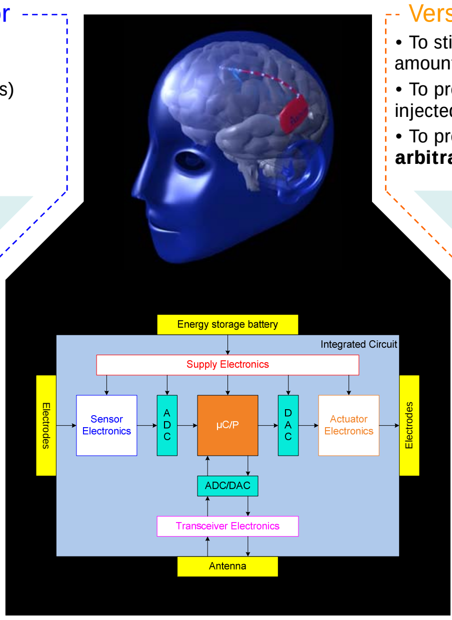

Versatile Waveform Generator

- To stimulate neural tissue a particular amount of **charge** needs to be injected.
- To prevent tissue damage, all charge injected must be **canceled**
- To prevent tissue habituation, any **arbitrary waveform** should be possible

Solution: Voltage based stimulation with indirect current sensing for charge control

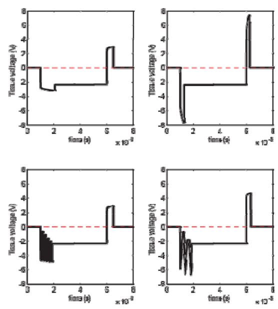

Sub-GHz UWB transceiver

Challenges:

Channel varies with patient

Safe, reliable and ultra-low power

Solution:

UWB in-body antenna modeling

Current driven antenna

Low complexity pulse generator

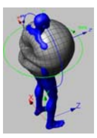

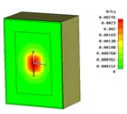

Properties:

High channel capacity

Excellent tissue penetration

Active for 1% of the time

Negligible tissue heating

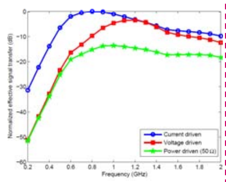

This fully integrated system enables very effective and patient friendly treatment for a wide variety of neural disorders, such as Parkinson, Tinittus, Depression, Schizophrenia and Autism

Delft Institute of Microsystems and Nanoelectronics
dimes

TUDelft Delft University of Technology

Challenge the future

Biomedical Electronics Group

Sub-GHz UWB Biomedical Communication

Mark Stoopman and Wouter A. Serdijn

Electronics Research Laboratory, Delft University of Technology, the Netherlands

Motivation

Implantable medical devices equipped with wireless communication allow

- Doctors to monitor and improve treatment
- To monitor device performance
- To automatically alert medical service in case of an emergency
- An increased comfort for the patient

Today's wireless biomedical communication system consume too much power and can be unreliable.

Objective

We propose the use of sub-GHz UWB biomedical communication

- To maximize the tissue penetration
- To make the wireless communication more reliable
- To minimize tissue heating
- To achieve ultra-low power consumption
- To minimize the path loss

Mark Stoopman
MSc student TUDelft

Human tissue modeling

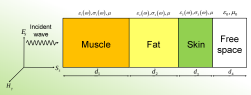

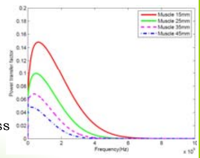

- Multi-layered tissue model to estimate power loss
- Channel varies with each patient
- Best tissue penetration at frequencies < 1 GHz

Tissue penetration vs. frequency

Implantable antenna

$$\lambda = \frac{\lambda_0}{\sqrt{\varepsilon_r + \frac{\sigma}{j\omega\varepsilon_0}}}$$

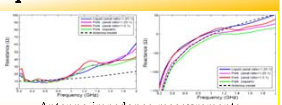

Antenna impedance measurements

- Characteristics are influenced by environment
- Body and antenna seen as one radiating structure
- Small antenna resistance with large varying reactance

Electronics-antenna interface

- Information is represented by power in R_A
- Antenna equivalent circuit models suggest to drive antenna with a *current*
- Power always delivered to radiation resistance
- Impedance matching is *not* required

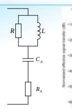

Antenna circuit model

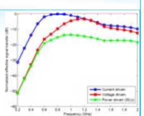

Electronics-antenna signal transfer

Simulation results

Simulation conditions:
CMOS I3T25 0.35μm AMIS technology, V_{DD}=2.5V
Circuit performance:
Tpulse=5 ns, 550 MHz bandwidth
Pavg=109 μW @ 1Mb/s

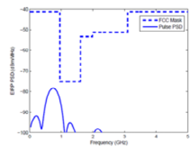

Pulse PSD and FCC mask

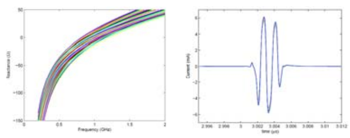

Influence of varying antenna reactance on pulse shape

Proposed Sub-GHz UWB Pulse Generator

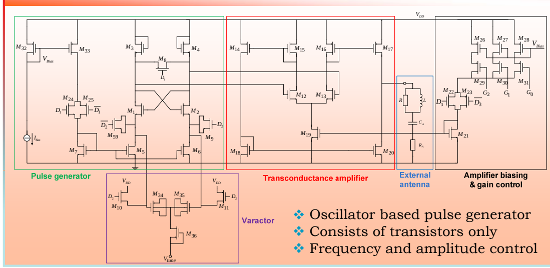

- Oscillator based pulse generator
- Consists of transistors only
- Frequency and amplitude control

Conclusion :

- Sub-GHz UWB offers good tissue penetration, reliable communication and low power electronics
- A current driven antenna offers the highest degree of reliability in this application
- An ultra-low power UWB transmitter is designed which is very robust against antenna impedance variations

Delft Institute of Microsystems and Nanoelectronics dimes

TUDelft Delft University of Technology

Challenge the future

Bibliography

[1] Wong L, Hossain S, Ta A, Edvinsson J, Rivas D, Naas H., "*A very low-power CMOS mixed-signal IC for implantable pacemaker applications*", IEEE J. Solid-State Circuits 39(12): 2446-56, 2004

[2] J.L. da Silva Jr., J. Schamberger, M.J. Ammer, "*Design Methodology for PicoRadio Networks*", IEEE Conference, Design, Automation and Test in europe, University of California at Berkeley, 2001

[3] Harrison, R.R, "*The Design of Integrated Circuits to Observe Brain Activity*" Proceedings of the IEEE, Volume 96, Issue 7, Pages 1203 - 1216,July 2008

[4] J.G. Webster, ed., *Design of Cardiac Pacemakers.* IEEE Press, 1995

[5] F. Asgarian, A. M. Sodagar, "*A High-Data-Rate Low-Power BPSK Demodulator and Clock Recovery Circuit for Implantable Biomedical Devices*"IEEE, Proceedings of the 4th International EMBS Conference on Neural Engineering Antalya, Turkey, May , 2009

[6] A.J. Johansson, "*Wireless Communication with Medical Implants: Antennas and Propagation*", PhD-thesis, Lund University, 2004

[7] K.Y. Yazdandoost, R. Kohno*"An Antenna for Medical implant Communications System"*, Proceedings of the 37th European Microwave Conference, National Institude of Information and Communication Technology Medical ICT Institute

[8] C.-M. Lee, T.-C. Yo, C-H. Luo, C.-H. Tu and Y.-Z. Juang "*Compact broadband stacked implantable antenna for biotelemetry with medical devices"*, IEEE, Electronic Letters, vol 43, Issue 12, page 660-662, June 2007

[9] P. Soontornpipit, C.M. Furse, You Chung Chung, "*Design of implantable microstrip antenna for communication with medical implants"*, IEEE, Microwave Theory and Techniques, vol 52, Issue 8 part 2, page 1944-1951, Aug 2007

[10] Federal Communication Commision, "*Revision of part 15 of the commissions's rule regarding ultra-wideband transmission systems, first report and order (ET Docket 98-153)*", April 2002

[11] Federal Communication Commision, "*Update and changes for the part 15 of the commissions's rule regarding ultra-wideband transmission systems*", http://antiope.com/documents/Part15.pdf, May 2007

[12] C. Gabriel, S. Gabriel and R. Corthout, "*The dielectric properties of biological tissues:I.Litterature survey,*"Phys. Med. Biol.,vol. 41, 1996.

[13] S. Gabriel, R.W. Lau and C. Gabriel "*The dielectric properties of biological tissues:II.Measurements in the frequency range 10Hz to 20GHz,*"Phys. Med. Biol.,vol. 41, 1996.

[14] S. Gabriel, R.W. Lau and C. Gabriel, "*The dielectric properties of biological tissues:III.Parametric models for the dielectric spectrum of tissues,*"Phys. Med. Biol.,vol. 41, 1996.

[15] W. D. Hurt , "*Multiterm Debye dispersion relations for permittivity of muscle",* IEEE Trans. Biomed. Eng. 32, January 1985

[16] V. Raicu, N. Kitagawa and A. Irimajiri, "*A quantitative approach to the dielectric properties of the skin*", Phys. med. Biol, Volume 45, 2000.

[17] M. Yvanoff "*LC Sensor for Biological Tissue Characterization*", PhD thesis, Rochester Institute of Technology, 2008

[18] A. Christ, A. Klingenbock, T. Samaras, C. Goiceanu, N. Kuster, "*The dependence of electromagnetic far-field absorption on body tissue composition in the frequency range from 300 MHz to 6 GHz",* IEEE Transactions on Microwave Theory and Techniques, vol. 54, 2006, pp. 21882195.

[19] M.D. Verweij, P.M. van den Berg, H. Blok, "*Electromagnetic Waves, An Introductory Course*", Delft University Press, ISBN 90-407-1836-9, 1999

[20] B. Noureddine, M. Mohamed and K. Smain, "*Attenuation in transferred RF Power to a Biomedical Implant due to the Absorption of Biological Tissue*", World Academy of Science, Engineering and Technology, volume 10, December 2005

[21] IEEE Std C95.1, " *IEEE Standard for Safety Levels with Respect to Human Exposure to Radio Frequency Electromagnetic Fields, 3 kHz to 300 GHz*" IEEE, E-ISBN: 0-7381-4835-0, New York, 2006

[22] Australian Radiation Protection and Nuclear Safety Agency, "*Maximum Exposure Levels to Radiofrequency Fields 3 kHz to 300 GHz",* Radiation protection series No. 3, March 2002

[23] C.A. Balanis, "*Antenna Theory*", John Wiley and Sons, Inc., 2nd ed., 1982

[24] J. Liang, "*Antenna Study and Design for Ultra Wideband Communication Applications*", PhD thesis, University of London, 2006

[25] A. Vorobyov, "*Planar elliptically shaped dipole antenna for UWB Impulse Radio*", PhD thesis, Delft University of Technology, 2008

[26] A. V. Vorobyov, Sumit Bagga, A. G. Yarovoy, S. A. P. Haddad, W. A. Serdijn, J. R. Long, Z. Irahhauten and L. P. Ligthart, "*Integration of a Pulse Generator on Chip Into a Compact Ultrawideband Antenna*", IEEE, Transactions on Antenna and Propagation, Vol. 56, No 3, March 2008

[27] C. Capps, "*Near Field or Far Field*" EDN, August 16, 2001, pp. 99-102 Available online at: http://www.edn.com/contents/images/150828.pdf

[28] V. S. Mallela, V. Ilankumaran and N.S. Rao, "*Trends in Cardiac Pacemaker Batteries*", Indian Pacing and Electrophysiology Journal (ISBN 0972-6292), 4(4): 201-212, 2004

[29] H.G. Schantz, "*Planar Elliptical Element Ultra-Wideband Dipole Antennas*", IEEE Antennas and Propagation Society International Symposium, 2002

[30] B. Huang, G.Z. Yan and P. Zan, "*Design of ingested small microstrip antenna for radiotelemetry capsules*", IEEE, Electronics letters, Vol. 43 No. 22, October 2007

[31] S. I. Kwak, K. Chang, Y. J. Yoon, "*Ultra-wide band Spiral shaped small Antenna for the Biomedical Telemetry",* IEEE, Microwave Conference, Volume: 1, page 4, December 2005

[32] A. J Johansson, *"Simulation and Verification of Pacemaker Antennas",* 25th Annual international conference of the IEEE engineering in Medicine and Biology society, September 2003.

[33] S. H. Lee, Y. J. Yoon*, "A dual spiral antenna for Ultra-wideband capsule endoscope system"* IEEE Small Antennas and Novel Metamaterials, iWAT International Workshop, Pages 227 - 230, March 2008

[34] L. A. Rocha, P. M. Mendes*, "Electrically Small MEMS Antenna for Wireless Biomedical Microsystems"*, IEEE, Microwave Conference, Page 262-265, October 2008

[35] B. A. Kramer, M. Lee, C. Chen, J. L. Volakis, *"Miniature UWB Antenna with Embedded Inductive Loading" IEEE,* Antenna Technology Small Antennas and Novel Metamaterials, Page 289 - 292, March 2006

[36] K.P. Ray, "*Design Aspects of Printed Monopole Antennas for Ultra-Wide band Applications*", SAMEER, IIT Campus, Hill Side, Powai, Mumbai 400076, India, 2008

[37] Allan W. Love, *"Comment: On the Equivalent Circuit of a Receiving Antenna*", IEEE Antennas and Propagation Magazine, Volume 44, Issue 5, page 124-1245, October 2002

[38] SID Monitoring Station Online Document (December 2009)*,"Magnetic dipole antenna theory"* http://sidstation.lionelloudet.homedns.org/antenna-theory-en.xhtml

[39] Maryam Soltan Zadeh, "*Implantable Loop Antenna*", Master in Applied Science thesis, Simon Fraser University,Canada, 2006

[40] Jack J. Wojcik, Paul G. Cardinal, "*Tissue Recipe and Calibration Requirements SSI/DRB-TP-D01-033*", Spectrum Sciences Institute RF Dosimetry research Board,Canada, 1998

[41] Anritsu, *"Technical Datasheet & Configuration Guide*", 37000D Vector Network Analyzers, 40 MHz to 65/67 GHz, 2007

[42] O. P. Gandhi and Cynthia M. Furse*, "Currents Induced in the Human Body for Exposure to Ultrawideband Electromagnetic Pulses"* IEEE Transactions on Electromagnetic Compatability, Volume 39, Issue 2, May 1997 Page(s) 174-180

[43] Dieter Schwarzbeck*, "The EMI-Receiver according to CISPR 16-1-1"*, Apllication note EMI receivers, Schwarzbeck Mess-Elektronik, Germany

[44] "*Planning for Medical Implant Communications Systems (MICS) & Related Devices*" Proposals Paper SPP 6/03, Australian Communications Authority, October 2003

[45] D. Richerd, R. Srinivasan, M. Reich, "*Design implantable antenna for medical devices*", Cambridge Consultants, Embedded Design India, June 2009

[46] Y. Ahmed, Y. Hao, C. Parini"*A 31.5 GHz Patch Antenna Design forMedical Implants*", International Journal of Antennas and Propagation, Volume 2008, Article ID 167980, 6 pages, July 2008

[47] T. Dissanayake, M. R. Yuce, C. Ho, "*Design and Evaluation of a Compact Antenna for Implant-to-Air UWB Communication*", IEEE, Antennas and wireless propagation letters, Vol 8, 2009

[48] Zarlink Semiconductors, "*ZL70101 Medical Implantable RF Transceiver*", www.zarlink.com, ZL70101 product profile

[49] Tianqi Wang, Wendi Heinzelman and Alireza Seyedi, "*Minimizing Energy Consumption in IR-UWB Based Wireless Sensor Networks*" Department of Electrical and Computer Engineering, University of Rochester

[50] N. Song, M. Wolf and M. Haardt, "*Low-complexity and energy efficient non-coherent receivers for UWB communication*", The 18th Annual IEEE International Symposium on Personal, Indoor and Mobile Radio Communications, Ilmenau University of Technology, 2007

[51] M. Ki*,* S. Choi, H-M Oh, K-H Kim*,"Performance Analysis of Noncoherent UWB Transceiver with PEWB under LOS Residential Channel Environment"*, IEEE Tencon region 10, page 1-6, 2005

[52] L. Stoica*, "Non-coherent energy detection transceivers for Ultra Wideband Impulse radio systems",* Faculty of Technology*,* University of Oulu, Oulu University press, ISBN 978-951-42-8717-6

[53] Q. Tang, S. K. S. Gupta, L. Schwiebert, "*BER Performance Analysis of an On-off Keying based Minimum Energy Coding for Energy Constrained Wireless Sensor Application*", IEEE international conference on communication, ICC, Arizona state university, page 2734-2738, vol. 4, 2005

[54] G. Kolumban, "*UWB Technology: Chaotic Communications Versus Noncoherent Impulse Radio*", IEEE, Proceedings of the 2005 european conference on Circuit Theory and Design, Page II/79-II/82, vol. 2

[55] S.Y. Seidel, T.S. Rappaport, "*914 MHz Path Loss Prediction Model for Indoor Wireless Communications in Multifloored Buildings*", IEEE Transactions on Antennas and Propagation, Vol 40. No. 2, February 1992

[56] AMI Semiconductor, Inc. I3T25 (0.35um) Design Rules, "*I3T25_Design_Rules_1000115_RevD"*

[57] "*C035U (0.35 Micron) Core CMOS Design Rules*", AMI Semiconductor, Inc., 1000042 Revision A

[58] X. Zhang, S. Ghosh and M. Bayoumi, "*A Low Power CMOS UWB Pulse Generator*", IEEE , The Center for Advanced Computer Studies University of Louisiana at Lafayette Lafayette, , 2005

[59] S. Bagga, S. A. P. Haddad, W. A. Serdijn and J. R. Long, "*An FCC Compliant Pulse Generator for IR-UWB Communications*", IEEE, Delft University of Technology, 2006

[60] Y. Shamsa, "*LC Ladder Based Orthonormal Filter for Impulse-Radio UWB Pulse Generation*", Msc Thesis electrical engineering, Delft University of Technology, 2009

[61] H. Kim, D. Park and Y. Joo, "*All-digital low-power CMOS pulse generator for UWB system*", IEEE Electronic Letters,Vol. 40 No. 24,

[62] T. Phan, J. Lee, V. Krizhanovskii, S. Han and S. Lee, "*A 18-pJ/Pulse OOK CMOS Transmitter for Multiband UWB Impulse Radio*", IEEE Microwave and Wireless Components Letters, Vol. 17, No. 9, September 2007

[63] S. Diao, Y. Zheng and C. He[65, 64]ng, Member, IEEE, "*A CMOS Ultra Low-Power and Highly Efficient UWB-IR Transmitter for WPAN Applications*", IEEE Transactions on Circuits and Systems, Express Briefs, Vol. 56, No. 3, March 2009

[64] J. R. Fernandes,H. B. Gonçalves, L. B. Oliveira and M. M. Silva, "*A Pulse Generator for UWB-IR Based on a Relaxation Oscillator*", IEEE Transactions on Circuits and Systems, Express briefs, Vol. 55, No. 3, March 2008

[65] A. Tsitouras and F. Plessas, "*Ultra wideband, low-power, 3–5.6 GHz, CMOS voltage-controlled oscillator*", Microelectronics Journal 40 page 897-904, 2009

[66] I. M. Filanovsky, and C. J. M. Verhoeven, "*Sinusoidal oscillators and multivibrators are not separate classes of circuits*", IEEE International Midwest Symposium on Circuits and Systems, page 778 - 781, August 2009

[67] I.M. Filanovsky, C.J.M. Verhoeven, "*Transition from Sinusoidal to Relaxation Oscillations in Emitter-Coupled Multivibrators*", IEEE, International Conference on Circuits and Systems, page 300 - 303, December. 2006

[68] I. M. Filanovsky, and C. J. M. Verhoeven, "*Sinusoidal and Relaxation Oscillations in Source-Coupled Multivibrators*", IEEE Transactions on Circuit and Systems, Express briefs, Vol. 54, No 11, November 2007

[69] A. Buonomo, A. L. Schiavo, "*Analysis of Emitter (Source)-Coupled Multivibrators*", IEEE Transactions on Circuits and Systems, Regular papers, Vol 53, No 6, June 2006

[70] P. Andreani and S. Mattisson, "*On the Use of MOS Varactors in RF VCO's*", IEEE Journal of Solid-State Circuits, Vol. 35, No. 6, June 2000

[71] R. L. Bunch and S. Raman, "*Large-Signal Analysis of MOS Varactors in CMOS Gm LC VCOs*", IEEE, Journal of Solid-State Circuits, Vol. 38, No. 8, August 2003

[72] K. Kuo and A. Leuciuc, "*A Linear MOS Transconductor Using Source Degeneration and Adaptive Biasing*", IEEE Transactions on Circuits and Systems, Analog and Digital Signal Processing, Vol. 48, No. 10, October 2001

[73] B. Razavi, "*Design of Analog CMOS Integrated Circuits*" International edition, 2001, ISBN: 0-07-118839-8

[74] J. M. Rabaey, A. Chandrakasan. B Nikolic, "*Digital Integrated Circuits, A design Perspective*", 2nd edtion, 2002

[75] Zarlink Semiconductors, "*ZL70250 Medical Implantable RF Transceiver*", www.zarlink.com, ZL70101 product profile

[76] S. Radiom, A. Enayati, G. A. E. Vandenbosch, W. De Raedt , G. Gielen, "*Miniaturization Of a bow-tie antenna for a pulsed-UWB transceiver in a 300-960MHz band*", IEEE, 3rd European Conference on Antenna and Propagation, EuCAP, June 2009

Index